Development of Highly Concentrated Conductive Silver Pastes for Front-Side Metallization of Silicon Solar Cells - Their Flow Properties and Printing Behavior

zur Erlangung des akademischen Grades einer
DOKTORIN DER INGENIEURWISSENSCHAFTEN (Dr.-Ing.)

von der KIT-Fakultät für Chemieingenieurwesen und Verfahrenstechnik des
Karlsruher Instituts für Technologie (KIT)
genehmigte

DISSERTATION

von
Dipl.-Ing. Ceren Yüce
aus Walldorf

Erstgutachter:	Prof. Dr. Norbert Willenbacher
Zweitgutachter:	Prof. Dr.-Ing. Gunter Hübner
Tag der mündlichen Prüfung:	25.07.2019

Preface

This publication based dissertation consists of three peer-reviewed scientific journal articles, two published articles and one submitted article. They include the main results of my experimental work from January 2015 until January 2019 at the Karlsruhe Institute of Technology (KIT), Institute of Mechanical Process Engineering and Mechanics in the group of Applied Mechanics.

The main part of this dissertation follows a brief introduction to the state-of-the-art on solar cells in general including the silver paste formulation concepts, their required rheological properties for solar cell manufacturing as well as the recent different technologies for solar cell front-side metallization used for the experimental part of this thesis. It consists of the following publications:

1. Challenges in rheological characterization of highly concentrated suspensions - A case study for screen-printing silver pastes
2. Rheology and screen-printing performance of model silver pastes for metallization of Si solar cells
3. Non-volatile free silver paste formulation for front-side metallization of silicon solar cells

This thesis concludes with an overall summary, an outlook and a bibliography. The bibliography includes all references of the publications. Hereby the publications are slightly changed. Furthermore, some diagrams and images are modified in size and color taking into account the one column and full color printing of this dissertation. For the reason of better readability, the term “we” is used.

Acknowledgments

I would like to take the opportunity to thank all those who directly or indirectly supported me, the active help on experimental work, fruitful discussions or general support in all cases during my time as a PhD student at the Karlsruhe Institute of Technology. Especially I would like to thank:

- Prof. Dr. Norbert Willenbacher for giving me the chance to do a doctorate at the Institute for Mechanical Process Engineering and Mechanics in the group of Applied Mechanics. The constant support, fruitful and creative discussions about next steps and new ideas were an important contribution to my work. Furthermore, I am thankful for his support in writing papers.
- Prof. Dr.-Ing. Gunter Hübner from the Hochschule für Medien (HdM) Stuttgart, Germany for being my second referee of my thesis.
- The Federal Ministry of Economics and Energy for their generous support. An interesting part of my work was carried out within this publicly funded industrial project with the acronym AdmMo. I would also like to thank the participating industrial partners, especially our subgroup “Metallization”.
- Dr. Markus König, Axel Grumbach, and Lindsey Karpowich from Heraeus Photovoltaics for providing silver pastes as well as raw materials, performing screen-printing tests and for many detailed discussions.
- Herbert Frintrup from Hans Frintrup GmbH for the good cooperation within the project as well as numerous very interesting discussions. Thank you Herbert for your support and helpfulness during my search for printing possibilities on a pilot line. He made it possible for me to perform my printing tests at Hanwha Q Cells GmbH in Bitterfeld-Wolfen through his well-maintained contacts. At this point I also would like to thank Dr. Ansgar Mette and Stefan Hörnlein, for providing us with printing experiments on their industrial pilot line.
- All PV-TEC staff members at Fraunhofer ISE, especially Dr. Jan Nekarda, Michael Linse and Dr. Max Pospischil involved in printing tests and informative discussions about solar cell characterization. Furthermore I would like to thank Max for the proofreading, the good cooperation, and the exchange of his experience.
- Kuninori Okamoto from Changzhou Fusion New Material Company, Shanghai and Adrian from International Solar Energy Research Center Konstanz for

their support in performing the printing tests up to firing and cell characterization, achieving the most important cell efficiency results.

- 100% erneuerbar stiftung for the acceptance as a scholarship holder and their financial support.
- My students Oliver Süß, Kevin Tedjokusuma, Mareike Schmalz, Gina Klotz, Jella Kramer, Willian Calderon da Costa, and Gizem Kayar, writing their bachelor thesis, working as an internship or as a research assistant. It was a great pleasure to work with you.
- Dr. Bernhard Hochstein for his help all over the years concerning a lot of technical and organizational questions.
- The technical staff of MVM, especially the PMT, including Klaus Hirsch, Astrid Huber, and Thomas Lebe, for their support in particle characterization and analysis.
- Volker Zibat from Institute for LEM for the EDX imaging.
- All my colleagues and those who became my friends for the unforgettable time with you at the Institute for Mechanical Process Engineering and Mechanics. Without your help, the partly outstanding motivation as well as the numerous discussions and the ability to work in a team, the results of my work and further developments would have been only a fraction of what I had achieved. Thank you for every minute of laughing (Moritz, Walter, Davi'i'd, Ronald, Claude), travelling (Johanna, Steffen), mental support (Annika, Katharina), accepting me as Ceriff, and also your coffee breaks in my office R219 (everyone). Furthermore, I also want to thank Frank and Chenhui for proofreading.
- Meine Annika, I'm so thankful that our paths have crossed and that you were my office colleague, supporting, pushing, listening and helping me. You are an enrichment to my personal development.
- My friends from my school days (Dajana, Jana, Felix, Friederike, Kathrin, Linda, Sarah, and Saskia), from studying days (Çiğdem, Philipp, and Roberto) and my family friends, especially Seçkin. I know exactly, without you I probably wouldn't be here today. Thank you so much for leading me on this path. Thank you so much for accepting me as I am.
- My family, my mother Nursevil, my father Akın, and my sister Gizem, who have not always made my life easy. However, we made it together. Thank you so much for standing with me on this path and your support not only during my thesis, also during the many years before.

Abstract

Photovoltaic has emerged as a renewable source and key technology in recent years to manage the rising energy demand. The performance of silicon (Si) solar cells depends on the front-side metallization that is commonly realized using traditional screen-printing to apply commercial silver pastes including a complex mixture of solvents, binders, and surfactants besides the particles. Flow properties of screen-printing pastes have to be carefully adjusted to ensure uninterrupted processing. This is challenging since line patterns down to 25 μm have to be achieved. High yield stress ensures good shape accuracy while a strong shear thinning is required for paste flowing through narrow mesh openings. The rheological characterization of such complex, highly concentrated silver pastes, as well as the correlation of rheological properties and the screen-printing behavior, are essential. Preliminary experiments demonstrate different results obtained the same measuring settings but changed measuring geometries. The rheological characterization of highly concentrated pastes implicates difficulties like wall slip, shear banding, plug flow, and sample spill.

Furthermore, silver paste formulation has an important part to achieve cost reduced high-efficiency solar cells since commercial silver pastes contain up to ~ 52 *vol*% silver particles. Saving the material costs and at the same time increasing the efficiency is the motivation for optimizing the electrode morphology. Moreover, dropping the cumbersome processing of polymeric additives represents an economic benefit. Capillary suspensions exhibit high yield stress and strong shear thinning behavior, making the capillary suspension concept promising for the front-side metallization of Si solar cells. A percolating particle network is formed by capillary bridges initiated by the addition of a small amount (< 5 *vol*%) of an immiscible secondary fluid to the pure suspension consisting of silver particles, glass frit, and bulk fluid. Generally, storage stability can be guaranteed. The distinct flow properties (yield stress and viscosity) of such capillary suspension-type pastes can be tuned in a wide range by appropriate choice of the type and amount of secondary fluid according to the demands of the respective printing process to achieve narrow line widths and high aspect ratios. The absence of non-volatile binders or thixotropic agents guarantees that the sintered finger lines are free of residual carbon impurities. Energy dispersive electron microscopy (EDX) imaging suggests that the higher conductivity of the additive-free formulation is due to lower carbon content in the sintered lines compared to lines printed from commercial pastes. This could result in higher finger line conductivity since the electrical conductivity is not disturbed by these impurities. In printed electronics application this is particularly beneficial, since no binders, dispersing agents or rheology control additives are necessary that could potentially deteriorate the electrical properties in the final printed and sintered pattern. Furthermore, the non-volatile free paste formulation concept offers an inherent benefit with respect to the sintering process since paste stabilization is done with volatile solvents.

In this thesis, the rheological properties of two commercial screen-printing pastes, provided by Heraeus Deutschland GmbH & Co. KG, that are used for front-side metallization of solar cells are examined. The investigation includes the determination of yield stress, viscosity at low and high shear rates, wall slip velocity, structural recovery after large deformation, and elongation at break as well as tensile force during filament stretching. The importance of concomitant video recordings for reliable determination of rheological quantities of highly concentrated suspensions showing wall slip, shear banding and sample spillover in a rotational shear rheometer with a parallel-plate sample fixture is demonstrated. Video recordings enable the determination of the true deformation profile and the flow field at the sample rim of the rheometer fixture using appropriate markers. The proper choice of plate roughness and plate separation parameters is also based on these video recordings identified for meaningful rheological characterization. Video recordings turn out to be indispensable for finding the appropriate measurement protocols for a meaningful rheological characterization of silver pastes using plate-plate rotational rheometry. Experimental settings for which wall slip, pure plug flow, shear banding or sample spillage occur could be unequivocally identified. The results strongly depend on the employed experimental setup, and particularly on the surface energy and roughness of the sample fixtures. We develop a detailed experimental protocol addressing all aspects of a reliable rheological characterization of highly concentrated pastes. The careful video supported rheological characterization of these silver pastes may also apply to various other kinds of concentrated suspensions including high density, micron-sized particles.

The above-mentioned measuring protocol is applied for a meaningful characterization of three model silver pastes suitable for front-side metallization of Si solar cells, and corresponding vehicles mainly differing with respect to the concentration of thixotropic agent. Our work includes a direct correlation of rheological paste properties and line morphology obtained from the screen-printing tests at various speeds through a layout screen including line widths between 20 μm and 55 μm. Therefore, we determine their rheological properties, i.e. yield stress, low shear viscosity, storage modulus, wall slip, structural recovery, and fracture strain using steady and oscillatory shear as well as elongational flow rheometry. Our study demonstrates that a minor increase of thixotropic agent concentration (only 15 %) leads to drastic changes in rheological response, especially with respect to yield stress, low shear viscosity, and storage modulus values. Finger line morphology is analyzed for electrodes screen printed through 25, 30, and 50 μm mesh opening at 210 $mm\ s^{-1}$ printing speed. This includes the analysis of dried electrodes with respect to line width, aspect ratio, and cross-sectional area determined with a 3D laser scanning microscope. We compare the results obtained from rheological characterization with that from electrode morphology determination to screen possible correlations. The aspect ratio of printed lines increases significantly with increasing thixotropic agent concentration due to its impact on yield stress and low shear viscosity, whereas the cross-sectional area A_f is independent of sample composition consistent with the gravimetric paste transfer determination revealing that paste laydown is independent of thixotropic agent content. The screen-printing process turns out to be relatively robust against changes in paste rheology. A twofold increase in yield stress

τ_y induces a 15-20 % increase in finger line aspect ratio AR without affecting the total laydown. This observed increase in aspect ratio should have a significant impact on electrical cell properties due to reduced shading losses obtained from finer line-widths at a given cross-sectional area.

The developed non-volatile free silver pastes are successfully applied on monocrystalline, respectively multicrystalline, Si-wafer using standard screen printing as well as emerging technologies such as knotless screen design or Pattern Transfer Printing^{TM} technology. Printing tests with standard screen design are performed through 37 μm finger opening with a series of pastes including the same type and amount of silver particles and glass frit. Results are compared to those obtained using commercial paste formulation including the same silver particles and glass frit. Morphology and electrical cell properties are characterized by employing a 3D laser scanning microscopy and a solar simulator as well as electroluminescence spectroscopy. The results reveal no clear correlation between these flow properties and printing results, i.e. cell performance. With the appropriate choice of bulk and secondary fluid, printed finger line morphologies and electrical cell performance data can be achieved similar to that obtained with commercial reference silver pastes including non-volatile additives. The real-time observation of the screen-printing process is performed using a high-speed imaging system inserted into a screen printer to visualize the paste spreading kinetics during screen-printing on a glass substrate. Knotless screen design experiments are performed through 27 μm finger opening. The silver deposit can be reduced and AR can be increased compared to printing with a standard screen for conventional as well as for non-volatile free pastes. Paste spreading and line interruptions strongly increase with decreasing yield stress and high shear viscosity as well as increasing wall slip. We hypothesize that particularly slip phenomena may have a dominant effect on printing performance. With the Pattern Transfer Printing^{TM} technology we obtain almost interruption-free finger widths $w_f \approx 30$ μm with high AR (≈ 0.5) depending on the paste formulation. Cell performance again suffers from contacting defects which according to visual inspection are caused here by poor adhesion of the deposited lines on the wafer.

In total, we present a versatile route for non-volatile free silver paste formulation. This formulation concept is tunable in a wide range and offers the possibility to meet the requirements for front-side metallization of Si solar cells. Due to the high purity of the pastes and the simple handling, this non-volatile free paste formulation concept has the potential to find a universal use in industrial processes for front-side metallization.

Zusammenfassung

Die Photovoltaik hat sich in den vergangenen Jahren aufgrund des steigenden Energiebedarfs zu einer Schlüsseltechnologie erneuerbarer Energiequellen entwickelt. Die Effizienz der Siliziumsolarzellen ist abhängig von der Frontseitenmetallisierung. Diese Frontkontakte aus kommerziellen Silberpasten werden mit traditionellen Verfahren wie dem Siebdruck appliziert. Die Pasten bestehen aus einer komplexen Mischung aus organischen Lösungsmitteln, Bindemitteln, Tensiden und funktionalen Partikeln. Die Fließeigenschaften von Siebdruckpasten müssen sorgfältig eingestellt werden, um ein unterbrechungsfreies Aufbringen zu gewährleisten. Dies stellt eine Herausforderung dar, da die gedruckten Linien eine Fingerbreite bis zu 25 μm erreichen müssen. Eine hohe Fließgrenze sorgt für eine gute Formgenauigkeit. Eine starke Scherverdünnung ist für das Durchdringen der Paste durch feine Fingeröffnungen ($< 25\ \mu m$) erforderlich. Die Charakterisierung solcher komplexen, hochkonzentrierten Silberpasten bezüglich prozessrelevanten, rheologischen Parametern ist unerlässlich, um die Verarbeitungs- und Produkteigenschaften zu verbessern. Vorversuche zeigten unterschiedliche Messergebnisse für die gleiche Messeinstellung bei der Verwendung von unterschiedlichen Messgeometrien. Die detaillierte rheologische Charakterisierung von komplexen, hochkonzentierten Suspensionen weist aufgrund von Messartefakten, wie z.B. Wandgleiten, shear banding und Spaltentleerung, Schwierigkeiten auf.

Darüber hinaus spielt die Formulierung von Silberpasten eine wichtige Rolle bei der Erzielung kostenreduzierter, hochleistungsfähiger Solarzellen, da kommerzielle Silberpasten bis zu 52 $vol\%$ Silberpartikel enthalten. Die Optimierung der gedruckten Elektroden ist durch die Einsparung der Materialkosten bei gleichzeitiger Erhöhung der Effizienz motiviert. Ein Wegfall der umständlichen Verarbeitung von polymeren Additiven stellt einen wirtschaftlichen Vorteil dar. Kapillarsuspensionen weisen eine hohe Fließgrenze und eine starke Scherverdünnung auf, welches das Konzept der Kapillarsuspension für die Frontenmetallisierung von Siliziumsolarzellen vielversprechend macht. Diese Formulierungsstrategie basiert auf dem sogenannten Kapillarsuspensionsphänomen. Ein Partikelnetzwerk wird durch Kapillarbrücken gebildet, die durch die Zugabe einer geringen Menge ($< 5\ vol\%$) eines nicht mischbaren Sekundärfluids zu der reinen Suspension aus Silberpartikeln, Glasfritte und Hauptflüssigkeit initiiert werden. Die Lagerstabilität solcher Pasten wird gewährleistet. Das Fließverhalten kann in einem weiten Bereich durch eine geeignete Wahl der Art und Menge des Sekundärfluids, um schmale Linienbreiten und hohe Aspektverhältnisse zu erreichen, abgestimmt werden. Das Fehlen von nichtflüchtigen Komponenten wie Bindemittel oder Thixotropiermittel garantiert, dass die gesinterten Fingerlinien frei von Restkohlenstoffverunreinigungen sind. Die energiedispersive Röntgenspektroskopie (EDX) Aufnahmen der gesinterten Fingerlinien deuten aufgrund des detektierten Kohlenstoffs in den Linien aus kommerziellen Pasten, auf

eine höhere Leitfähigkeit der additivfreien Formulierung, welche keine Verunreinigungen aufweisen. In der Anwendung der druckbaren Elektronik ist dies besonders bemerkenswert. Des Weiteren bieten Pasten, frei von nichtflüchtigen Komponenten, einen Vorteil im Bezug auf den Sinterprozess, da die Stabilisierung der Pasten mit flüchtigen Lösungsmitteln erfolgt.

In dieser Arbeit werden die rheologischen Eigenschaften von zwei kommerziellen Siebdruckpasten, welche durch die Heraeus Deutschland GmbH & Co. KG bereitgestellt werden, charakterisiert. Diese Untersuchung umfasst die Bestimmung der Fließgrenze, Viskosität bei niedrigen und hohen Scherraten, Wandgleitgeschwindigkeit, Strukturerholung nach hohen Deformationen und die Bruchdehnung, sowie die Zugkraft bei Pastenverstreckung. Die Bedeutung von Videoaufzeichnungen für die zuverlässige Bestimmung der rheologischen Eigenschaften hochgefüllter Suspensionen, welche Wandgleiten, shear banding und Spaltentleerung während der Platte-Platte-Rotationsrheometrieversuche aufzeigen, wird demonstriert. Videoaufzeichnungen ermöglichen die Bestimmung des wahren Deformationsprofils und des Strömungsfeldes am Probenrand mit Hilfe von geeigneten Markierungen. Dieses Protokoll beinhaltet die Messparametereinstellungen und die erforderlichen Rauhigkeiten der Messgeometrien, die für aussagekräftige rheologische Messungen ermittelt werden. Die Ergebnisse hängen stark vom verwendeten Versuchsaufbau ab, insbesondere von der Oberflächenenergie und der Rauhigkeit der Messgeometrien. Wir haben ein detailliertes experimentelles Protokoll entwickelt, das alle Aspekte einer zuverlässigen rheologischen Charakterisierung von hochkonzentrierten Pasten berücksichtigt. Für eine gezielte Produktentwicklung, die den vielfältigen Anforderungen bei der Verarbeitung und Anwendung solcher komplexen Fluide gerecht wird, ist ein detailliertes Messprotokoll zwingend erforderlich. Die sorgfältige videogestützte rheologische Charakterisierung kann auch für diverse andere Stoffsysteme hochkonzentrierter Suspensionen eingesetzt werden.

Wir wenden das oben genannte Messprotokoll für eine aussagekräftige Charakterisierung von drei Modellsilberpasten an, die für die Frontseitenmetallisierung von Siliziumsolarzellen geeignet sind, und dazugehörige Vehikel, die sich hauptsächlich in ihrer Thixotropiermittelkonzentration unterscheiden. Die Veränderungen in der Pastenrheologie und in der gedruckten Fingerlinienmorphologie werden untersucht, um ein besseres Verständnis über den Zusammenhang zwischen Pastenzusammensetzung, Rheologie und Linienmorphologie zu erlangen. Wir bestimmen ihre rheologischen Eigenschaften, d.h. Fließgrenze, Viskosität, Speichermodul, Wandgleitverhalten, Strukturerholung mit Hilfe der stationären und oszillatorischen Scherrheometrie sowie die Bruchdehnung. Anschließend werden Siebdruckversuche durchgeführt. Schon eine geringe Erhöhung der Thixotropiermittelkonzentration (nur 15 %) führt zu einer drastischen Veränderung der rheologischen Eigenschaften, z.B. Anstieg der Fließgrenze, der Viskosität und des Speichermoduls der Pasten. Für die Charakterisierung der Fingerlinienmorphologie stehen Druckversuche durch 25, 30 und 50 μm Fingeröffnungen bei einer Druckgeschwindigkeit von 210 $mm\ s^{-1}$ im Vordergrund, um die wesentlichen Veränderungen der Pastenrheologie und der Morphologie der gedruckten Fingerlinie zu verdeutlichen. Das Druckergebnis wird durch die Charakterisierung der getrockneten Elektroden in Bezug auf Linienbreite, Aspektverhältnis und Querschnittsfläche mit einem 3D Laserscanning-Mikroskop bestimmt. Wir vergleichen die Ergebnisse der rheologischen Charakterisierung mit denen der gedruckten Elektroden, um mögliche Korrelationen zu überprüfen. Mit

zunehmender Thixotropiermittelkonzentration bzw. mit zunehmender Fließgrenze τ_y der verwendeten Pastenserie nimmt die Fingerbreite w_f der gedruckten Fingerlinien ab und die Fingerhöhe h_f nimmt zu. Dementsprechend weist das Aspektverhältnis AR eine deutliche Abhängigkeit von τ_y auf, während die Querschnittsfläche A_f unabhängig von der Probenzusammensetzung ist. Des Weiteren zeigt der Pastenauftrag auf dem Siliziumwafer eine Unabhängigkeit von der Konzentrationsänderung des Thixotropiermittels. Das Siebdruckverfahren erweißt sich als robust gegen Veränderungen in der Pastenrheologie. Eine Verdoppelung von τ_y induziert eine Erhöhung des Aspektverhältnisses AR der gedruckten Elektroden, ohne den Pastenauftrag zu beeinflussen. Der beobachtete Anstieg von AR sollte einen signifikanten Einfluss auf die elektrischen Eigenschaften der Zellen haben, da die Verschattungsverluste durch feinere Linienbreiten und gleichbleibender Querschnittsfläche reduziert werden.

Die entwickelten additivfreien Silberpasten werden auf mono- bzw. multikristalline Siliziumwafer mit Standardsiebdruck sowie mit neuen Technologien, wie Nullgradsiebe und die Pattern Transfer Printing^{TM} Technologie, appliziert. Druckversuche mit Standardsieben mit einer Fingeröffnungen von 37 μm werden mit einer Reihe von additivfreien Pasten durchgeführt. Die Ergebnisse werden mit der kommerziellen Pastenformulierung, welche die gleiche Sorte und Menge an Silberpartikel und Glasfritte enthalten, verglichen. Die Morphologie und die elektrischen Zelleigenschaften werden mit Hilfe einer 3D Laserscanning-Mikroskopie und eines Sonnensimulators, sowie der Elektrolumineszenzspektroskopie, charakterisiert. Die Ergebnisse zeigen keinen eindeutigen Zusammenhang zwischen diesen Fließeigenschaften und den Druckergebnissen, d.h. des Zellwirkungsgrades. Mit einer geeigneten Wahl an Haupt- und Zweitflüssigkeit werden Fingermorphologien und elektrische Zelleffizienzen vergleichbar mit einer handelsüblichen additivreichen Referenzpaste erreicht. Die Echtzeitbeobachtung des Siebdruckprozesses von additivfreien Pasten erfolgt unter der Verwendung einer Hochgeschwindigkeitkamera, welche in den Siebdrucker eingebaut wird, um die Kinetik der Pastenausbreitung beim Siebdruck auf eine Glasoberfläche zu visualisieren. Versuche mit Nullgradsieben mit einer Fingeröffnung von 27 μm zeigen verglichen mit Standardsieben, dass der Silberauftrag erfolgreich reduziert und das Aspektverhältnis erhöht werden kann. Die Pastenausbreitung und die Fingerlinienunterbrechungen nehmen mit abnehmender Fließgrenze, mit abnehmender Viskosität bei hohen Scherraten, sowie mit zunehmendem Wandgleitverhalten stark zu. Wir gehen davon aus, dass insbesondere das Gleitverhalten der Pasten einen dominanten Einfluss auf das Druckergebnis haben können. Je nach Pastenrezeptur erhalten wir nahezu unterbrechungsfreie Fingerbreiten $w_f \approx 30$ μm mit hohem Aspektverhältnis AR (≈ 0.5) aus Druckversuchen mit der Pattern Transfer Printing^{TM} Technologie. Die elektrische Zelleffizienz ist aufgrund von Fehlern in der Kontaktierung, verursacht durch eine schlechte Haftung der gedruckten Linien auf dem Siliziumwafer, im Vergleich schlechter als die Referenzpaste.

Wir präsentieren eine vielseitige Formulierungsroute für additivfreie Silberpasten. Dieses Formulierungskonzept bietet die Möglichkeit, die Anforderungen an die Frontmetallisierung von Siliziumsolarzellen zu erfüllen. Aufgrund der hohen Reinheit der Pasten und der einfachen Handhabung hat dieses Pastenformulierungskonzept, frei von nichtflüchtigen Komponenten, das Potenzial universell in industriellen Prozessen zur Frontmetallisierung eingesetzt zu werden.

Notations

Abbreviations

CaBER	capillary breakup elongational rheometer
CO_2	carbon dioxide
Cz	monocrystalline
EC	ethyl cellulose
EL	electroluminescence
EOM	emulsion over mesh
fin	final
FOG	fineness of grind
ini	initial
KIT	Karlsruhe Institute of Technology
LVE	linear viscoelastic regime
mc	multicrystalline
max	maximum
min	minimum
MSDS	material safety data sheet
STC	standard test condition
PP	plate-plate
PTP	Pattern Transfer Printing
PV	photovoltaic
Si	silicon
T-Max	Thixatrol Max
vdW	van der Waals
ZnO	zinc oxide

Symbols

Latin symbols

AR	aspect ratio	[-]
A_f	finger cross-sectional area	$[\mu m^2]$
d, d_{plate}	plate diameter	$[mm]$
d_{finger}	finger opening	$[\mu m]$
d_{piston}	piston diameter	$[mm]$
d_{nozzle}	nozzle diameter	$[mm]$

$D_{reservoir}$	feed reservoir diameter	$[mm]$
f	frequency	$[Hz]$
F	force	$[N]$
F_C	capillary force	$[N]$
FF	fill factor	[%]
G, G_P	modulus	$[Pa]$
G_0	elastic modulus	$[Pa]$
G'	storage modulus	$[Pa]$
G''	loss modulus	$[Pa]$
h, h_1, h_{end}	gap height	$[mm]$
h_{break}, h_{br}	breakage height of CaBER piston position	$[mm]$
h_f	finger height	$[\mu m]$
h_{trench}	trench height	$[\mu m]$
I	current	$[A]$
J_{SC}	short circuit current	$[mA{\cdot}cm^{-2}]$
L_{nozzle}	nozzle length	[mm]
M	torque	$[Nm]$
m, $\partial v_{slip}/\partial\tau$	slope of wall slip velocity	$[\mu m{\cdot}(Pas)^{-1}]$
n	rotational speed	$[rpm]$
N_{bridge}	number of capillary bridges	[-]
n_{crit}	critical rotational speed	$[rpm]$
r	plate radius	$[mm]$
R	particle radius	$[\mu m]$
R_q	plate roughness	$[\mu m]$
t	time	$[s]$
t_{II}	shearing time	$[ms]$
T	temperature	[°C]
V	voltage	$[V]$
V_{bridge}	capillary bridge volume	$[\mu m^3]$
V_{OC}	open circuit voltage	$[mV]$
v_{slip}	wall slip velocity	$[\mu m{\cdot}\mathrm{s}^{-1}]$
$v_{stretch}$	stretching velocity TA.XT	$[mm{\cdot}\mathrm{s}^{-1}]$
V^*	characteristic slip velocity	$[\mu m{\cdot}\mathrm{s}^{-1}]$
w_f	finger width	$[\mu m]$
w_{trench}	trench width	$[\mu m]$
$x, x_{particle}$	particle diameter	$[\mu m]$
x_{10}	10th percentile of all particle diameters	$[\mu m]$
x_{50}	50th percentile of all particle diameters	$[\mu m]$
x_{99}	99th percentile of all particle diameters	$[\mu m]$

Greek symbols

ϵ	fracture strain	[-]
γ	deformation	[-]
γ_y	yield strain	[-]
$\dot{\gamma}$	shear rate	$[s^{-1}]$
$\dot{\gamma}_{app}$	apparent shear rate	$[s^{-1}]$
$\dot{\gamma}_{crit}$	critical shear rate	$[s^{-1}]$
$\hat{\gamma}$	deformation amplitude	[-]

$\hat{\gamma}_c$	characteristic deformation amplitude	[-]
Γ_{int}	interfacial tension	$[mN{\cdot}m^{-1}]$
η	viscosity	$[Pas]$
η_{app}	apparent viscosity	$[Pas]$
η_{bulk}	bulk viscosity	$[Pas]$
η_{eff}	cell efficiency	[%]
η_r	relative viscosity	$[Pas]$
η_S	solvent viscosity	$[Pas]$
Θ	contact angle	[°]
Θ_C	three phase contact angle	[°]
τ	shear stress	$[Pa]$
τ_{slip}	critical slip stress	$[Pa]$
τ_w	wall shear stress	$[Pa]$
τ_y	yield stress	$[Pa]$
$\tau_{y,app}$	apparent yield stress	$[Pa]$
$\hat{\tau}_c$	critical stress amplitude	$[Pa]$
ϕ_{solid}	solid content	$[wt\%, vol\%]$
ϕ_{sec}	secondary fluid content	$[wt\%, vol\%]$
Ω	angular velocity	$[rad{\cdot}s^{-1}]$

Contents

1. General introduction

1.1 Motivation

The high greenhouse gas emissions are a global challenge of climate change which pushes electric energy generation from renewable sources. Utilization of photovoltaics, wind energy, hydropower, geothermal energy and biomass is strongly growing [1, 2, 3]. Photovoltaic (PV) systems, namely solar cells, play a key role due to their robustness and virtually maintenance-free operation over long time periods (> 25 years). In 2017, the worldwide installed photovoltaic capacity was 400 GW_p, resulting in a decrease of CO_2 emission of approximately 0.3 gigatons. Today essentially more than 95 % of the globally installed PV systems consists of silicon (Si) wafers with silver contacts on the front-side and aluminum on the rear-side. The metallization is achieved via screen-printing of appropriately formulated silver pastes [4, 5, 6]. Screen-printing is a traditional, robust and versatile printing method since the 1970s for numerous printing applications [4, 5] established in the fabrication of all kinds of electronic devices, such as printed circuit boards [7, 8], thin film transistors [9], displays, touch panels [10], low temperature co-fired ceramic devices [11, 12], and photovoltaic cells [13, 14]. This printing technology is easy to implement and allows a fast metallization for high-volume products like Si solar cells. Currently production rates can reach up to 4000 wafers/h on a single line at low printing cost [6]. This economically attractive technology was one of the key factors enabling the recent improvement of solar cell efficiency and cost reduction. However, a further development leading to saving costs of the solar cell production is necessary. In particular the specific raw material consumption, especially the amount of used silver is a critical parameter. Front-side metallization is done with well-developed silver pastes aiming at higher cell efficiency. Today about 7.5 % of the global silver production are used for the metallization of solar cells [6]. For this purpose, a significant material cost reduction achievable by the reduction of the silver consumption per wafer as well as a further enhancement of cell efficiency are essential for an expansion of PV installations in near future. An optimization of the solar cell front-side metallization can be achieved by finger width (w_f) reduction down to 30 μm and high aspect ratio (AR) enhancement ($AR > 0.6$) with good finger line uniformity. This leads to reduced material consumption and minimized shading losses [6, 15, 16]. The narrower and the higher the printed electrodes, the better is the cells efficiency and the total cost per produced kWh is reduced.

A suitable and carefully adjusted silver paste formulation is required to exceed the limitations of resulting finger width on the final product. State-of-the-art finger width achieved by the screen-printing technology goes down to 30 μm [17]. The adjustments are realized by optimizing the paste composition, i.e. silver particles, glass frit, organic solvent or non-volatile binders. Two key features, namely, the wetting and the flow properties of the paste, are decisive in achieving high-performance printed fingers. A comprehensive rheological characterization of screen-printing pastes is essential in order to improve processing properties and product features. From flooding of the screen to the snap-off of the screen from the wafer the paste is exposed to complex loads, including a broad range of shear rates and stresses. In addition, resistance to elongational deformation during snap-off, structural recovery after being squeezed through the screen openings, and slip at the boundaries of these openings, also have to be considered [18, 19, 20, 21, 22, 23, 24, 25, 26, 27]. Rheological characterization of up-to-date commercial silver pastes for front-side metallization is a particular challenge. Rheological measurements are limited by wall slip and shear banding phenomena, as well as sample spill strongly depending on the employed experimental set up. In particular the surface energy and roughness of the sample fixtures, in addition to the details of the experimental protocol are parameters strongly influencing the measurement results.

The high conductivity of silver pastes based on the so-called capillary suspensions concept, i.e. ternary solid/fluid/fluid systems without any addition of non-volatile organic components [28], was demonstrated in preliminary lab scale stencil printing tests. A twofold increase of conductivity compared to layers produced from commercial pastes under identical conditions could be gained [28]. The non-volatile components such as polymeric thickeners, binders and thixotropic agents in commercial silver paste formulation are not necessarily burned out without residues in the sintered electrode. These small amounts of residual carbon in the sintered finger line can considerably deteriorate the conductivity of the printed layer. The special feature of capillary suspensions is that the used liquids, termed bulk fluid and secondary fluid, are immiscible and accordingly a sample-spanning particle network of particles suspended in the bulk fluid forms driven by the capillary forces acting in the ternary system. The strength of this particle network results in a high yield stress and guarantees storage stability for several months, even with the high density difference between silver particles and continuous phase relevant here [28, 29, 30, 31]. This network, however, breaks down when external stresses are applied and this results in a high degree of shear thinning which can be varied in a wide range according to the demands of the respective printing process for narrow finger line printing [28]. Besides the cost-efficient production process of Si solar cells with high electrical performance, additive-free formulation has a further benefit regarding the sintering process. Burned-out polymeric additives are likely to contaminate the sintering furnace and ventilation ductwork and accumulated residues may cause unexpected changes to the sintering furnace performance, excessive downtime for maintenance, and possible fire hazard as carbonaceous residues build within ventilation ductwork [32]. In this sense the non-volatile free paste formulation concept offers an inherent benefit with respect to the sintering process.

Further reduction in finger width can be achieved with emerging application technologies, i.e. knotless screen [33], dispensing [34], flexographic printing [35, 36], or Pattern Transfer Printing^{TM} (PTP) [37] to excel the actual width and AR limits. Recently, finger widths of $w_f = 28\ \mu m$ could be obtained using knotless screen [38] and $w_f = 21\ \mu m$ is achieved with the PTP technology [39]. Adjusting the pastes flow behavior is essential for these aforementioned printing technologies.

1.2 Solar cells

Sunlight can be directly converted into electricity using an electronic device, the solar cell. A typical silicon solar cell structure consists of a n-doped (phosphorus doped) emitter layer and a p-doped (boron doped) base substrate. Silicon can be doped with phosphorus consisting of five valence electrons and with boron containing three valence electrons for the defined modification of conductivity. The n-doped layer can support free electrons while the p-doped layer is including holes. By the contact of the n-doped emitter and the p-doped base a p-n junction is generated which forms a space charge region. Free electrons at the interface layer of the n-region can recombine by diffusion with a hole of the p-region. This results in free charge carriers, so-called electron-hole pairs, generated under irradiation (see Figure 1.1). In order to use the effect for generating electrical energy, the electron-hole pairs must be separated from each other. This is achieved by the electric field due to the differences in the electric charges of the positively charged phosphorus atom in the n-doped layer and a negatively charged boron atom in the p-doped layer. The electrons and holes migrate to the respective electrode, creating a voltage. The electrons flow via the solar cell contacts at the n-doped layer into the external load. They are dissipating their energy and return to the rear-side contact of the solar cell [40].

Conductive contacts are applied by screen-printing on the front- and rear-side of the cell as electrodes. The rear-side contact is usually covering the entire surface and is made of aluminum paste. The front contains a pattern of thin silver electrodes to reduce the shading losses. Shape and area coverage of these front contacts play a striking role for the efficiency of the solar cells. Fine conductive fingers are connected with the so-called busbars, bundling and transmitting the current flow from the conductive fingers [41, 42, 43]. The degree of energy release to the external load is determined by the amount of photons reaching the emitter and thus is depending on the irradiated area. The greater the shading area of the front contacts the less is the irradiated area [44] and the less the cell efficiency. The geometry of the fingers is crucial to keep losses low and to achieve the highest possible efficiency. In order to avoid losses due to the recombination of electrons with holes, the diffusion paths to the electrodes must be kept short. This can be achieved by a larger number of contact fingers [45], but at the same time more contacts mean a higher shading of the wafer by the non-transparent electrode structures. Shading losses can be kept low by printing of ultra-fine contact lines ($< 30\ \mu m$) with high aspect ratio ($> 0.6\ \mu m$) possible with adjusted pastes or innovative printing methods resulting in higher efficiency [6, 15, 16, 44, 46].

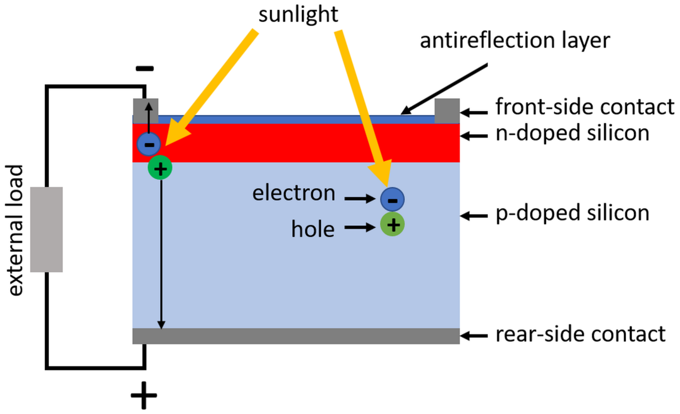

Figure 1.1: Schematic diagram of a silicon solar cell structure.

1.2.1 Front-side metallization printing technologies

1.2.1.1 Screen-printing technology with standard and knotless screen design

The central element of the well-established screen-printing process is a fine-meshed screen. The paste is pushed through the mesh openings using a rubber blade, the so-called squeegee with a certain squeegee hardness, usually between 55 and 85 Shore, with adjusted squeegee angle, squeegee pressure, snap-off height and printing speed. The squeegee angle is defined as the angle between the substrate and the squeegee, which is important for the shear profile in the paste roll [21]. The squeegee pressure influences the paste laydown on the substrate. A too low pressure would result in non-uniform printed finger lines and a too high pressure would cause wider finger lines at the same time decreased finger height due to the paste spreading, respectively bleeding. The snap-off height is the distance between substrate and screen, when the screen is lifting up from the substrate to its initial position behind the printing squeegee in the printing process. This height has to be well adjusted since too high or low snap-off heights are influencing the electrode shape. Ideally, the paste is adhering completely to the substrate, when the squeegee has passed and the screen lifts up again to its initial position. The snap-off carries the risk to peel the printed elements. The printing speed is also affecting the printing result since the paste roll, respectively the pastes shear profile, is changed applying varied printing speeds. Printing speed on an industrial cell production line is around 300 mm/s [47]. A careful adjustment of screen tension, snap-off height, printing speed, squeegee pressure, squeegee angle as well as the material of the squeegee is decisive for a good printing result [20].

The resulting electrode morphology can also be influenced by the screen properties. The screen consists of an aluminum frame and a mesh of wires being fixed to the frame. An emulsion respectively polymer capillary film is coated onto the screen which is photolithographically structured with the requested printing layout. This design is applied as the negative printing motif on the screen to locally prevent the paste penetration and thus to define the later release of the printed pattern. The finger openings are formed by washing out the uncured emulsion with water. During the printing process, the so-called stencil faces the substrate to be printed, i.e. here the Si-wafer (see Figure 1.2).

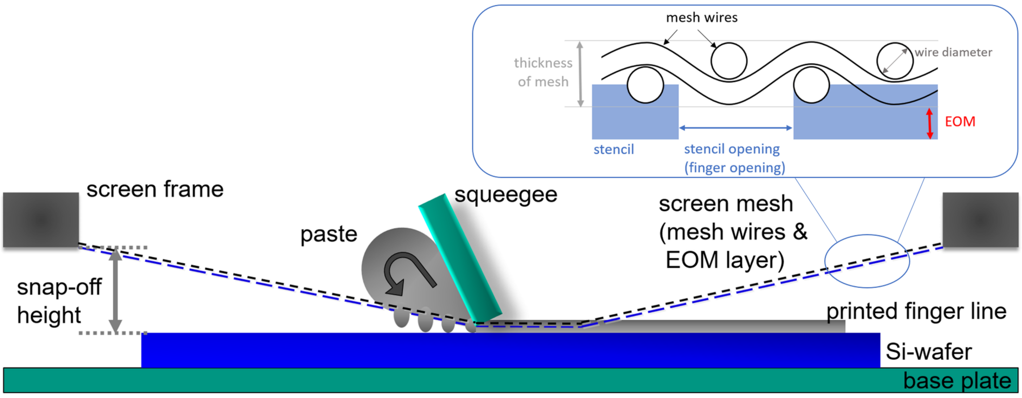

Figure 1.2: Schematic diagram of the screen printer construction during the screen-printing experiments and a screen cutout.

The height of the emulsion above the mesh is defined as EOM (emulsion over mesh). The EOM thickness influence the resulting electrode morphology. It is related to the paste laydown and is limited by the ratio of width to height of the finger opening. A high EOM thickness enables printing of fingers with a high aspect ratio for large finger openings. For narrower finger openings a high EOM thickness would result in paste transfer defects during the paste application. The adjusted thin EOM thickness for narrow finger openings reduces the finger volume which limits the paste spreading [25].

In Figure 1.3(a) cut-outs from standard screen design with 22.5° oriented mesh wires to the screen frame is compared with a new screen design Figure 1.3(b), the so-called knotless screen. The main difference is the 0° mesh wire orientation to the screen frame and hence the direction of finger lines. Furthermore, mesh marks, i.e. two crossed wires in the finger opening of the standard screen, in the open channels are absent. Mesh marks are preventing the paste laydown on the substrate and additionally cause interruptions in printed electrodes. For the knotless screen design, interruptions in the printed finger lines are reduced and an enhanced paste transfer, improved finger uniformity and a better lateral conductivity are expected while decreasing finger width and increasing AR at the same time [33, 48]. Recently, finger widths of $w_f = 28\ \mu m$ could be obtained using knotless screen [38]. An equipment upgrade for the knotless screen design is not required, ultra-fine line printing is easily applicable and the less mesh blocking is a further advantage due to the larger screen open ratio of the given mesh [48].

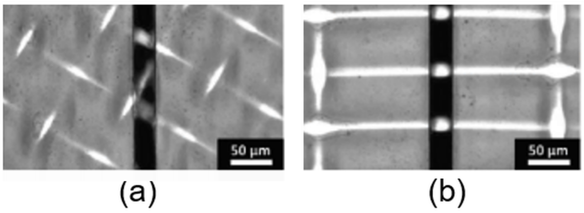

Figure 1.3: Cutouts are demonstrating the mesh wire orientation in the finger mesh opening (here 25 μm) (a) standard screen design with 22.5° and (b) knotless screen design with 0° to the screen frame and hence the direction of finger lines.

1.2.1.2 Pattern Transfer Printing

Pattern Transfer Printing^{TM} (PTP) is a contactless printing technology based on laser induced paste deposition from a polymer substrate, a so-called tape [37]. Paste application on the transparent tape is performed using doctor blades. Trenches are filled up with the paste. The transfer of the paste pattern to the substrate is performed using laser light irradiation. The solvent at the interface between polymer substrate and paste is evaporated due to the dissipated high energy locally increases the temperature above the boiling point of the solvent included in the paste. The resulting overpressure deliminates the paste from the polymer substrate trench and it is deposited on the wafer underneath (see Figure 1.4) [37]. This method enables the manufacturing of ultra-fine finger lines ($< 20\ \mu m$) with high aspect ratio (> 0.6) since the trench width and height in the typically used tapes are 20 μm [39]. It is, however, not yet used on a commercial level.

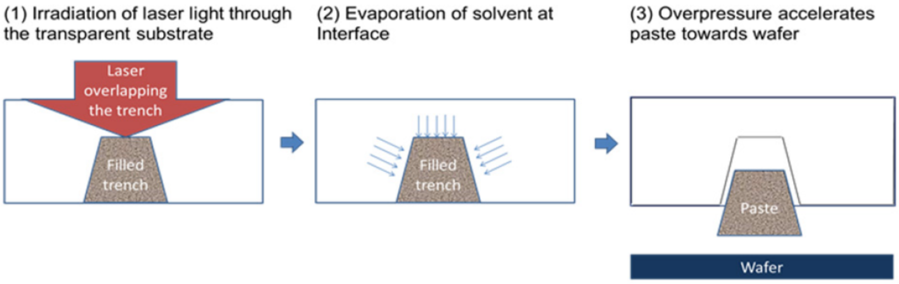

Figure 1.4: Electrode application with the PTP technology [37]. (1) Irradiation of laser light through the transparent polymer substrate to remove the paste filled in the trenches. (2) Solvent evaporation at the interface between transparent substrate and paste due to the high dissipated energy and locally temperature increase above the boiling point of the included solvent for paste formulation. (3) Electrode acceleration towards the wafer induced by the evolved overpressure at higher temperatures.

1.2.2 Silver paste formulation for front-side metallization pastes

1.2.2.1 Conventional silver paste formulation

Highly concentrated conductive screen-printing pastes for front-side metallization of solar cells mainly consist of three components: the conductive material, the vehicle and the glass frit [12, 49, 50, 51]. Generally, 85-90 $wt\%$ micron-sized spherical silver particles (particle diameter, median, $x_{50} \approx 1\text{-}3\ \mu m$) providing good electrical conductivity of printed and fired structures are used as the conductive material [52, 53]. The particles are suspended in the continuous phase (5-14 $wt\%$), the so-called vehicle. This is a mixture of organic solvents containing non-volatile organic binders and additives. Organic solvents are demonstrating advantages in their high boiling points, beneficial for the protracted printing process on industrial scale. Paste consistence is not changed remarkably during the high-throughput printing process. Depending on the wetting behavior of the particles, solvents has to be chosen guaranteed dispersibility. The binder determines the high shear viscosity of the paste relevant for the printing process [24, 54, 55, 56]. The so-called thixotropic agents included in paste formulations are providing the sedimentation stability and shape accuracy of printed lines and are adjusting the flow behavior of the pastes during the application process due to the shear thinning behavior. Therefore, hydrogenated castor oils and diamines are often used as thixotropic agents, whereas synthetic acrylate polymers or ethyl cellulose are frequently added as binders.

In addition, preferably micron sized leaded glass frit (1-5 *wt*%) is dispersed as a further solid component to etch and hence open the passivation layer during the contact firing step [57]. At around $T \approx 500$ °C remained organic components are burned out and the contact formation takes place between $T = 750$ and 900 °C. The degree of the etching of the anti-reflection layer for contact formation depends on the firing duration, respectively high temperature, as well as glass frit amount [58]. Also the chemical composition of the glass plays a key role and has to be adjusted correspondingly. The glass frit enables the formation of ohmic contacting between the printed electrodes and the Si-wafer layer to promote conductivity [57, 59, 60, 61, 62, 63, 64].

1.2.2.2 Silver paste formulation based on capillary suspensions

Capillary suspensions can be described as ternary systems consisting of solid particles suspended in two immiscible liquids, termed as bulk and secondary fluid. Typically, the latter is the minority phase. The addition of a small amount of a secondary fluid to a suspension results in the formation of a sample-spanning particle network connected by capillary bridges consisting of the secondary fluid. The rheological behavior changes from a fluid like, weakly elastic to highly elastic, gel-like state. The suspension is stabilized and phase separation is avoided due to the strong particle network [29]. In the case of conductive silver pastes, the addition of non-volatile binders and additives mentioned above is superfluous. Non-volatile free silver pastes suitable for the front-side metallization of Si solar cells based on capillary suspensions consists of only four components, silver particles, glass frit, the bulk fluid and the secondary fluid [28]. The absence of non-volatile components such as polymeric thickeners, binders or thixotropic agents guarantees that the sintered layers are free of residual carbon impurities and result in higher conductivities since the electrical conductivity is not disturbed by these impurities.

The network formation of capillary suspensions can appear in the pendular state when the added secondary fluid preferentially wets the particles and forms liquid bridges (three-phase contact angle $\Theta_C < 90°$) and in the capillary state when the particles are not preferentially wetted by the secondary fluid. In the latter case particle clusters form around small droplets of the secondary fluid ($\Theta_C > 90°$) (see Figure 1.5). In both cases secondary fluid is able to re-wet the particle, so bulk fluid can be replaced from the particle surface to create a capillary network.

In binary particle/fluid systems, i.e. regular suspensions dominating van der Waals (vdW) attraction can lead to the formation of sample-spanning network structures. In pendular state capillary suspensions, the secondary fluid forms bridges between the particles and corresponding capillary forces F_C control network formation

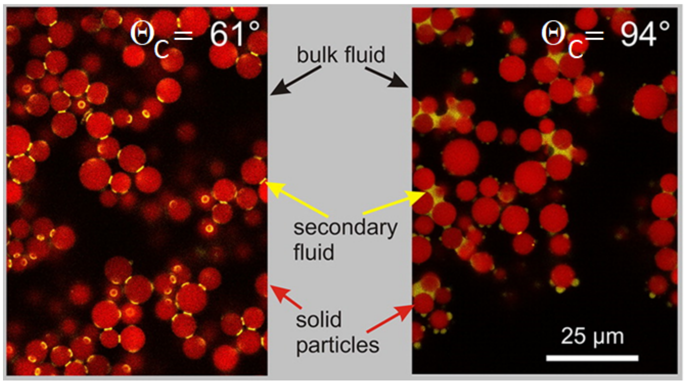

Figure 1.5: Two dimensional confocal image of the sample-spanning particle network in a capillary suspension made of dyed glass beads ($x_{particle} = 6.4\ \mu m$, (red)), dyed secondary liquid which is a water/glycerol mixture (yellow) and oil as bulk fluid (black). On the left is an example for interconnected particles in the pendular state ($\Theta_C < 90°$) and on the right the capillary state ($\Theta_C > 90°$) [65].

and strength. The capillary force depends on the selected liquids and the corresponding interfacial tension Γ_{int} as well as the wetting properties, characterized by the contact angle Θ_C, of the ternary system. These correlations are demonstrated in a simplified equation (1.1) for the capillary force F_C between two identical and spherical particles with diameter x [66]:

$$F_C = \pi \cdot x \cdot \Gamma_{int} \cdot \cos(\Theta_C) \tag{1.1}$$

This equation applies under the following assumptions: the particles are in contact, the fluid bridge volume V_{bridge} is small compared to the volume of the spherical particles and capillary bridges are toroidally shaped. The main parameters influencing the paste can be directly highlighted with this equation [29, 31, 66]. In a system with particle sizes $x > 1\ \mu m$ capillary forces are much stronger than vdW forces which then do not have to be considered [67]. Tuning the paste formulation results in changed rheological behavior, e.g. yield stress τ_y, determined empirically in detail [31, 66, 68, 69]. The yield stress of a capillary suspension in the pendular state can be related to the force F_c as follows [67]:

$$\tau_y = f(\phi_{solid}, \phi_{sec}) g(V_{bridge}) \cdot \frac{4 \cdot \pi \cdot \Gamma_{int} \cdot \cos(\Theta_C)}{x} \tag{1.2}$$

again assuming equal-sized, spherical particles in contact. The yield stress in capillary suspensions depends on the volume of an individual bridge via the function $g(V_{bridge})$ and on the number of bridges which in turn depends on solids and secondary fluid content captured in the function $f(\phi_{solid}, \phi_{sec})$. The yield stress increases with increasing secondary fluid content ϕ_{sec} and solid content ϕ_{solid} due to increased number of particle-particle contacts as well as capillary bridges [31, 66, 70]. Furthermore, τ_y depends on reciprocal particle diameter (x^{-1}) [31], the interfacial tension Γ_{int} and the three phase contact angle Θ_C. Further investigations regarding the influence of Γ_{int} [31] and Θ_C [65] are not discussed in more detail, here.

1.2.3 Rheological properties of silver pastes

So far it is assumed that the defect free processing of narrow and uniform electrodes in solar cells front-side metallization can be carefully adjusted by the flow properties of screen-printing pastes. A first attempt towards rheological characterization of a commercial silver paste was provided by [18]. Narrow electrode lines with a high aspect ratio require silver pastes with a high yield stress guaranteeing good shape accuracy [12, 25, 51, 71, 72]. Furthermore, screen-printing pastes should exhibit a substantial degree of shear thinning for a low viscosity at high shear rates for the pastes flow through narrow mesh openings [18, 24, 71]. Afterwards, structure and viscosity must recover quickly to prohibit paste spreading on the substrate to achieve an optimum printing result with a layer thickness that is as uniform as possible and exact edge sharpness to reduce shading losses [18, 20, 73, 74, 75, 76, 77]. The flow properties of screen-printing silver pastes and concepts relating to the control of yield stress and shear thinning behavior via polymeric additives is a well discussed topic in previous studies [55, 56, 74]. Various other complex flow phenomena like shear banding or avalanching may occur in such suspensions [78, 79, 80]. Wall slip is also crucial to concentrated suspensions [81, 82, 83, 84]. A thin layer of liquid of lower viscosity, i.e. a layer depleted or free of particles is formed next to the wall [84, 85, 86, 87, 88, 89, 90] and may control flow through narrow gaps or channels. Wall slip is considered to be important for the screen-printing performance of highly concentrated pastes. The paste glides through the mesh easier at higher wall slip and its deposit on the substrate is increased significantly [26]. Two recent studies revealed that wall slip of silver pastes can have a significant impact on paste transfer and line shape [26, 27]. A higher slip velocity resulted in a higher silver laydown and a higher aspect ratio of the printed lines, as well as in a narrower intersection of busbars and fingers.

Recently, the effect of paste rheology during the screen-printing process was directly investigated in a combined rheological and high-speed imaging study [91]. Screen-printing of ZnO pastes, including different types and concentrations of thixotropic agent and ethyl cellulose binder, on a glass substrate confirmed that the length of the pre-injection zone is inversely proportional to the yield stress, whereas the length of the cling zone was linearly related to the filament rupture strain. The printed electrode width turned out to be inversely proportional to the product of the yield stress and high shear viscosity and the spreading process was limited to a period of 100 ms after the squeegee had passed [91].

The gain of scientific insight in such studies trying to correlate paste rheology and printing performance is limited when pastes with different compositions, not only with respect to rheology but also in terms of their substrate wetting properties, are investigated [25, 27].

1.2.4 Cell performance characterization

1.2.4.1 Electrode morphology

The electrode morphology is generally examined with a 3D laser scanning microscope (see Figure 1.6(a)). This investigation includes the following parameters:

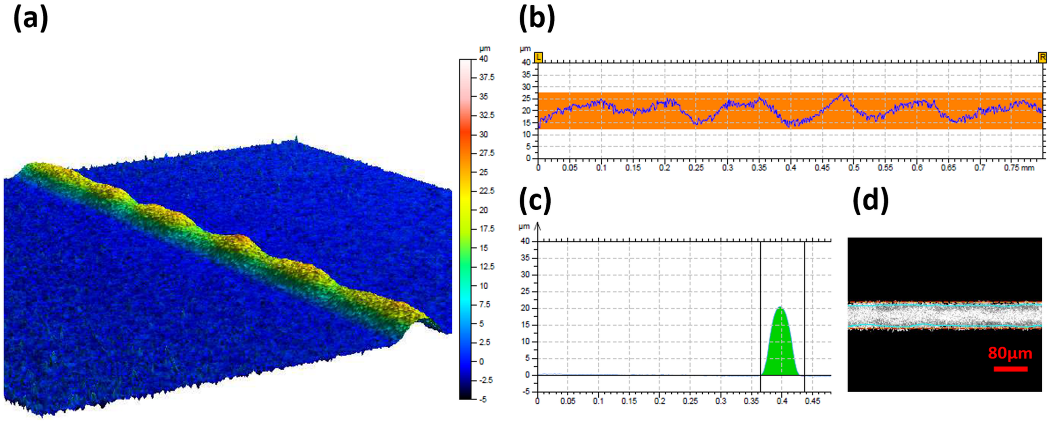

Figure 1.6: (a) Screen printed finger line height profile image examined with a 3D laser scanning microscopy, (b) side view of printed finger line to detect the fluctuations in the longitudinal height profile caused by the mesh marks, (c) detection of the cross-sectional area A_f, (d) top-view of finger width edge detection.

Finger width w_f Finger width is defined as the maximum horizontal expansion of the finger cross section plane which is directly influencing the shading losses on the solar cell (see Figure 1.6(d)). The minimization of the shaded area on Si solar cells results in increased electrical performance. Accordingly, decreasing the silver consumption is the main purpose of further paste development as well as for emerging front-side metallization technologies.

Finger height h_f Finger height of printed electrodes is the parameter with the highest fluctuations in the longitudinal profile due to defects caused by mesh wires in the mesh opening (see Figure 1.6(b)). Finger height fluctuations have to be minimized in order to keep the line or grid resistance low. Especially with very narrow contact fingers, the height of the fingers must be as uniform as possible.

Finger cross-sectional area A_f The cross-sectional area of fired fingers (see Figure 1.6(c)) is depending on the finger width and finger height ($A_f \approx 0.5{\cdot}h_f{\cdot}w_f$) and is influencing the grid resistance. A large cross-sectional area is essential for high conductivity [92]. Optimization can be done by adjusting the paste formulation and/or working on innovative paste application technologies.

Aspect ratio AR Aspect ratio is defined as the ratio of finger height to finger width ($AR = h_f/w_f$). Best light incidence can be reached by narrow, high and triangular shaped finger lines supporting the direct reflection of irradiated sunlight [93]. In solar cells with screen printed contacts, the shaded areas make up about 10% of the cell surface [46]. This disadvantageous effect results in an effort to produce lines that are as thin and high as possible. Due to the reduced shading losses of the cell, more charge carrier generation processes take place, current density and efficiency increase. In this context, the aspect ratio AR is often referred to.

1.2.4.2 Electrical cell performance

The electrical cell performance of important characteristic solar cell parameters is done by conducting a current vs. voltage (I-V-curve) measurements on printed and fired solar cells at standard test conditions (STC: 1000 W/m^2, 25 °C, AM 1.5).

Short circuit current J_{SC} The short circuit current is defined as the current through the solar cell, when the voltage across the solar cell is zero, or in other words when the solar cell is short circuited. J_{SC} is influenced by the finger width. The narrower w_f the higher is J_{SC}.

Open circuit voltage V_{OC} The open circuit voltage is the maximum voltage available from a solar cell occurring at current $I = 0$ A, or in other words when no current flows between the two poles.

Fill factor FF In conjunction with J_{SC} and V_{OC}, defined as the maximum current and voltage from a solar cell, the fill factor FF characterizes the resistive and non-resistive losses from a solar cell. It is defined as the ratio of the maximum power from solar cell ($V_{mp} \cdot I_{mp}$) to the product of J_{SC} and V_{OC}. This characterizes the degree of the solar cells ability to collect the charge carriers generated by light.

Cell efficiency η_{eff} Cell efficiency is the decisive parameter characterizing the cell performance and is defined as the ratio of energy output from the solar cell to the input energy from the solar simulator ($\eta_{eff} = (FF{\cdot}J_{SC}{\cdot}V_{OC})\ /\ P_{in}$). Influencing factors are the spectrum and the intensity of the incident sunlight as well as the temperature of the solar cell. To compare solar cell efficiencies measuring conditions must be carefully controlled, and only efficiency data obtained under standard test conditions (STC) should be compared.

1.2.4.3 Electroluminescence spectroscopy

Electroluminescence (EL) spectroscopy measurements are performed with fired Si solar cells. The results provide an overview over solar cell uniformity and electrode contacting [94]. A direct current is applied to the solar cell and the resulting output is a radiative recombination of carriers causing a light emission in the infra-red range of the electromagnetic spectrum. The intensity of the emitted light is proportional to the local recombination current density that depends on resistive losses on the way. Electrons are injected and diffuse into the p-doped layer of the solar cell. EL images with dark and bright areas are the result of such measurements (Figure 1.7). Regions with poor contacting and inactive regions, i.e. caused by printing, respectively contacting, defects, are highlighted as dark areas (Figure 1.7(a)). Good contacting is bright, the light output increases with the local voltage (Figure 1.7(b)).

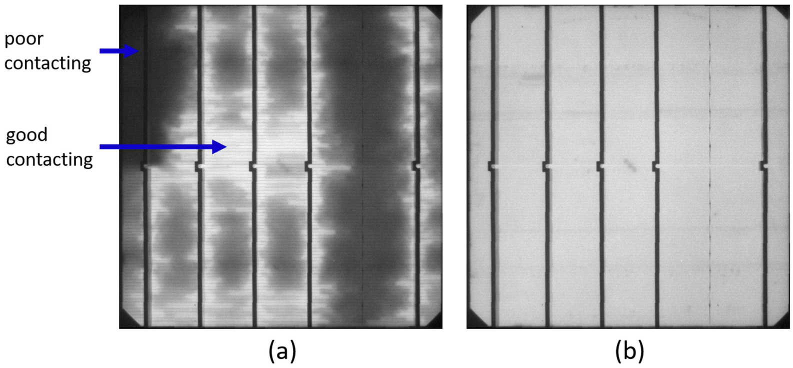

Figure 1.7: Electroluminescence (EL) spectroscopy images of monocrystalline silicon wafers exemplary for (a) poor contacting and inactive regions show up as dark areas and (b) good contacting.

1.3 Aims of this work

This thesis presents an experimental study on highly concentrated conductive silver pastes. We focus on the paste formulation, respectively their rheological properties, to apply ultra-fine electrodes for the front-side metallization of Si solar cells. We work on different measuring methods for the flow behavior characterization of silver pastes. Therefore, we investigate various formulation series as well as concepts with volatile components. We also examine their performance with different printing technologies to manufacture ultra-fine electrodes and present their applicability.
The following main part of this work is divided into three sections:

I. Rheological characterization of highly concentrated suspensions

We observed a lack of a detailed rheological characterization of complex, highly concentrated suspensions since aforementioned measurement artifacts like wall slip, shear banding and sample spillage occur. A comprehensive rheological characterization of highly concentrated suspensions or pastes is mandatory for a targeted product development meeting the manifold requirements during processing and application of such complex fluids. Our first challenge is to work out a protocol for reliable rheological characterization of these complex fluids. Preliminary experiments demonstrated different results obtained from same measuring settings but changed measuring geometries. Protocols for a robust and meaningful characterization of the flow behavior of concentrated silver pastes can be defined with the help of video recordings showing the true sample deformation at the rim of the rheometer fixture. This motivated us to develop a script for rheological characterization of such complex fluids.

II. Rheology and screen-printing performance of metallization pastes

The challenge in front-side metallization of Si solar cells is to print uniform fine lines with a high aspect ratio to achieve higher efficiencies simultaneously with reduced consumption of raw materials. An in-depth understanding of the relationship between paste composition, rheology and screen printed line morphology is essential. The successful application of the above obtained protocol on different silver paste formulations is the next challenge. Rheological measurements and printing experiments are performed with the same pastes and changed printing conditions, i.e. printing speed and finger width profile. Parameters essential for a correlation of rheology and screen-printing behavior should be worked out to investigate the dominating properties providing a prediction of printability of fine finger lines.

III. Alternative paste formulation concept for front-side metallization of Si solar cells

This part of the thesis focuses on the formulation of competitive silver pastes based on the capillary suspensions concept without the addition of non-volatile components. In a previous work [28], a twofold increase of conductivity compared to thick film layers produced from commercial silver pastes under identical conditions could be gained with this formulation concept. Our motivation is to demonstrate that the development of a highly conductive, non-volatile free silver paste formulation consisting of only four components, silver particles, glass frit and two immiscible fluids is suitable for the front-side metallization of Si solar cells. First experiments on an industrial pilot line revealed almost comparable cell efficiencies for printed and fired monocrystalline Si solar cells at approximately 15 % reduced silver laydown presumably due to the missing residual carbon impurities in the printed and fired finger lines (see Appendix, chapter 7, Figure 7.1). Saving the material costs and at the same time increasing the efficiency is the motivation for optimizing the electrode morphology. Furthermore, we aim at demonstrating the versatile application possibilities for front-side metallization with emerging printing technologies. Si solar cells are still by far dominating solar energy harvesting technology and new concepts potentially improving the efficiency of that technology are highly demanded.

1.4 Outline of this work

Chapter 1 includes a general introduction representing the state-of-the-art, respectively the motivation of this thesis. A brief overview of the solar cell concept as well as different application technologies for front-side metallization relevant for this work are discussed. The main part of this thesis is the development of a new paste formulation concept with the focus on non-volatile free silver paste formulation for front-side metallization of Si solar cells including the rheological characterization of such complex, highly concentrated suspensions. The fundamentals of the capillary suspension concept is also discussed in this introductory chapter. State-of-the-art regarding rheological properties and characterization methods of silver pastes for industrial metallization with screen-printing is appropriately documented. Subsequently, we give an overview and a brief explanation of parameters obtained from cell performance characterization of printed and fired cells, as well as a brief explanation of electroluminescence spectroscopy imaging. The aims and the outline of this work are closing this chapter.

Chapter 2 presents an important part of this thesis and describes how to conduct appropriate measurements in order to characterize rheological properties of highly concentrated silver pastes. The results were published in the peer-reviewed *Journal of Visualized Experiments*. Rheological characterization of up-to-date commercial silver pastes for front-side metallization is a particular challenge. This measuring protocol for a conclusive assessment of different process relevant rheological parameters, i.e. yield stress, viscosity at low and high shear rates, wall slip velocity, structural recovery after large deformation and elongation at break as well as tensile force during filament stretching, are evaluated. A rotational shear rheometer with a parallel-plate sample fixture is used in this study. The importance of concomitant video recordings during parallel-plate rotational rheometry for a significant determination of rheological quantities is demonstrated. These video recordings enabled assessment of secondary flow phenomena such as plug flow, wall slip, and shear banding which depend on the plate roughness in a non-trivial manner and limit rheological measurements. Results strongly depend on the employed experimental setup, and particularly on the surface energy and roughness of the sample fixtures. We developed a detailed experimental protocol addressing all aspects of a reliable rheological characterization of highly concentrated pastes.

Chapter 3 covers the rheology and screen-printing performance of front-side metallization pastes. We apply the above mentioned measuring protocol for a meaningful characterization of three model silver pastes suitable for front-side metallization of Si solar cells, and the corresponding vehicles mainly differing with respect to the concentration of thixotropic agent. We investigate their rheological properties, i.e. yield stress, viscosity, storage modulus, wall slip behavior, structural recovery, and fracture strain, using steady and oscillatory shear and elongational flow rheometry. Afterwards screen-printing tests are performed at various printing speed through a layout screen including line widths between 20 and 55 μm. Printing performance is characterized by the analysis of dried electrodes with respect to line width, aspect ratio, and cross-sectional area with a 3D laser scanning microscope. We compare the results obtained from rheological characterization with that from electrode morphology determination to screen possible correlations. The results were published in the peer-reviewed journal *Coatings*.

Chapter 4 includes the development of non-volatile free paste formulation based on the capillary suspensions concept presenting a versatile, cost-effective formulation platform. The pastes are made of silver particles, glass frit, and two immiscible fluids. The secondary fluid added in small fractions induces the formation of a percolating particle network providing extended shelf-life. Based on the type and amount of added secondary fluid flow behavior of these pastes is adjusted in a wide range as demanded by the respective printing process without further addition of non-volatile rheology control agents. Such pastes are successfully applied on monocrystalline (Cz), respectively multicrystalline (mc), Si-wafers using standard screen printing, as well as emerging technologies such as knotless screen design or the Pattern Transfer Printing^{TM} technology. The matureness of additive-free paste formulation is demonstrated regarding the printability with these different printing technologies. A finger width study is performed to investigate the printing behavior right after printing, drying and firing of screen-printed electrodes. Furthermore, this chapter 4 includes the real-time observation of the screen-printing process using a high-speed imaging system inserted into a screen printer to visualize the paste spreading kinetics during screen-printing on a glass substrate. Morphology and electrical cell properties are characterized employing a 3D laser scanning microscopy and a solar simulator as well as electroluminescence spectroscopy. Results are compared to these obtained using commercial paste formulation including the same silver particles and glass frit. This part of the work has been submitted for publication to the peer-reviewed journal *Solar Energy Materials and Solar Cells*.

A final summary and an outlook regarding the development of silver paste formulation and printing technologies for future research are given in chapters 5 and 6. Including the ideas and potential next steps resulting from the main results obtained from this thesis.

2. Rheological characterization of highly concentrated complex fluids

Full title:	Challenges in rheological characterization of highly concentrated suspensions - A case study for screen-printing silver pastes [95]
Authors:	Ceren Yüce, Norbert Willenbacher
Status:	published
Bibliographic data:	J. Vis. Exp. (122), e55377; doi:10.3791/55377 (2017)

Consider the explicit permission to use the JoVE article 55377 “Challenges in Rheological Characterization of Highly Concentrated Suspensions - A Case Study for Screen-printing Silver Pastes” in the authors thesis.

Abstract

A comprehensive rheological characterization of highly concentrated suspensions or pastes is mandatory for a targeted product development meeting the manifold requirements during processing and application of such complex fluids. In this investigation, measuring protocols for a conclusive assessment of different process relevant rheological parameters have been evaluated. This includes the determination of yield stress, viscosity, wall slip velocity, structural recovery after large deformation and elongation at break as well as tensile force during filament stretching.

The importance of concomitant video recordings during parallel-plate rotational rheometry for a significant determination of rheological quantities is demonstrated. The deformation profile and flow field at the sample edge can be determined using appropriate markers. Thus, measurement parameter settings and plate roughness values can be identified for which yield stress and viscosity measurements are possible. Slip velocity can be measured directly and measuring conditions at which plug flow, shear banding or sample spillover occur can be identified clearly.

Video recordings further confirm that the change in shear moduli observed during three stage oscillatory shear tests with small deformation amplitude in stage I and III but large oscillation amplitude in stage II can be directly attributed to structural break down and recovery. For the pastes investigated here, the degree of irreversible, shear-induced structural change increases with increasing deformation amplitude in stage II until a saturation is reached at deformations corresponding to the crossover of G' and G'', but the irreversible damage is independent of the duration of large amplitude shear.

A capillary breakup elongational rheometer and a tensile tester have been used to characterize deformation and breakup behavior of highly filled pastes in uniaxial elongation. Significant differences were observed in all experiments described above for two commercial screen-printing silver pastes used for front side metallization of Si solar cells.

Keywords

rheological characterization; highly concentrated suspension; silver paste; video recordings; wall slip; shear banding; plate roughness; elongation

Video Link

The video component of this article can be found at:
URL: https://www.jove.com/video/55377/

2.1 Introduction

Front-side metallization of silicon (Si) solar cells is commonly realized using traditional screen-printing. Besides stencil printing, inkjet printing and flexographic printing [35], screen-printing has been used since the 1970s for numerous printing applications [4]. It is a versatile technique and in solar cell production, it ensures simple and fast metallization at a low printing cost. However, the flow properties of screen-printing pastes have to be carefully adjusted to guarantee undisturbed, defect free processing. This is particularly challenging in solar cell metallization since narrow uniform line patterns have to be achieved. Furthermore, paste recipes have to be carefully adjusted to avoid sedimentation of the high density silver particles, phase separation and particle aggregation.

The highly concentrated conductive screen-printing pastes for front-side metallization of solar cells mainly consist of three components [12, 49, 50, 51]: the conductive material, generally micron-sized silver particles providing good electrical conductivity [52, 53]; the continuous phase, the so-called vehicle, a mixture of organic binders, solvents and additives promoting particle wetting, film formation and adhesion to the substrate that also includes additives to adjust the flow behavior, especially allowing the paste to pass the narrow screen meshes easily; and the inorganic binder (glass powder) acts as an adhesion promoter and activates the sintering process at lower temperatures.

Printing fine lines with a high aspect ratio requires silver pastes that exhibit a high yield stress and a pronounced shear-thinning behavior [71]. The high yield stress guarantees good shape accuracy and a high aspect ratio whereas strong shear thinning and a correspondingly low viscosity at high shear rates are necessary when the paste flows through narrow mesh openings, where the paste is exposed to high shear rates estimated to be beyond $10^3\ s^{-1}$ [18].

During the printing process, pastes are exposed to very different deformation rates and stresses. First, the paste rests on the screen; then the squeegee acts and the paste penetrates through screen openings onto the substrate. After application of the paste on the silicon wafer, structure and viscosity must recover quickly to prohibit paste spreading on the substrate. This would reduce solar cell performances due to higher shading losses [18, 20, 73, 74, 75, 76]. Interruptions, the so-called meshmarks, in printed finger lines can occur at cross points of mesh wires depending on paste rheology. The time for leveling out the meshmarks should be as long as necessary but also short enough to keep the finger line spreading as low as possible [77].

The squeegee pressure required for the paste to flow through the meshes onto the substrate has to be adjusted carefully to the high yield stress necessary to provide good shape accuracy [12, 25, 51, 71, 72]. Particles are closely packed, interact strongly and form complex structures. Accordingly, besides yield stress, shear thinning and thixotropy, various other complex flow phenomena like shear banding or avalanching may occur in such suspensions [78, 79, 80]. Wall slip is also crucial to concentrated suspensions [81, 82, 83, 84]. A thin layer of liquid of lower viscosity, i.e. a layer depleted or free of particles is formed next to the wall [84, 85, 86, 87, 88, 89, 90] and may control flow through narrow gaps or channels.

So a comprehensive rheological characterization of screen-printing pastes is essential in order to improve processing properties and product features. In this study, two commercial silver pastes are characterized. These pastes exhibit substantially different printing performances. The rheological characterization of such materials is very demanding. Even the simple determination of the steady shear viscosity using a rotational rheometer is a major challenge due to wall slip, plug flow, shear banding and paste spill. Accordingly, previous studies focused on oscillatory shear measurements [18, 25, 80] or on the characterization of low concentrated silver pastes, so-called inks [12, 51, 76], for which the above-mentioned phenomena are unlikely to occur.

Protocols for a robust and meaningful characterization of the flow behavior of concentrated silver pastes can be defined with the help of video recordings. A rotational shear rheometer with a parallel-plate sample fixture is used in this study, clearly demonstrating that plug flow, wall slip, and shear banding depend on the plate roughness in a non-trivial manner.

In previous work, time-dependent development of wall slip in steady torsional flow of concentrated suspensions was examined for different plate roughness. The flow of highly concentrated suspensions of solid glass spheres in polymer binder solution was visualized and an increased plate or inner cylinder roughness prevented wall slip. However, increasing plate roughness resulted in fracture of the samples [81, 84]. Fracture occurred at smaller apparent shear rates when the wall roughness was increased. The tips of the asperities of the roughened surfaces might act as stress concentration points at the plate surface, initiating fracture at shear stresses τ smaller than the yield stress τ_y [84].

Wall slip is considered to be important for the screen-printing performance of highly concentrated pastes. The paste glides through the mesh easier at higher wall slip and its deposit on the substrate is increased significantly [26]. With the help of video recordings, wall slip can be directly observed for different experimental protocols. The slip velocity can be determined directly from the angular velocity of the rotating plate using smooth plates with low roughness. But flow behavior determination on silver pastes is an inherent limitation. The suspensions are non-transparent, so optical flow field observations can only be done at the sample rim. Previous studies have tried to determine wall slip and deformation within the samples simultaneously. They observed slip below the yield stress and found a quadratic dependence of slip velocity on the shear stress. The flow behavior of transparent clay suspensions was investigated by Pignon [86] following the deformation of a dye pigment line injected into the bulk material. Persello et al. [85] have investigated concentrated aqueous silica suspensions. They found that increasing plate roughness to suppress wall slip does not result in a homogeneous sample deformation but provoked bulk fracture. Slip and sample deformation in pastes of soft microgel particles and concentrated emulsions have been intensively discussed in a series of papers [87, 88, 89, 90]. Fluorescent tracer particles were used to determine the flow field within these transparent samples in a cone-plate geometry. They found a characteristic slip velocity V^* at the yield stress of the respective material and a power law for the increase of slip velocity with shear stress τ below τ_y. An exponent of one was found for non-adhering particles and two in the case of weak attraction between particles and wall.

In the study presented here the development of deformation and flow under controlled stress and controlled shear rate conditions is monitored. In contrast to the findings reported in [84], increasing plate roughness does not result in fracture for both investigated pastes. Also, wall slip and plug flow cannot be suppressed just by increasing plate roughness. These phenomena seem to be controlled by the ratio of particle size and plate roughness. Sample spill sets in at a characteristic rotational speed presumably determined by the balance between centrifugal forces acting on and friction at the rheometer plate. However, the shear rate range in which the viscosity determination is possible can be determined, and simultaneously wall slip can be quantified. Furthermore, a capillary rheometer is used to determine the viscosity at higher shear rates relevant for the printing process.

Despite the difficulties with steady shear rheometry, well-defined oscillatory shear deformation can be implemented easily. A three-stage oscillation test (constant frequency, different oscillation amplitudes) simulates the screen-printing process [18] and allows for studying structural recovery of the paste:

In the “first pre-print” step, a small deformation is applied to determine the elastic and viscous properties at rest. The second “print” step simulates the blade coating and the paste passing the screen mesh by applying a sufficiently high deformation amplitude breaking the paste structure. In the final “post-print” step, a small deformation is applied to detect the structural recovery of the paste. The initial modulus value should be reached quickly to avoid paste spreading but not too fast to avoid meshmarks. The investigations presented here confirm that the structural recovery is incomplete as previously reported by Zhou [80]. Zhou could show that the structural change is caused by the breaking of filler clusters of filler-matrix decoupling using silver particles suspended in ethyl cellulose solution. Video recordings in this study reveal that the observed irreversible structural change is not an artefact related to the occurrence of wall slip, shear banding, plug flow or sample spill. Additionally, it is found that the degree of structural breakdown strongly depends on the deformation amplitude applied in stage two, but hardly depends on the time interval of the applied strain. This aspect was not perceived in the experiments of Zhou. The influence of the paste composition on structural breakdown and recovery will be discussed in a subsequent paper.

Finally, a method to simulate the paste behavior during screen snap-off is presented. A capillary breakup elongational rheometer and a commercial tensile tester are used to determine the stretch ratio at which the pastes break and the maximum axial force during stretching as a function of elongation velocity.

Video recordings have turned out to be indispensable for finding the appropriate measurement protocols necessary for a meaningful rheological characterization of silver pastes using parallel-plate rotational rheometry. Video data enabled the determination of shear rate and shear stress regimes in which physically well-defined yield stress and viscosity values could be determined. The appropriate choice of plate roughness and plate separation parameters was also based on these video recordings. Experimental settings for which wall slip, pure plug flow, shear banding or sample spillage occur could be unequivocally identified. The pastes investigated here are used for front-side metallization of solar cells. However, a careful video supported rheological characterization is also important for various other kinds of concentrated suspensions including high density, micron-sized particles.

2.2 Protocol

Caution: Please consult all relevant material safety data sheets (MSDS) before use. Several of the components used for the silver paste formulation are acutely toxic, carcinogenic and water-endangering substances. Please use all appropriate safety practices when handling with silver pastes (personal protective equipment - safety glasses, gloves, lab coat, full length pants, closed-toe shoes). Also working with the rheometer requires carefully work. Protect the hands from being trapped during the geometric moves to the measuring position.

2.2.1 Rotational shear measurements - Measurement report

1. Apparent viscosity determination - shear rate controlled measurements

   1. Carry out rotational shear experiments using rheometer A with parallel-plate geometry (plate roughness $R_q = 2\text{-}4\ \mu m$, plate diameter $d = 25\ mm$). The required paste volume is 0.49 mL.

      1. Adjust the measuring settings for viscosity determination. Carry out measurements in stepwise controlled shear rate mode $\dot{\gamma} = 0.01\text{-}1000\ s^{-1}$ in 40 steps. The measuring time is 1200 s.

      2. Place the equipment for recording the measuring gap in position: camera tripod with the attached endoscopic camera, LED spotlight,

   and the external computer to save the recordings. Adjust the endoscopic camera settings, e.g. contrast and brightness of the exposure field.

   3. Just before filling up the rheometer gap, mix the sample in the reservoir so the paste is blended homogeneously.

   4. Fill up the rheometer gap with the mixed silver paste sample.
      NOTE: For a measuring gap height of $h_{end} = 1\ mm$, first go to a gap position $h_1 = 1.05\ mm$ for removing the excess sample from the edge of the rheometer geometry. After clearing up the excess sample, change the actual gap height position from h_1 to h_{end}.

   5. To visualize the paste flow in the measuring gap, mark the paste with soot particles in a vertical line.

   6. Before starting the measurement, wait about 5 min until normal forces in the gap have decayed.

   7. Start the measurement. Start the measuring device and video recording at the same time to follow the paste in the gap and to correlate measuring settings, rheometry results, and video recordings correctly.

   8. Repeat the measurement steps 1.1.3 - 1.1.7 at least three times.

   9. Plot the apparent viscosity η_{app} vs. apparent shear rate $\dot{\gamma}_{app}$ logarithmically. Evaluate the video recordings to check the section of dominating wall slip, the section of paste deformation, and the section of sample spill. The parameter settings for which a uniform shear profile is formed can be detected easily based on the video recordings (Figure 2.1).
      NOTE: The shear stress at the edge of the plate is calculated from the recorded torque applied by the rheometer and the apparent shear rate at the edge of the plate at steady state. The apparent shear rate is referred to the angular velocity Ω of the plate and to the gap height h at the maximum plate radius.

2. Yield stress determination - a comparison of shear stress controlled measurements with different plate roughness and vane geometry

   1. Yield stress measurement with a plate roughness $R_q = 1.15\ \mu m$.

      1. For measurements with $R_q = 1.15\ \mu m$, use rheometer B with a plate diameter of $d = 20\ mm$. The required paste volume is 0.31 mL.

      2. Adjust the measuring settings for yield stress measurement. Carry out measurements in stepwise controlled shear stress mode. Vary

the shear stress between 1 Pa to 3000 Pa in 35 steps with a total measuring time of 1050 s.

3. Assemble a camera tripod with the attached endoscopic camera, a LED spotlight, and the external computer with software to save the video recordings. Adjust the endoscopic camera settings, e.g. the contrast and brightness of the exposure field.
4. Before filling the measuring gap with silver paste, mix the sample in its reservoir to ensure that it is blended homogeneously. Use a speed mixer (30 s at 1000 rpm). After mixing, fill up the gap with paste.
5. Take a small amount of the blended paste, apply it to the bottom plate of the parallel-plate rheometer and bring the upper plate to a measuring position.
   NOTE: For a measurement with gap height $h_{end} = 1\ mm$, first go to gap position $h_1 = 1.05\ mm$ and remove the excess sample from the edge of the rheometer geometry. After clearing up the excess sample, change the actual gap height position from h_1 to h_{end}.
6. Mark the paste in the measuring gap with soot particles in a vertical line. This enables visualization of the paste deformation and flow in the gap as well as the wall slip.
7. Before starting the measurement, wait about 5 min until the normal force on the upper plate has vanished.
8. Start the measurement now. Start the measuring device and video recording at the same time to follow the paste in the gap and to attribute the correct measuring settings to video recordings.
9. Continue the measurement until the paste is spilled out of the gap.
10. Repeat the measurement in total for three times. For each measurement, clean the measuring gap with ethanol and repeat steps 2.1.4 - 2.1.9.
11. When the measurement is finished, plot the deformation γ vs. shear stress τ logarithmically and determine the yield stress of the medium using the tangent intersection point method [96].

2. Yield stress measurement at a plate roughness of R_q = 2-4 μm.
   1. For measurements with R_q = 2-4 μm, use rheometer A with a plate diameter of $d = 25\ mm$. The required paste volume is 0.49 mL.
   2. Repeat the steps 2.1.2 - 2.1.11 for yield stress measurements with a plate roughness R_q = 2-4 μm.

3. Yield stress measurement at a plate roughness of $R_q = 9\ \mu m$.
    1. For measurements with $R_q = 9\ \mu m$, use rheometer B with a plate diameter of $d = 20\ mm$ and required paste volume is 0.31 mL. Use double faced adhesive tape to attach pieces of sandpaper to the plates matching their diameter.
    2. Repeat the steps 2.1.2 - 2.1.11 for yield stress measurements with a plate roughness $R_q = 9\ \mu m$.
4. Yield stress measurement with the vane geometry.
    1. For yield stress measurements with the vane geometry, use rheometer C.
    2. Adjust the measuring settings for yield stress measurement. Carry out the measurements in stepwise controlled shear stress mode like parallel-plate measurements in 2.1, 2.2 or 2.3. The parameter values are τ = 1-3000 Pa in 35 steps and a total measuring time of 1050 s.
    3. Before filling the cylindrical measuring cup with the sample, mix the sample in its reservoir to ensure that the sample is blended homogeneously. After mixing fill up the cylindrical measuring cup with 10 mL silver paste.
    4. Move the vane geometry to the measuring position and wait 5 min.
    5. Start the measurement now.
    6. For reliable results, repeat the measurement at least three times.
    7. When the measuring is finished, plot the deformation γ versus shear stress τ logarithmically and determine the yield stress using the tangent intersection point method as described above.

3. Wall slip observation
    1. Perform wall slip observations with a plate roughness $R_q = 1.15\ \mu m$ using rheometer B with a plate diameter $d = 20\ mm$.
        1. Adjust the measuring settings for the wall slip determination. Carry out measurements in controlled shear stress mode for selected shear stresses between 400 Pa and 1300 Pa and a measuring time of 300 s total.
        2. Place the equipment for recordings of the measuring gap in position: camera tripod with the attached endoscopic camera, LED spotlight and the external computer to save the recordings. Adjust the endoscopic camera settings, e.g. contrast and brightness of the exposure field.

        3. Before filling the measuring gap with silver paste, mix the sample in its reservoir to ensure that it is blended homogeneously.
        4. Fill up the rheometer gap with the mixed silver paste sample.
        5. Mark the paste in the measuring gap with soot particles in a vertical line for flow behavior observation.
        6. Before starting the measurement wait about 5 min until the normal forces in the gap have decayed.
        7. Start the measurement. Start the measuring device and video recording at the same time to follow the paste in the gap and to correlate measuring settings, rheometry results and video recordings correctly.
        8. Repeat the steps 3.1.3 - 3.1.7 three times for each selected shear stress.
        9. Plot the wall slip velocity v_{slip} vs. shear stress τ to display the wall slip behavior (Figure 2.9).

4. Sample slip investigation during rotational shear measurement

    1. Carry out sample spill investigation with rheometer A (plate diameter $d = 25\ mm$ and required paste volume $0.49\ mL$).

        1. To determine the dependency of the onset of sample spill on gap height h run steps 1.1.1 - 1.1.8 at different gap heights.
        NOTE: For a measurement with
        $h_{end} = 0.2\ mm$ first go to gap position $h_1 = 0.21\ mm$ and remove the excess sample from the edge of the rheometer geometry
        $h_{end} = 0.5\ mm \rightarrow h_1 = 0.51\ mm$
        $h_{end} = 1.0\ mm \rightarrow h_1 = 1.05\ mm$
        $h_{end} = 1.5\ mm \rightarrow h_1 = 1.55\ mm$
        $h_{end} = 2.0\ mm \rightarrow h_1 = 2.05\ mm$.
        2. Present results as a plot of the apparent viscosity η_{app} vs. apparent shear rate $\dot{\gamma}_{app}$ for different gap heights (Figure 2.10). Determine the kink in this curve and the corresponding critical rotational speed n_{crit} and plot this vs. the gap height h (Figure 2.11).

5. Rheological characterization at high shear rates performed with capillary rheometer

    1. Perform capillary rheometer measurements using a nozzle with circular cross-section. Use a nozzle with diameter $d = 0.5\ mm$ and length $L = 40\ mm$ here. The diameter of the feed reservoir is $d_{feed} = 20\ mm$.

1. Adjust the measuring settings (piston velocity between 0.001 $mm\ s^{-1}$ and 20 $mm\ s^{-1}$). Carry out measurements in stepwise controlled shear rate, 5 s for each measuring point.
2. Mix the sample to ensure the paste is blended homogeneously and fill up the feed reservoir with 78.5 mL silver paste.
3. Bring the piston in measurement position and start the measurement.
4. Calculate the shear stress from the pressure difference between sample chamber and capillary outlet. Determine this pressure drop using a 500 bar pressure transducer. Record at least 5 pressure values for each selected piston velocity.
5. Continue the measurement until the feed reservoir is empty.
6. Repeat the measurement (steps 5.1.2 - 5.1.5) three times.
7. Calculate the apparent shear rate from the volumetric flow rate using piston velocity and diameter of the feed reservoir and perform the Weissenberg-Rabinowitsch correction. Calculate the wall shear stress τ_w from the measured pressure difference [97]. The apparent viscosity is then given as $\eta_{app} = \tau_w/\dot{\gamma}_{app}$. Finally, plot the apparent viscosity vs. apparent shear rate to complete the rheological characterization at high shear rates (Figure 2.12).

2.2.2 Oscillatory shear measurement

1. Amplitude sweep

    1. Perform amplitude sweep measurements with rheometer A using a plate diameter of $d = 25\ mm$ and a roughness R_q = 2-4 μm. The required paste volume is 0.49 mL.

        1. Adjust the measuring settings for amplitude sweep measurement. Carry out measurements at controlled deformation amplitude $\hat{\gamma}$ = 0.01-100 % and a constant frequency of $f = 1\ Hz$ in 35 steps.
        2. Repeat steps 2.1.3 - 2.1.8 (section 2.2.1) to complete the amplitude sweep three times. Clean the measuring gap with ethanol before each measurement.
        3. Plot the moduli G' and G'' vs. the deformation amplitude logarithmically (Figure 2.13). The deformation amplitude range in which $G' > G''$ and both moduli run parallel independent of the deformation amplitude $\hat{\gamma}$, is the linear viscoelastic regime (LVE). For structural recovery tests pick one deformation amplitude from this area for

step I and step III. For step II of the subsequent three stage structural recovery test select the deformation amplitude $\hat{\gamma} = 10$ % higher than $\hat{\gamma}_{cross}$ at which $G' = G''$ to ensure a structural break down between the structural recovery tests.

2. Three stage structural recovery test

    1. Perform structural recovery tests with rheometer A equipped using a plate with diameter $d = 25\ mm$ and roughness R_q = 2-4 μm. Use the settings determined in the amplitude sweep experiments (section 2.2.2, 1. Amplitude sweep). The required paste volume is 0.49 mL.

        1. Carry out the three-stage oscillation test with different oscillation amplitudes at constant frequency ($f = 1\ Hz$).
        NOTE:
        Stage I: Small oscillation amplitude within the LVE is applied for a period of 300 s to obtain the shear moduli of the initial state. For paste B $\hat{\gamma}_I = 0.025$ %.
        Stage II: The large strain amplitude ($\hat{\gamma}_{II} = 80$ %) determined in step 1 (section 2.2.2, 1.) is applied in the oscillatory shear mode for $t_{II} = 50\ s$, 150 s or 600 s for time dependence investigations. For deformation dependence investigations the strain amplitudes between $\hat{\gamma}_{II} = 0.025$ % and $\hat{\gamma}_{II} = 100$ % are applied each for constant time ($t_{II} = 150\ s$).
        Stage III: The same small oscillation amplitude like in stage I is applied for 1200 s to follow the recovery over a longer period of time.

        2. Repeat steps 2.1.3 - 2.1.8 (section 2.2.1) to complete three stage oscillation tests three times. Clean the measuring gap with ethanol before each measurement.

        3. Plot the moduli G' and G'' versus time in a semi-log plot (see Figure 2.14 and Figure 2.15(a)).

2.2.3 Stretching behavior determination - A snap-off simulation

1. Stretching behavior measurements with the capillary breakup elongational rheometer

    1. Perform stretching experiments with the capillary breakup elongational rheometer. Use two cylindrical pistons with a diameter $d = 6\ mm$. Stretch

the pastes at varying velocities from the initial gap height $h_0 = 1\ mm$ till the filament breaks.

NOTE: Please note that this is not a typical filament thinning experiment controlled by surface tension. This test can also be done with a screen mesh attached with the emulsion side on the upper piston and a wafer substrate on the bottom. This way printing process during metallization of mono- and multicrystalline industrially pre-processed Si-wafer is mimicked.

1. Adjust the measuring settings for stretching experiments. Vary the stretching velocities (e.g.: 7.5 $mm\ s^{-1}$, 11 $mm\ s^{-1}$ and 110 $mm\ s^{-1}$) to see the change in filament deformation and breakup behavior.
2. Turn on the high speed camera to record the change in filament shape. Set the frame rate to minimum 250 fps and turn on the backlight to trace the filament deformation. Also adjust the high speed camera settings, especially the image sharpness, the contrast and brightness of the exposure field.
3. Before filling the measuring gap with silver paste, mix the sample in its reservoir to ensure the paste is homogeneously blended. After mixing, fill up the measuring gap with paste.
4. Take a small amount (28.3 μL) of the blended paste to apply it on the bottom piston. Bring the upper piston to the measuring position (measuring gap height $h = 1\ mm$) and clean up the excess sample from the edge of the geometry.
5. Start the measuring device and the recordings of the filament deformation at the same time.
6. Repeat the measurement three times. For each measurement, clean the measuring gap with ethanol and repeat steps 1.1.3 - 1.1.5.
7. Choose the first picture showing filament breakage to evaluate the piston position h_{br} at which the filament breaks. Calculate the critical stretch ratio (h_{br} - h_0) / h_0 = Δh_{br} / h_0. Determine this quantity for different stretching velocities (Figure 2.16).

2. Stretching force measurement with the tensile tester

    1. For tensile tester experiments use a piston with a diameter $d = 5\ mm$. Record the resulting tensile force during stretching.

        1. Adjust the measuring settings for stretching experiments. Vary the stretching velocities, e.g. $v = 10\ mm\ s^{-1}$, 20 $mm\ s^{-1}$, 30 $mm\ s^{-1}$,

and 40 $mm\ s^{-1}$ and measure the change in stretching force with a 50 N load cell. Set the initial gap height h to $h_0 = 1\ mm$ and the end position to $h_{end} = 12\ mm$.

2. Before filling the measuring gap with silver paste, mix the sample in its reservoir to ensure the paste is homogeneously blended.
3. Apply the paste to the bottom plate of the tensile tester. Bring the upper plate to the measuring position and clean up the excess sample from the edge of the geometry.
4. Start the measuring device and the recordings of the filament elongation at the same time.
5. Repeat the measurement three times. For each measurement clean the measuring gap and repeat steps 2.1.2 - 2.1.4.
6. From the F vs. Δh data the maximum force F_{max} detected during extension and the stretch ratio at break $\Delta h_{br}\ /\ h_0$ are obtained as shown in Figure 2.17(a). Plot $\Delta h_{br}\ /\ h_0$ vs. the different stretching velocities (Figure 2.17(a)). Plot F_{max} vs. stretching velocity (Figure 2.17(b)).

2.3 Representative results

The viscosity is a key parameter in fluid processing and for multiphase fluids its dependence on shear rate is often determined using parallel-plate rotational rheometry. For highly concentrated suspensions this is neither a straight forward nor a trivial task and the definition of a suitable measuring protocol can be challenging. Here it is demonstrated how highly concentrated silver pastes can be rheologically characterized combining rotational rheometry and video recordings. A robust experimental protocol for determination of the steady shear viscosity is established and the accessible shear rate range is determined. Figure 2.1 represents an overview of apparent viscosity and apparent shear stress vs. the applied apparent shear rate for paste B. The measurement is done with a plate roughness of R_q = 2-4 μm. Cutouts from video recordings permit the division of the obtained flow curve into three sections. In section one wall slip dominates. The upper plate glides without paste deformation. In this section the shear stress is constant. Paste deformation sets in at $\dot{\gamma}_{min,\ app} = 0.07\ s^{-1}$ marking the onset of section two. At the same time the shear stress begins to increase. The deformation of the paste and the stress increase monotonically until section three is reached. At a critical shear rate or angular speed the paste creeps out of the gap and at the same time apparent viscosity and shear stress drop strongly due to the sample spill. Accordingly, the viscosity and shear stress curves exhibit a characteristic kink which occurs at about $\dot{\gamma}_{max,\ app} = 2.5\ s^{-1}$. This $\dot{\gamma}_{max,\ app}$ marks the onset of sample spill. The higher the shear rate the faster the paste is ejected. The viscosity of the paste is accessible only in the shear rate range at $\dot{\gamma}_{min,\ app} < \dot{\gamma}_{app} < \dot{\gamma}_{max,\ app}$. However, since the deformation inside the gap is not known and a priori must not be the same as observed at the rim the viscosity data even in that nominal shear rate range has to be treated as the apparent values. The shear stress τ_{app} at the rim of the plate r_{max} is calculated from the applied torque M in the following way $\tau_{app} = M\ (2\pi r_{max}^3)^{-1}\ [3 + d(\ln M)\ /\ d(\ln \dot{\gamma}_{app})]$. The apparent shear rate $\dot{\gamma}_{app}$ at the edge of the plate is calculated from the angular velocity Ω of the plate and the gap height h according to $\dot{\gamma}_{app} = \Omega\ (r_{max}\ /\ h)$ [97]. Since the true deformation and stresses inside the gap are not known these calculated stress and shear rate values have to be treated as apparent or nominal values.

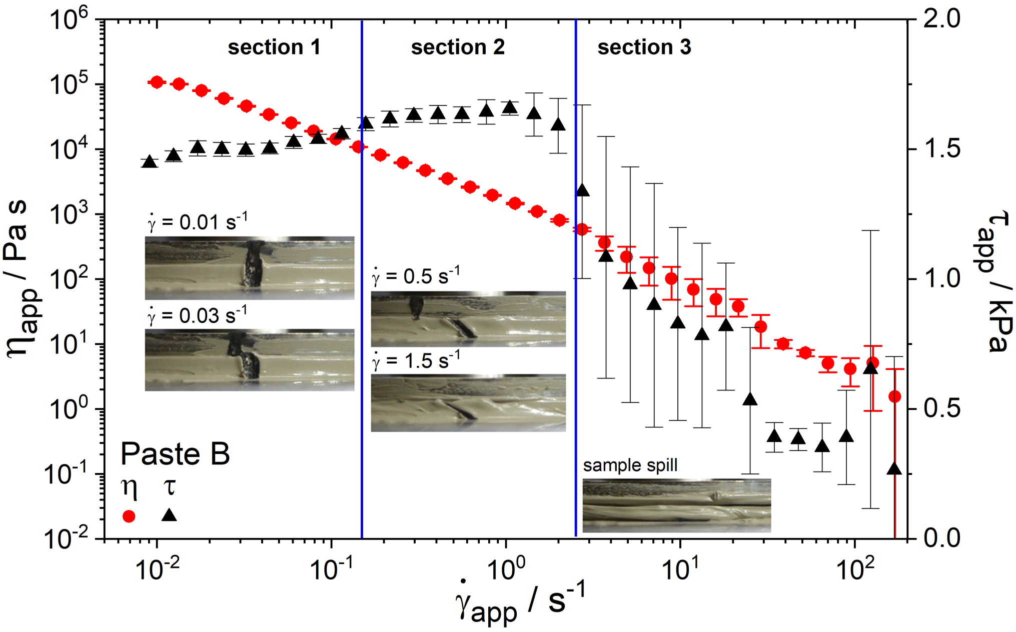

Figure 2.1: **Apparent viscosity in controlled shear rate parallel-plate rotational rheometry.** Overview of the resulting apparent viscosity and shear stress measured in controlled shear rate mode with a parallel-plate rheometer (short: PP, plate roughness R_q = 2-4 μm and gap height $h = 1\ mm$. Classification of apparent shear rate in three sections based on video recordings during measurement. Wall slip, paste deformation and sample spill are highlighted in the video recording cutouts. Paste B is chosen exemplarily here, but similar results were obtained for paste A. The error bars are calculated as the standard deviation obtained from at least three independent measurements.

In soft matter often a critical stress, the so-called apparent yield stress $\tau_{y,\ app}$, is found at which a transition from an elastic reversible deformation to irreversible flow is observed. This yield stress is a key factor in paste formulation regarding classical screen-printing as well as emerging additive manufacturing techniques. A high yield stress is desirable to ensure shape accuracy after printing. Generally, the yield stress is determined from the kink in the deformation vs. shear stress curve using the tangent intersection method as exemplarily shown in Figure 2.2. Often this is done using a so-called vane geometry guaranteeing reliable and significant results without the effect of slip [98, 99]. Measuring the yield stress with the parallel-plate geometry is another option which has to be carefully validated. Wall slip or shear banding phenomena often observed in highly filled suspensions may interfere with the yield stress evaluation. Therefore, the effect of plate roughness on $\tau_{y,\ app}$ determination is investigated. Results for the yield stress values obtained for paste A and B in stress sweep experiments at different plate roughness are shown in Figure 2.3.

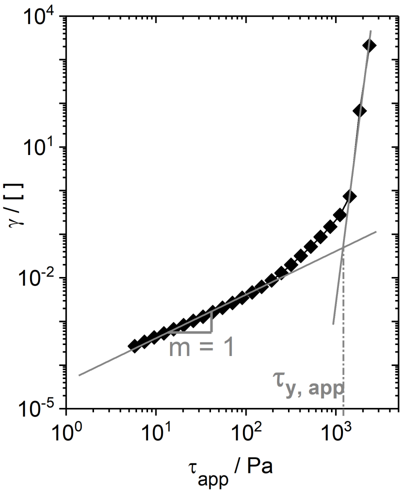

Figure 2.2: **Applying the tangent intersection point method for yield stress determination.** The deformation γ, i.e. the displacement of the upper plate divided by the gap height, is plotted versus the applied nominal shear stress τ_{app}. The shear stress controlled measurement is done with a plate roughness R_q = 2-4 μm and a gap height $h = 1\ mm$. Paste B is chosen exemplarily here, but similar results were obtained for paste A.

Increasing the plate roughness causes an increase in calculated yield stress, whereas the variation in gap height h does not affect determination of this quantity. Figure 2.4 displays cutouts of the video taken for paste A at a plate roughness of R_q = 1.15 μm and a gap height of $h = 1\ mm$. Soot particles were placed on the sample rim as a marker and endoscopic video imaging was used to characterize the deformation at the sample rim. The paste glides on the bottom plate at stresses up to $\tau_{app} = 600\ Pa$ while it sticks to the upper plate. A plug flow is formed in the measuring gap, i.e. the sample is not deformed and the determination of a yield stress or viscosity is pointless even though a kink in the corresponding apparent deformation vs. shear stress curve seems to imply a transition from elastic deforma-

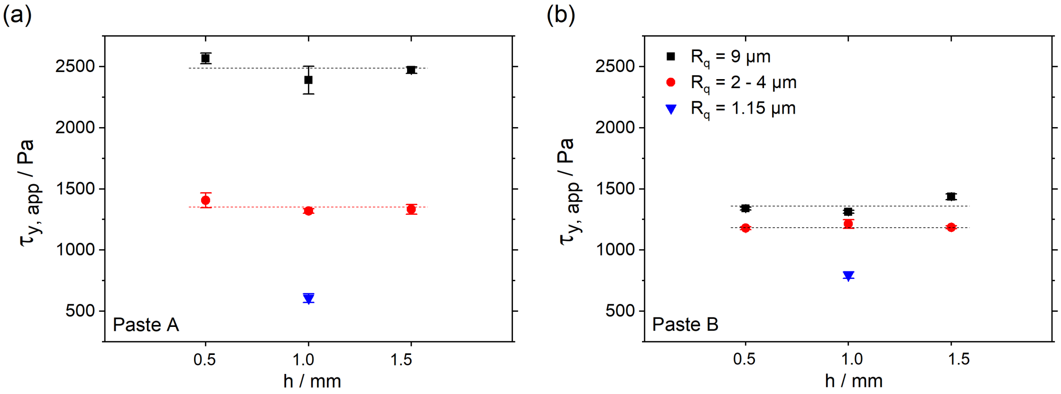

Figure 2.3: **Effect of plate roughness on apparent yield stress.** The resulting apparent yield stress for different plate roughness $R_q = 1.15$ μm, $R_q =$ 2-4 μm, and $R_q = 9$ μm vs. gap height h. Results depend on the plate roughness R_q and is independent of varying the measuring gap height (left: paste A, right: paste B). The error bars are calculated as the standard deviation obtained from at least three independent measurements.

tion to viscous flow. Similar behavior is obtained for other gap heights for paste A as well as paste B. So a plate roughness of $R_q = 1.15$ μm is not appropriate for the determination of yield stress or viscosity of such highly filled silver pastes. In contrast, for a plate roughness $R_q =$ 2-4 μm (as declared by the manufacturer) video imaging confirms the formation of a shear deformation profile at the rim (Figure 2.5) as necessary for a reliable and well-defined rheological measurement.

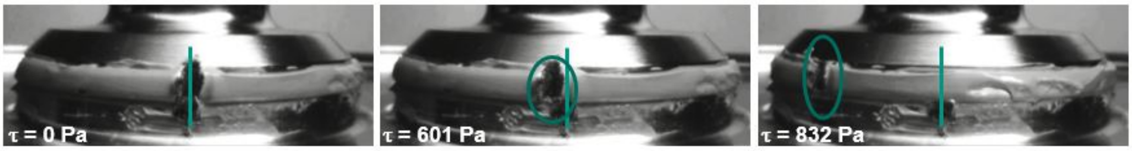

Figure 2.4: **Cutouts from video recordings at varying shear stress.** Here using the example of paste A measured with plate roughness $R_q = 1.15$ μm.

Figure 2.5: **Cutouts from video recordings at varying shear stress.** Here using the example of paste A measured with plate roughness $R_q =$ 2-4 μm.

Plug flow is avoided and for paste A uniform flow sets in at $\tau_{app} = 1360$ Pa. Similar flow behavior was observed for paste B. So this choice of plate roughness allows for a reliable yield stress measurement. Choosing a higher plate roughness

$R_q = 9\ \mu m$ results in higher yield stress values than obtained for plate roughness $R_q = 1.15\ \mu m$ and $R_q = 2\text{-}4\ \mu m$. This effect is much more pronounced for paste A than for paste B. The video recordings show that no shear profile is formed with paste A during this measurement (Figure 2.6).

At a stress $\tau_{app} = 1880\ Pa$ the upper plate starts moving without paste deformation. A stress of $\tau_{app} = 2605\ Pa$ causes gliding of the paste on the bottom plate still without paste deformation. The critical stress corresponding to the kink in the deformation vs. stress curve does not mark the transition from elastic to viscous deformation, i.e. it is not the apparent yield stress. Instead it marks the onset of slip and plug flow and has to be considered as critical slip stress τ_{slip}. In contrast, no plug flow was observed for paste B using the $R_q = 9\ \mu m$ plate (Figure 2.7).

The deformation of the paste starts at $\tau_{app} = 1430\ Pa$ and is fully developed at $\tau_{app} = 1597\ Pa$. At higher shear stress ($\tau_{app} = 1880\ Pa$) shear banding occurs, i.e. only an intermediate narrow layer of the sample is sheared. The yield stress obtained from the deformation vs. stress data with the $R_q = 9\ \mu m$ plate is close to that obtained with $R_q = 2\text{-}4\ \mu m$ in case of paste B, but it is pointless to use this rough plate for $\tau_{y,\ app}$ determination of paste A.

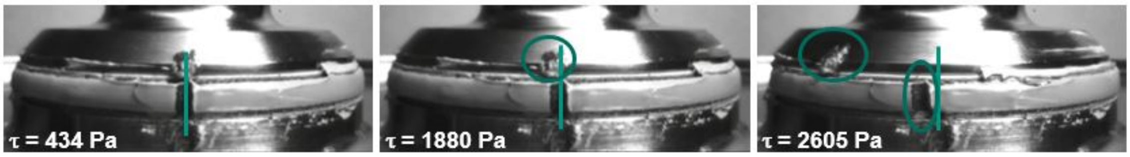

Figure 2.6: **Cutouts from video recordings at varying shear stress.** Here using the example of paste A measured with plate roughness $R_q = 9\ \mu m$.

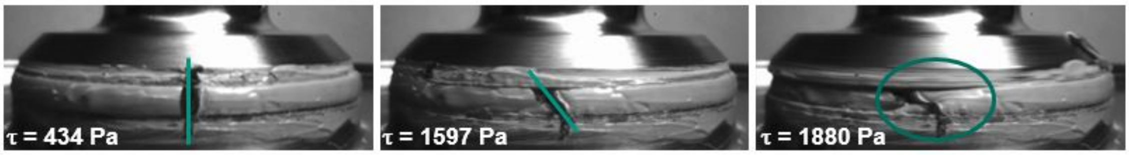

Figure 2.7: **Cutouts from video recordings at varying shear stress.** Here using the example of paste B measured with plate roughness $R_q = 9\ \mu m$.

To double-check the parallel-plate $R_q = 2\text{-}4\ \mu m$ results, the yield stress was also measured with the vane geometry. This geometry is inherently not affected by wall slip effects and the onset of rapid vane rotation at a certain applied stress is unequivocally related to the structural breakdown within the paste in the cylindrical plane defined by the diameter of the vane [98, 99]. Figure 2.8 shows that the results obtained using the vane geometry agree very well with those obtained from parallel-plate rheometry with $R_q = 2\text{-}4\ \mu m$. Based on the findings presented above, all further experiments were performed using a plate with roughness R_q = 2-4 μm except for the wall slip velocity measurements. The plates with roughness R_q = 1.15 μm and R_q = 9 μm cannot be recommended for yield stress and viscosity determination of silver pastes or other highly filled suspensions similar to those investigated here. Finally, it is stated that the yield stress of paste A is higher than that of paste B.

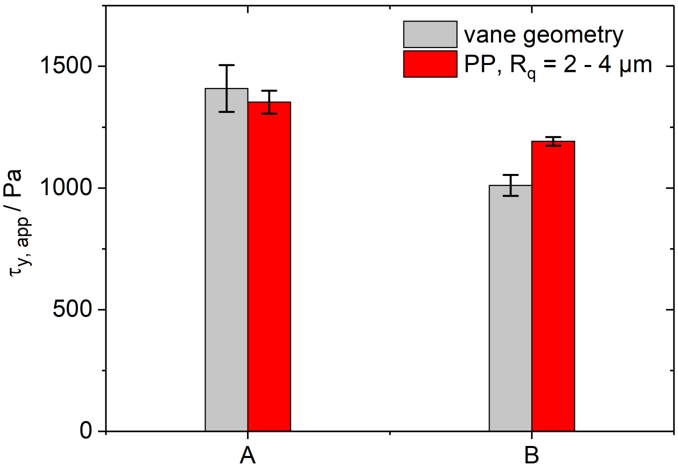

Figure 2.8: **Resulting yield stress.** A comparison of the yield stress for paste A and B determined with the vane geometry and the R_q = 2-4 μm parallel-plate geometry. The error bars are calculated as the standard deviation obtained from at least three independent measurements.

Wall slip is another important parameter for successful printing. The higher the wall slip, the better the paste flows through the screen mesh openings [26]. The wall slip velocity, i.e. the relative velocity of the moving plate and the adjacent paste layer, can be evaluated directly from video recordings irrespective of plug flow or shear deformation prevailing in the gap. A smooth upper plate and a rough bottom plate have to be used when performing these experiments [84, 86, 87, 89]. If the sample within the gap is at rest, the slip velocity is directly given by the speed of the upper plate. Figure 2.9 displays the wall slip velocity vs. shear stress as determined under this latter conditions using a plate with $R_q = 1.15$ μm. Slip clearly occurs at stresses far below the yield stress similar as observed for concentrated emulsions and pastes of soft microgel particles [87, 88, 89]. For paste A, higher wall slip velocities are obtained than for paste B irrespective of applied stress. In both cases, slip velocity increases linearly with applied stress. However, the obtained slope $m_A = 0.33$ μm $(Pa\ s)^{-1}$ for paste A is nearly three times higher than the slope $m_B = 0.12$ μm $(Pa\ s)^{-1}$ obtained for paste B. Similar as observed previously [87, 88, 89], a characteristic slip velocity V^* at about a stress level corresponding to the yield stress is found and above τ_y slip is hardly measurable. For paste A and B, $V_A^* = 0.37$ mm s^{-1} and $V_B^* = 0.11$ mm s^{-1}, respectively.

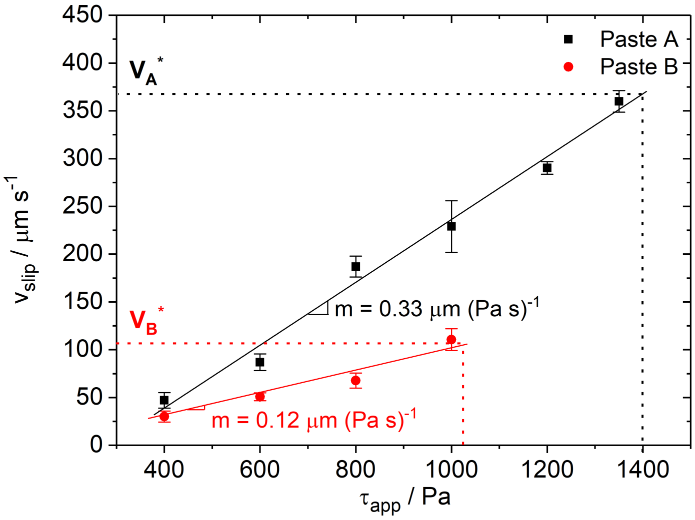

Figure 2.9: **Dependence of wall slip on shear stress.** Wall slip velocity v_{slip} vs. shear stress τ for paste A and B determined with $R_q = 1.15\ \mu m$ parallel-plate geometry at gap height $h = 1\ mm$. The characteristic wall slip velocity obtained at the yield stress of the material is indicated as V^*. The error bars are calculated as the standard deviation obtained from at least three independent measurements.

The sample spillover is attributed to the strong centrifugal force acting on the high density micron-sized particles and should therefore be controlled by the angular or rotational speed n_{crit} at which the centrifugal force dominates over viscous friction. To test this, the measuring gap height h was increased from 0.2 mm to 2 mm. The intensity of sample spillover increases with gap height h and shear rate. The wider the gap height the earlier sample spill sets in, i.e. $\dot{\gamma}_{crit}$ is lower (Figure 2.10).

Figure 2.11 demonstrates that sample spill sets in at a critical angular speed n_{crit} irrespective of sample height h between 0.5 mm and 2 mm. For paste A, the critical rotational speed is $n_{crit,\ A} \approx 0.6\ min^{-1}$ and for paste B it is $n_{crit,\ B} \approx 1.7\ min^{-1}$. The finding $n_{crit,\ A}\ <\ n_{crit,\ B}$ might be due to different vehicle viscosity or due to varying silver particle size. However, both pastes exhibit much higher n_{crit} values for a measuring gap height $h = 0.2\ mm$. Thus, decreasing the gap height allows for a wider shear rate range in which viscosity determination is possible. The reason for the high n_{crit} values found for $h = 0.2\ mm$ is not yet clear. This might be due to a stronger contribution of surface tension at the sample rim or due to the formation of aggregates clogging the narrow gap. Further investigations are necessary to clarify that. Figure 2.10 further confirms that for $\dot{\gamma}_{app} = 0.07\text{-}2.5\ s^{-1}$ the apparent viscosity data obtained at different gap heights do not vary systematically, i.e. wall slip is negligible under these experimental conditions. Varying the shear rate from high to low or from low to high values yields the same viscosity data as long as n_{crit} is not exceeded, i.e. no spillage takes place, i.e. there is no evidence of irreversible structural change within the sample.

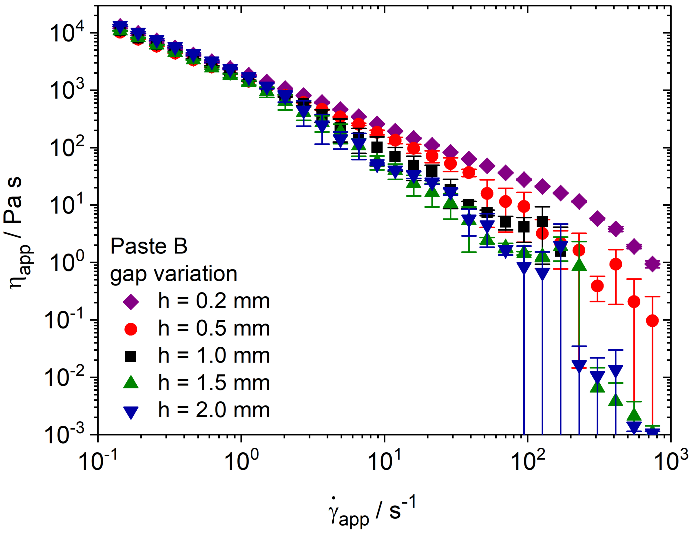

Figure 2.10: **Effect of gap height on sample spill.** Apparent viscosity at varying measuring gap height h in controlled shear rate mode for paste B and plate roughness R_q = 2-4 μm. The gap height is varied between $h = 0.2$ mm and $h = 2.0$ mm. Downward kink of viscosity curve sets in at higher shear rates when a lower gap height is chosen. The gap height is varied between $h = 0.2$ mm and $h = 2.0$ mm. The error bars are calculated as the standard deviation obtained from at least three independent measurements.

A capillary rheometer is used to determine the paste viscosity especially at process-oriented high shear rates. The Weissenberg-Rabinowitsch correction for non-parabolic velocity profile is done here to get the true shear rate in the case of non-Newtonian fluids [97]. The entrance pressure loss is negligible because of the high L/d ratio >> 1, but the occurrence of wall slip has not been investigated in this case and therefore data have to be treated as apparent viscosity values. Figure 2.12 displays the apparent viscosity for both pastes A and B determined with parallel-plate rotational rheometry and capillary rheometry. Remarkably, the data obtained from both experimental techniques seem to agree very well for both pastes suggesting that wall slip is of minor relevance in the capillary rheometry measurements performed here. Finally, paste A and B exhibit similar apparent viscosity at low shear rates but viscosity of paste A is higher than that of paste B in the high shear regime.

Steady shear measurements using parallel-plate rotational rheometers have to be performed carefully and may be disturbed by wall slip, shear banding or sample

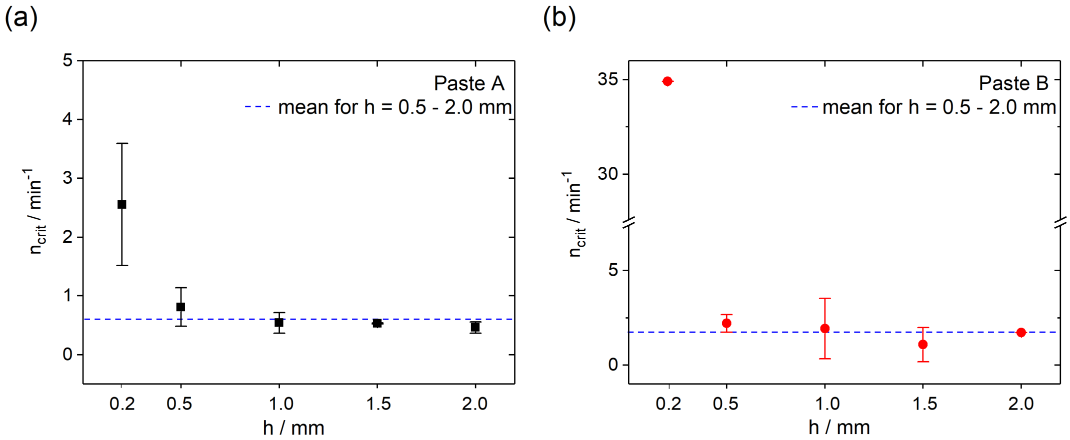

Figure 2.11: **The critical rotational speed at which sample spill sets in.** Rotational speed n_{crit} at which the downward kink of the viscosity curve sets in vs. gap height h using parallel-plate geometry with R_q = 2-4 μm (left: paste A, right: paste B). Sample spillover sets in at this characteristic rotational speed as confirmed by video recordings. For paste A sample spill sets in at $n_{crit,\ A} = 0.6\ min^{-1}$ and for paste B at $n_{crit,\ B} = 1.7\ min^{-1}$ for gap height $h \geq 0.5\ mm$. The error bars are calculated as the standard deviation obtained from at least three independent measurements.

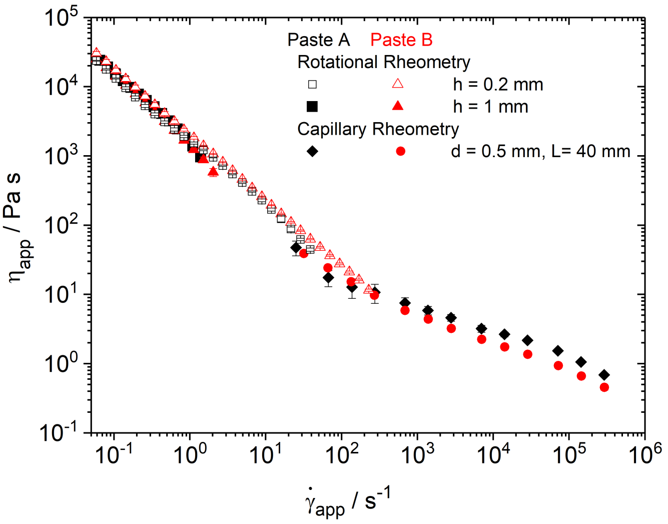

Figure 2.12: **Viscosity in a wide shear rate range.** Apparent viscosity of paste A and B determined in a wide shear rate range using parallel-plate rotational rheometry (gap height h = 0.2 mm and h = 1 mm; R_q = 2-4 μm) and capillary rheometry (d = 0.5 mm and L = 40 mm). The error bars are calculated as the standard deviation obtained from at least three independent measurements.

spillage as extensively discussed above. Therefore, using oscillatory shear experiments have been suggested to characterize structural breakdown and recovery of silver pastes during the screen-printing process. This is done in a three stage oscillatory test as suggested by Hoornstra, Thibert, and Zhou [18, 76, 80]. First, an amplitude sweep has to be performed to determine the linear and non-linear response regime at a pre-selected frequency (Figure 2.13).

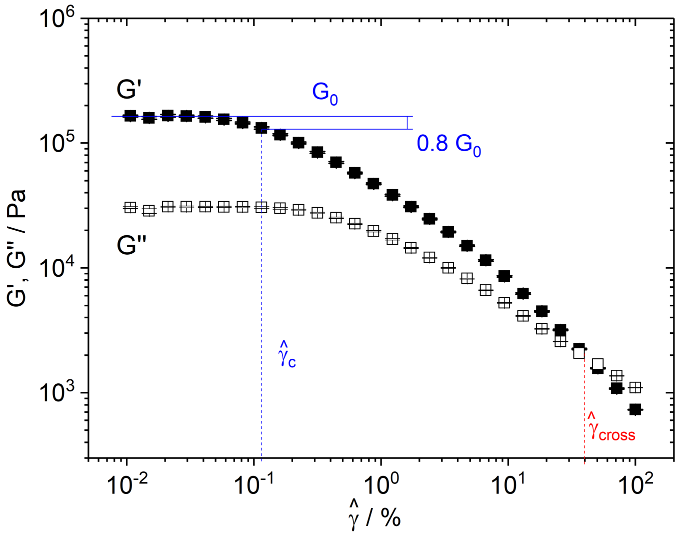

Figure 2.13: **Determination of the linear and non-linear response regime in oscillatory shear.** Amplitude sweep test for paste B: G', G'' vs. deformation amplitude $\hat{\gamma}$ at fixed frequency $f = 1\ Hz$. Test performed using a rotational rheometer equipped with parallel-plate geometry (R_q = 2-4 μm, gap height $h = 1\ mm$). The error bars are calculated as the standard deviation obtained from at least three independent measurements.

The linear viscoelastic regime distinguishes itself by constant, $\hat{\gamma}$-independent modulus values and $G' > G''$. The decay of the storage modulus G' at large $\hat{\gamma}$ is chosen as a criterion to identify the onset of the non-linear response regime. The characteristic deformation amplitude $\hat{\gamma}_c$ marking the transition from linear to non-linear response is defined as the amplitude at which G' has decreased to 80 % of its average initial value G_0 in the linear regime: $G'(\hat{\gamma}_c) = 0.8\ G_0$. In stage I and III of the test, a small oscillation amplitude within the linear viscoelastic response regime, i.e. $\hat{\gamma} < \hat{\gamma}_c$ is selected to characterize the rest structure of the paste (stage I) as well as the time dependence and degree of recovery in stage III of the test after the destruction of the initial structure due to a high deformation amplitude applied in stage II. Figure 2.14 shows corresponding results for paste B.

In stage I, the paste is deformed at $\hat{\gamma} = 0.025$ % and G' is higher than G'', i.e. the elastic behavior of the paste is predominant. When deformation is increased in stage II, G'' is higher than G' ensuring the structural breakdown within the paste during this period of large deformation. Stage III simulates the resting of the finger lines on the substrate after printing. In this stage G' is higher than G'' again, but

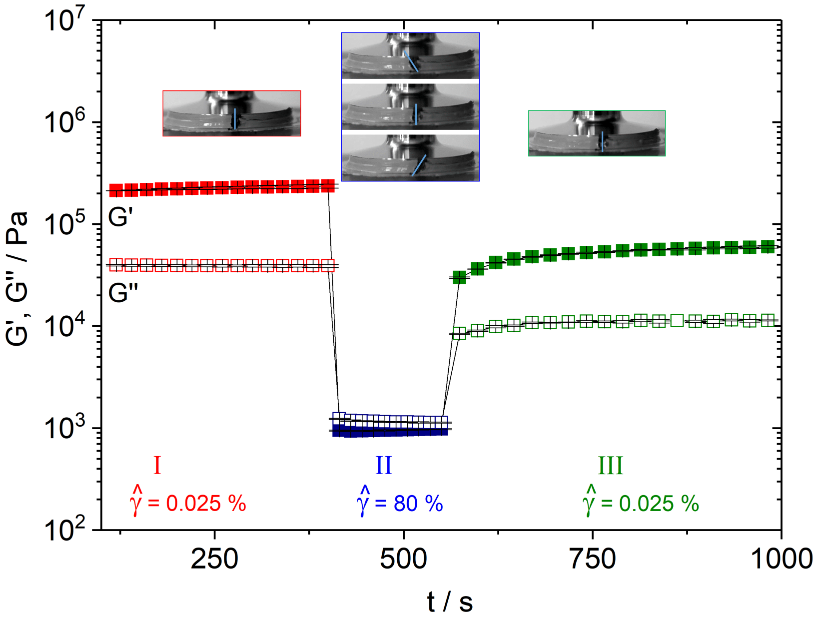

Figure 2.14: **Three stage structural recovery test.** Three stage structural recovery test for paste B performed at constant frequency $f = 1\ Hz$ with a parallel-plate rotational rheometer (plate roughness R_q = 2-4 μm). The applied deformation amplitude $\hat{\gamma}$ in stage I is 0.025 %, in stage II $\hat{\gamma}$ = 80 %, and in stage III $\hat{\gamma}$ = 0.025 %. Video recordings confirm homogeneous sample deformation throughout the gap, no wall slip, shear banding, plug flow or sample spillage occurs. The error bars are calculated as the standard deviation obtained from at least three independent measurements.

G' and also G'' are both lower than the respective initial G' and G'' values before the paste structure was destroyed. The video recordings confirm that this is not related to the effects like wall slip, plug flow or sample spill. The paste deforms uniformly during oscillatory shear, sticks to the plate, and indicates neither wall slip nor sample spill. Therefore, it can be concluded that the incomplete recovery of the shear moduli indicates an irreversible structural change within the sample due to the applied large amplitude shear in stage II. The data shown in Figure 2.15(a) reveal that the degree of irreversible structural change does not depend on the duration of the large deformation amplitude oscillatory shear applied in stage II. The results in stage III do not vary for different periods of shearing time t_{II}. However, the value of the selected deformation amplitude in stage II has a strong impact on the degree of structural recovery. This is obvious from Figure 2.15(b) showing the difference between the storage modulus values determined in stage III and I $\Delta G'$ normalized by the initial modulus value G'_I. For $\hat{\gamma} > 20$ %, i.e. at deformations corresponding to the crossover of G' and G'' (see Figure 2.13) paste B recovers only 30 % of its initial value and paste A only 10 %. This is considered a paste property crucial for various coating operations and its dependence on paste composition will be addressed in future work. Note, the structural recovery immediately after cessation of large amplitude oscillatory shear in stage II would be of utmost relevance especially for the screen-printing process but the commercial rheometer used here does not allow for determination of reliable data within the first second after changing $\hat{\gamma}$.

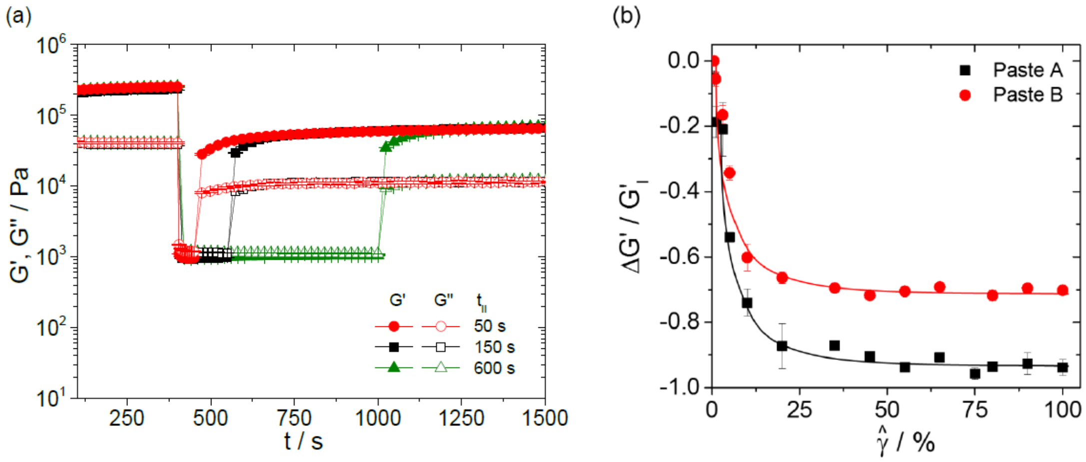

Figure 2.15: **Structural recovery tests.** (a) Effect of shearing time on structural recovery. Structural recovery of paste B for $\hat{\gamma}_{II} = 80$ % and different duration of stage II, $t_{II} = 50\ s$, 150 s and 600 s. (b) Effect of deformation amplitude on structural recovery. Relative irreversible structural change $(G'(t \to \infty) - G'(t = 0)) / G'(t = 0) = \Delta G' / G'_I$ as a function of deformation amplitude $\hat{\gamma}$ applied in stage II of the three stage structural recovery test determined for paste A and B at constant $t_{II} = 150\ s$. The error bars are calculated as the standard deviation obtained from at least three independent measurements.

Filament stretching experiments have been performed to simulate the snap-off during screen-printing. The snap-off belongs to the final step of screen-printing. Figure 2.16 demonstrates that the filament lengths at break increases with increasing stretching velocity for both pastes. Breakage always occurs at lower stretch ratio $(h_{br} - h_0) / h_0 = \Delta h_{br} / h_0$ for paste B than for paste A, but this difference seems to decrease slightly with increasing stretching velocity. Since the filament breakage of paste B happens at a lower stretch ratio this paste may have better snap-off properties.

The results obtained with the capillary breakup elongational rheometer imaging setup are confirmed by the tensile tester experiments. Corresponding results are shown in Figure 2.17. Again the stretch ratio at which the filaments break increase with increasing stretching velocity (Figure 2.17(a)) and paste B breaks at lower Δh_{br} / h_0 values than paste A.

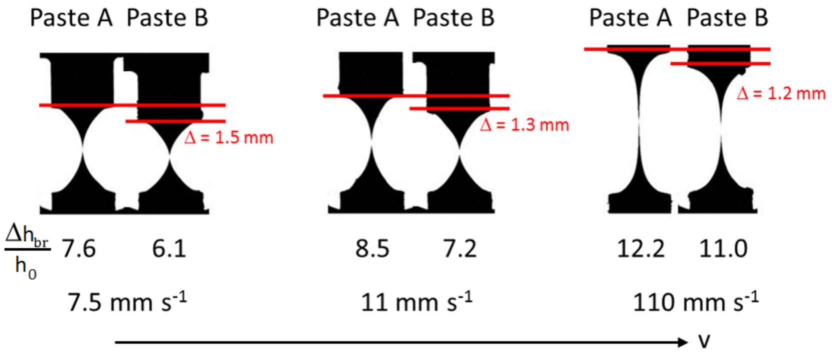

Figure 2.16: **Optical determination of filament breakage in elongational deformation.** Critical tensile stretch ratio at which filament breakage occurs for pastes A and B at different stretching velocities as obtained using the capillary breakup elongational rheometer (initial gap height $h_0 = 1\ mm$).

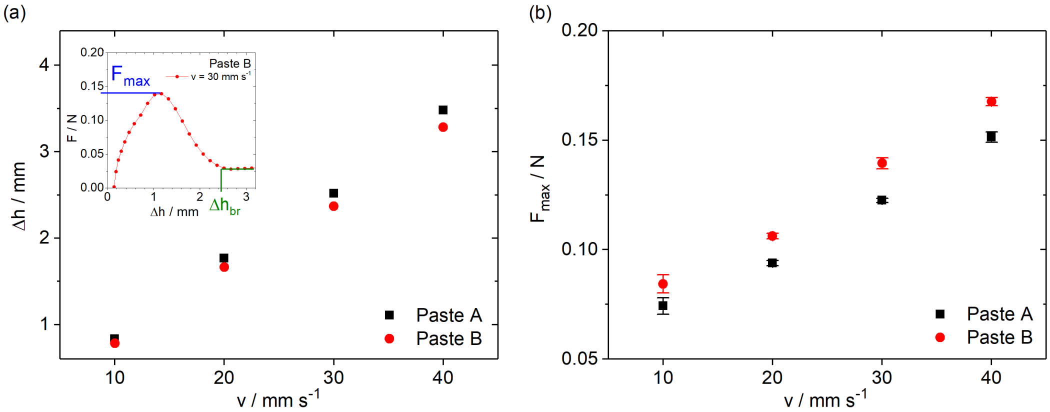

Figure 2.17: **Tensile testing - axial force during elongational deformation.** Resulting Δh_{br} / h_0 (a) and resulting force F_{max} (b) vs. stretching velocity obtained for paste A and B with the tensile tester. The initial gap height is $h = 1\ mm$ and the piston diameter $d = 5\ mm$. The insert displays raw force F vs. stretch ratio data for paste B obtained at $v = 30\ mm\ s^{-1}$ to demonstrate the determination of F_{max} and Δh_{br}. The error bars are calculated as the standard deviation obtained from at least three independent measurements.

However, the absolute values Δh_{br} / h_0 obtained with the capillary breakup elongational rheometer are always higher than corresponding values obtained with the tensile tester. This is attributed to the different plate diameters $d = 6\ mm$ and $d = 5\ mm$, i.e. different initial sample volumes for the capillary breakup elongational rheometer and tensile tester. Finally the tensile tester also provides a second characteristic parameter the maximum force F_{max} acting on the filament during stretching. This quantity also increases linearly with increasing separation speed but in this case the values obtained for paste B are larger than those for paste A. Further investigations will be needed to disclose the relevance of F_{max} for the screen-printing process or other coating operations.

2.4 Discussion

A comprehensive rheological characterization of highly concentrated suspensions or pastes is mandatory for a targeted product development meeting the manifold requirements during processing and application of such complex fluids. This investigation includes the determination of yield stress, viscosity, wall slip velocity, structural recovery after large deformation and elongation at break as well as tensile force during filament stretching. A summary of all applied methods, obtained information, and paste characteristics are summarized in Table 2.1.

methods	**information**	**paste characteristics**	**plate roughness R_q**
steady shear	apparent viscosity η_{app}	A > B	2-4 μm
	yield stress τ_y	A > B	2-4 μm; vane geometry
	wall slip behavior v_{slip}, V^*	A > B	1.15 μm
	crit. rotational speed n_{crit}	A > B	2-4 μm
oscillatory shear	elastic modulus G_0	A > B	2-4 μm
	structural recovery	A < B	2-4 μm
stretching behavior determination	elongation at filament breakage	A > B	-
	maximal tensile force during elongation	A < B	-

Table 2.1: **Overview of applied methods, corresponding characteristic information and differences between specific flow properties of paste A and B.**

The importance of video recordings for reliable determination of rheological quantities of highly filled suspensions showing wall slip, shear banding and sample spillover in parallel-plate rotational rheometry is demonstrated. Video recordings enable the determination of the true deformation profile and the flow field at the sample rim using appropriate markers. It is necessary to study this deformation behavior before analyzing the results of rheological experiments. Thus measurement parameter settings and plate roughness values can be identified for which viscosity measurements are possible. The paste yield stress can be determined either using a vane geometry or plate-plate geometry with appropriate roughness.

Viscosity determination is possible using plate-plate geometry only with a carefully selected plate roughness depending on sample composition. Higher roughness does not necessarily result in lower wall slip. The shear rate or shear stress range in which viscosity determination can be done is limited by the yield stress and the onset of sample spill.

Furthermore, the slip velocity can be measured directly and measuring conditions at which plug flow, shear banding or sample spillover occur can be identified clearly. For wall slip measurements smooth surfaces were used as the upper shearing plate and a rough bottom plate to allow slip only at the upper plate. This slip velocity can be calculated directly from the angular velocity of the upper plate. For both pastes slip occurs at stress levels well below the apparent yield stress. Similar observations have been reported for suspensions of glass beads [84], clay suspensions [86], soft microgel pastes as well as for emulsions [87, 88, 89]. Here a linear increase of v_{slip} with τ_{app} is found. This is in line with the observations of Aral et al. [84] who also determined v_{slip} using visualization of the flow field at the rim of the investigated glass bead suspensions.

Seth et al. have shown that the scaling of slip velocity with applied stress is controlled by the interaction between the soft particles they used in their study and the wall. For the case where there is no specific adherence of particles to the wall, they also find a linear relationship between v_{slip} and stress but a quadratic scaling is found for the particles weakly adhering to the wall [87, 88, 89]. The studies on soft particle pastes also reveal a characteristic slip velocity V^* at the yield stress and a elastohydrodynamic model is presented [88] allowing to calculate V^* from physical fluid and particle parameters which can be determined independently: $V^* \sim {\gamma_y}^2\ (G_0\ R\ /\ \eta_s)\ (G_P\ /\ G_0)^{1/3}$. This characteristic slip velocity depends on the pastes yield strain γ_y and elastic modulus G_0, solvent viscosity η_s, as well as particle radius R and modulus G_P. The values resulting from this simple estimate ($V_A^* = 375\ \mu m\ s^{-1}$ and $V_B^* = 118\ \mu m\ s^{-1}$) agree very well with the experimental results (Figure 2.9) not only with respect to the order of magnitude but also regarding the difference between paste A and B.

Sample spillage is observed here at a critical rotational speed characteristic for each paste. Spillage does not occur in the pure vehicles. This phenomenon limits rheological characterization of the pastes and may also be relevant for certain processing or coating operations but its physical origin still remains unsolved.

Video recordings further indicate that wall slip, plug flow and sample spill can be excluded during oscillatory shear tests. Therefore, the decrease and increase in shear moduli observed during three stage oscillatory shear tests with small oscillation amplitude in stage I and III as well as large deformation amplitude $\hat{\gamma} > \hat{\gamma}_c$ can be directly attributed to structural break down and recovery. It could be shown that the degree of irreversible structural change during oscillatory shear increases with increasing deformation amplitude in stage II until a saturation is reached at deformations corresponding to the crossover of G' and G'' in the amplitude sweep test, but the irreversible damage is independent of the duration of high amplitude shear in stage II. The change in modulus and hence sample structure due to large shear deformation in stage II is termed irreversible here since after waiting times of more than 10^4 s, the storage modulus is far lower than its initial value (data not shown). The data shown in Figure 2.15 are restricted to waiting times of 1500 s for the sake of clearness. However, it should be noted that the time scale of the printing process is on the order of seconds or even below. This is not accessible with the conventional rotational rheometer setup used in this study.

The gap heights used in this study are also much larger than typical mesh openings in screen-printing of modern printed electronics. Rheological measurements using plate-plate geometry cannot be done at such small gap openings due to limitations of mechanical adjustment for large plates typically used in rheological measurements. Furthermore, large gap separations have been chosen here to ease visualization of the sample deformation at the rim.

Filament stretching tests using a capillary breakup elongational rheometer and a tensile tester can be used to characterize the deformation and breakup behavior of highly filled pastes in elongational flows. The elongation at the break and the maximum force during elongation are parameters obtained from these tests and may be related to the squeegee snap-off during screen-printing.

Finally, significant differences were observed in all the experiments described above for the two commercial silver pastes investigated in this study. An extended discussion of the relevance of the rheological paste properties for their performance will be addressed in a subsequent paper based on data for a broad variety of different pastes and vehicles.

Disclosures

The authors have nothing to disclose.

Acknowledgements

The authors would like to thank to Heraeus Precious Metals GmbH & Co. KG for their support and supply of commercial silver pastes, especially M. König for fruitful discussions. Special thanks go to M. Schmalz for experimental support. C. Yüce gratefully acknowledges financial support by the 100 prozent erneuerbar stiftung. Finally, we acknowledge financial support from the Federal Ministry for Economic Affairs and Energy (Grant no. 0325775G).

3. Rheology and screen-printing performance of silver pastes

Full title:	Rheology and screen-printing performance of model silver pastes for metallization of Si solar cells [100]
Authors:	Ceren Yüce, Markus König, and Norbert Willenbacher
Status:	published
Bibliographic data:	Coatings, 2018, 8, 406; doi:10.3390/coatings8110406

Abstract

Further strong growth of solar energy conversion based on PV (photovoltaic) technology requires constant improvement to increase solar cell efficiency. The challenge in front-side metallization of Si solar cells is to print uniform fine lines with a high aspect ratio to achieve higher efficiencies simultaneously with a reduced consumption of raw materials. An in-depth understanding of the relationship between paste composition, rheology and screen-printed line morphology is essential. Three model pastes with similar silver content and corresponding vehicles differing in their thixotropic agent content were investigated. Rheological properties (yield stress, viscosity, wall slip velocity, structural recovery, and fracture strain) were determined using steady and oscillatory shear, as well as elongational flow rheometry. Pastes were screen-printed at various speeds through a layout screen including line widths between 20 and 55 μm. Dried fingers were analyzed with respect to line width, aspect ratio (AR) and cross-sectional area. Our investigations reveal that minor changes of thixotropic agent result in substantial variations of the paste's flow properties. However, this only weakly affects the line morphology. Irrespective of printing speed or finger opening, AR is slightly increasing; i.e., the screen-printing process is robust against changes in paste rheology.

Keywords

silver pastes; fine line screen-printing; rheology; electrode line morphology

3.1 Introduction

Screen-printing is a traditional and versatile printing method [4, 5]. It is well established, not only in textile or poster printing, but also in the fabrication of all kinds of electronic devices, such as printed circuit boards [7, 8], thin film transistors [9], displays, touch panels [10], low temperature co-fired ceramic devices [11, 12], and photovoltaic cells [13, 14]. Screen-printing is easy to implement and allows for high through-put, and is thus economically attractive for high-volume products like silicon (Si) solar cells. Today, essentially all commercial Si solar cells are metallized via screen-printing [59] and this technology was one of the key factors enabling recent improvements in efficiency. A further substantial increase of solar energy conversion is required to meet increasing global electric power demand, as well as the challenges of climate change. However, about 7.5 % of global silver production is currently employed in the metallization of solar cells [6]. A constant, significant reduction of silver consumption per wafer is necessary for a further expansion of PV installation. This drives perpetual efforts to decrease the width and increase the aspect ratio and uniformity of the finger lines making up the front contacts of Si solar cells, aiming at higher cell efficiency and lower silver consumption [101]. Besides an optimized wafer surface treatment, adapted printing parameters and an appropriate screen design, this requires a carefully adjusted silver paste formulation. Two key features, namely, the wetting and the flow properties of the paste, are decisive to achieve high-performance printed fingers. From flooding of the screen to snap-off of the screen from the wafer and drying of the printed features, the paste is exposed to complex loads, including a broad range of shear rates and stresses. In addition, resistance to elongational deformation during snap-off, structural recovery after being squeezed through the screen openings, and slip at the boundaries of these openings, also have to be considered [18, 19, 20, 21, 22, 23, 24, 25, 26, 27]. Rheological characterization of up-to-date commercial silver pastes for front-side metallization is a particular challenge. Rheological measurements are limited by wall slip and shear banding phenomena, and sample spill is strongly dependent on the employed experimental setup, and particularly on the surface energy and roughness of the sample fixtures, and the details of the experimental protocol. Recently, we have presented detailed experimental protocols allowing for a meaningful, comprehensive characterization of paste flow properties addressing all of the aspects mentioned above [95]. Silver pastes for solar cell metallization consist of silver particles, which finally provide the conductivity of the printed and sintered structures, as well as glass frits opening the passivation layer during sintering [57]. The particles are usually suspended in a mixture of organic solvents and so-called thixotropic agents, with binders added as polymeric, non-volatile organic ingredients to control the flow behavior of the paste and to provide the appropriate cohesive and adhesive properties of the dry layer [24, 54, 55, 56]. Hydrogenated castor oils and diamines are often used as thixotropic agents, whereas synthetic acrylate polymers or ethyl cellulose are frequently added as binders.

The flow properties of screen-printing silver pastes and concepts relating to the control of yield stress and shear thinning behavior via the above-mentioned polymeric additives have been discussed in various studies [55, 56, 74, 91]. It is generally accepted that screen-printing pastes should exhibit a substantial degree of shear thinning [18, 24].

A rheological characterization of a commercial silver paste for front-side metallization of solar cells was provided by [18]. However, a direct comparison to printed electrode properties was not made. In [25], four commercial silver pastes characterized as suggested in [18] were used to develop screen design strategies for an optimized front-side metallization of solar cells. A thick emulsion over mesh (EOM) layer enabled printing of fingers with a high aspect ratio, whereas a thin EOM layer limited paste spreading. Differences in wetting properties among the pastes were not addressed in this study. Recently, the effect of paste rheology during the screen-printing process was directly investigated in a combined rheological and high-speed video imaging study [91]. Screen-printing ZnO pastes, including different types and concentrations of thixotropic agent and binder, on a glass substrate confirmed that the length of the pre-injection zone is inversely proportional to the yield stress, whereas the length of the cling zone was linearly related to the filament rupture strain. The printed electrode width turned out to be inversely proportional to the product of the yield stress and high shear viscosity. In this study, the spreading process was limited to a period of 100 ms after the squeegee had passed.

Two recent studies revealed that wall slip of silver pastes can have a significant impact on paste transfer and line shape [26, 27]. A higher slip velocity resulted in a higher silver laydown and a higher aspect ratio of the printed lines, as well as in a narrower intersection of busbar and fingers. The gain of scientific insight in such studies trying to correlate paste rheology and printing performance is limited when pastes with different compositions, not only with respect to rheology but also in terms of their substrate wetting properties, are investigated [25, 27].

Therefore, we choose a model system comprising silver particles, a mixture of organic solvent, and a thixotropic agent, as well as ethyl cellulose as binder. The silver content and the total amount of non-volatile organic additives were kept constant. The mixing ratio of thixotropic agent and binder, however, was varied in a certain, narrow range. This resulted in a substantial change of several rheological parameters, including yield stress, shear modulus, low shear viscosity, structural recovery and elongational fracture strain, without affecting the wetting behavior. Pastes were printed using a standard commercial lab-scale screen printer. A layout screen with finger opening width varying between 20 and 55 μm was used and different printing speeds (70 - 210 $mm\ s^{-1}$) close to technical conditions were employed. The resulting finger lines were analyzed with respect to cross-sectional area, line width and height, as well as fluctuations of these quantities along the printed structures, allowing for a direct correlation to the above-mentioned rheological parameters.

3.2 Materials

Three model silver pastes (M1-M3) based on three corresponding vehicle formulations (V1-V3) were characterized in this study. All vehicles were made from the same organic solvent (a mixture of four parts diethylenglycoldibutylether and one part terpineol), thixotropic agent (Thixatrol Max), and organic binder (ethyl cellulose). They differed in their concentration ratio of Thixatrol Max (T-Max) and ethyl cellulose (EC) binder as shown in Table 3.1. Since these polymeric additives are not surface active [102] and their amount was varied only in a small range, we can safely assume that the surface tension and wetting behavior were similar for all investigated model systems. The changes in vehicle composition were in a range typical for commercial silver pastes.

Diethylenglycoldibutylether and terpineol were mixed and EC binder was dissolved using a tempered dissolver (DISPERMAT LC, VMA-Getzmann GmbH, Reichshof, Germany) at 60 ± 10 °C until the solution became clear. After, T-Max was dissolved using the same equipment at 70 ± 10 °C.

Spherical silver particles with a mean diameter $x_{50} = 1.5\ \mu m$, according to Fraunhofer diffraction, were dispersed in these vehicles at a concentration of 80 $wt\%$ to formulate printable silver pastes. A three-roll mill (EXAKT 80E, EXAKT Advanced Technologies GmbH, Norderstedt, Germany) and a non-contact planetary mixer (SpeedMixer^{TM}, Hauschild GmbH, Hamm, Germany) were used to manufacture homogeneous pastes free of agglomerates as confirmed by the low fineness of grind value (FOG) ≈ 8 ± 2 μm. All vehicles and silver pastes were prepared by Heraeus Deutschland GmbH & Co. KG in Hanau, Germany as described above.

Table 3.1: Overview of investigated model vehicles (V1, V2, and V3) and model silver pastes (M1, M2, and M3). Vehicles included thixotropic agent and ethyl cellulose binder at varying mixing ratios. Model silver pastes additionally contained 80 $wt\%$ (corresponding to 36.4 $vol\%$) spherical silver particles ($x_{50} = 1.5\ \mu m$).

sample	**silver particles** / $wt\%$	**thixotropic agent** / $wt\%$	**ethyl eellulose binder** / $wt\%$	**organic solvent** / $wt\%$
V1	0	11.73	5.61	82.65
V2	0	11.80	5.05	83.14
V3	0	13.49	5.50	81.00
M1	80	2.35	1.12	16.53
M2	80	2.36	1.01	16.63
M3	80	2.70	1.10	16.20

3.3 Experimental methods

A series of rheological and screen-printing experiments were performed to correlate flow properties and screen-printing results of model vehicles (V1, V2, and V3) and model pastes (M1, M2, and M3). Experimental investigations were separated into two parts. The first consisted of the rheological investigations performed at the Institute for Mechanical Engineering and Mechanics at KIT (Karlsruhe Institute of Technology) in Karlsruhe, Germany. A thorough rheological characterization was performed, including steady and oscillatory rotational shear rheometry, capillary viscometry and filament stretching elongational rheometry, as described in [95]. Secondary flow effects, such as wall slip, shear banding and sample spillage, were carefully considered. The second part included printing tests of model pastes. We conducted screen-printing experiments with a half-automatic gadget at the laboratories of Heraeus Deutschland GmbH & Co. KG in Hanau, Germany. All experiments were conducted at 23 °C.

3.3.1 Rheological measurements

Yield stress measurements were performed using a stress-controlled rheometer setup (Haake RS150, Thermo Fisher Scientific, Karlsruhe, Germany) equipped with a vane-and-cup fixture. We performed the measurements in a stepwise controlled stress mode. The shear stress was varied from 1 to 5000 Pa, in 41 steps, equally separated on a logarithmic scale, and each stress was applied for 30 s. Yield stress values were determined from the measured deformation using the tangent intersection point method [95, 103, 104].

A rotational rheometer with parallel-plate measuring system (Physica MCR501, Anton Paar Germany GmbH, Ostfildern, Germany) and a customized capillary rheometer (Göttfert Rheograph 2000, Göttfert Werkstoff-Prüfmaschinen GmbH, Buchen, Germany) were used for viscosity measurements to cover paste behavior at low and high shear rates. Choosing a plate roughness of R_q = 2-4 μm avoided wall slip effects and/or plug flow in the measuring gap by video imaging of the gap edge described in [95]. The measuring gap height was $h = 1\ mm$ and the plate diameter, $d_{plate} = 25\ mm$. Rotational rheometer measurements were taken using a stepwise controlled rate adjustment. The shear rate was varied from 0.01 to 1000 s^{-1} in 41 steps, equally separated on a logarithmic scale, and each shear rate was applied for 30 s. Capillary rheometry was undertaken using a capillary nozzle with diameter, $d_{nozzle} = 0.5\ mm$, and length, $L_{nozzle} = 40\ mm$. The paste was filled into a feed reservoir with diameter, $D_{reservoir} = 20\ mm$, and pushed through the nozzle at the center of the reservoir bottom at velocities between 0.05 and 20 $mm\ s^{-1}$, corresponding to shear rates between 720 and $3 \cdot 10^5\ s^{-1}$. The corresponding pressure drop was recorded using a 500 bar pressure transducer (Gefran Deutschland GmbH, Seligenstadt, Germany). Sample viscosity was calculated from this pressure drop and the corresponding flow rate. The Rabinowitsch-Weissenberg correction was performed to obtain true shear rates taking into account deviations from the parabolic flow profile in the nozzle [97].

Wall slip velocity was determined in a parallel-plate rheometer (Haake RS150). The measuring gap height was $h = 1\ mm$ and plate radius $r = 10\ mm$. A smooth upper plate ($R_q = 1\ \mu m$) and a rough bottom plate ($R_q = 9\ \mu m$) were used to assure that slip takes place at the upper plate and that the rest of the sample remained undeformed [26]. The slip velocity could then be calculated as $v_{slip} = 2\pi n r$, where n is the rotational speed of the upper plate. Experiments were done at shear stresses between $\tau = 200\ Pa$ and the yield stress τ_y of the respective paste.

Sample spillage is known to limit the shear rate range for flow curve measurements. Spillage shows up as a downward kink in apparent viscosity versus shear rate data, and the critical rotational speed for the onset of spillage was determined at various plate separations between 0.2 and 2 mm for plates with different roughness $1\ \mu m < R_q < 9\ \mu m$.

Oscillatory shear experiments were conducted using a rotational rheometer (Physica MCR501) with a parallel-plate measuring system ($d_{plate} = 25\ mm$, R_q = 2-4 μm, $h = 1\ mm$). Measurements with varying strain amplitude ($\hat{\gamma}$ = 0.001-100 %, in 35 steps, equally separated on a logarithmic scale) at constant frequency $f = 1\ Hz$ allowed for determination of the plateau modulus G_0, defined as the value of the storage modulus G' in the linear viscoelastic regime (LVE) where G' and G'' were independent of the strain amplitude, as well as for determination of the crossover-stress $\hat{\tau}_c$ at which $G' = G''$, with the loss modulus G''. The frequency dependence of G' and G'' was examined at constant amplitude $\hat{\gamma} = 25$ % covering the frequency range f = 100-0.001 Hz in a downward mode.

Information about structural recovery of model vehicles and silver pastes was obtained from oscillatory time interval tests as described in [18, 95]. The measurement protocol comprised three sections with different deformation, but constant frequency $f = 1$ Hz, to mimic the paste deformation during the screen-printing process. The deformation applied in sections I and III was $\hat{\gamma} = 0.05$ %, i.e., in the LVE regime, to represent the behavior during pre-print and at rest, after the paste was pushed through the finger opening. Measuring times were selected as 400 s for the first step and 20 min for the third recovery step. In section II we applied the deformation $\hat{\gamma} = 90$ % to simulate the paste transfer through the finger opening. This measurement period lasted for 150 s.

A capillary breakup elongational rheometer (CaBER) (HAAKE CaBER1, Thermo Fisher Scientific, Karlsruhe, Germany) was used to perform filament stretching experiments. Therefore, the measuring gap (height $h_0 = 1$ mm) between two pistons (diameter $d_{piston} = 6$ mm) was filled with the sample, and the upper piston was moved from $h_0 = 1$ mm to the end position $h_{end} = 16$ mm, at constant stretching velocity $v_{stretch} = 110$ mm s^{-1}. A high-speed camera (Photron FastCam-X1024 PCI, Photon, Pfullingen, Germany) was used to record the change in filament shape at 250 fps during stretching. The filament breakage length h_{break} and the fracture strain $\epsilon = (h_{break}$ - $h_0)/h_0$ were determined from corresponding video image sequences.

3.3.2 Screen-printing tests and morphology observation of printed electrodes

Screen-printing tests were performed with a half-automatic EKRA X1-SL screen printer (EKRA Screen Printing Technologies, ASYS Group, Dornstadt, Germany). A stainless-steel screen mesh (360 meshes per inch with a layout of about 50 μm down to 20 μm finger opening, 16 μm thread diameter and 13 μm emulsion over mesh (EOM) layer thickness) was used to perform printing tests. An RKS squeegee (200 mm length) (RK Siebdrucktechnik GmbH, Rösrath, Germany) with a 65 shore hardness and forming a 60° angle with the screen was used for printing. The printing speed was varied between 70 and 210 mm s^{-1}. Snap-off distance between the screen mesh and the substrate was fixed at $h_{snap-off} = 1.5$ mm. The monocrystalline (Cz) Si-wafers were weighed before and after the printing process to determine the paste laydown on the substrate. In the final step, printed substrates were dried in a drying chamber at 150 °C for about 10 min.

The morphology of dried finger profiles obtained from 25, 30, and 50 μm finger line openings were examined with a 3D laser scanning microscopy (VK-X100 Laser Microscope, Keyence Deutschland GmbH, Neu-Isenburg, Germany). Therefore, we selected finger lines located at the same position on five different Si-wafers for each paste and each finger line opening to assure that these fingers were printed through the same screen area. Self-programmed MATLAB-code (MATLAB R2017a) was used to characterize the finger width w_f and finger height h_f. The cross-sectional area A_f of printed finger lines was calculated by integration of the finger profile perpendicular to the printing direction. The aspect ratio AR was given by $AR = h_f{\cdot}w_f^{-1}$. The average and standard deviation values for these quantities were calculated from the respective data obtained for the five different wafers.

3.4 Results and discussion

3.4.1 Rheological properties of model vehicles and model silver pastes

All samples investigated in this work exhibit a yield stress τ_y which is the minimum stress required to force the sample to flow due to stress-induced structural rearrangements or breakdown of the sample's network structure. Yield stress data for model vehicles and silver pastes are shown in Figure 3.1.

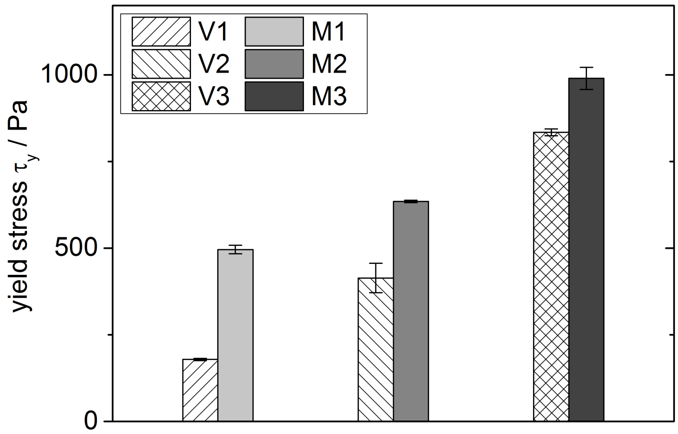

Figure 3.1: Yield stress values of vehicles and silver pastes determined from rotational rheometry (vane-and-cup fixture). Patterned bars represent the model vehicles (V1-V3) and filled bars the model pastes (M1-M3) containing 80 $wt\%$ silver particles.

The yield stress increases from V1 to V3, and, respectively, from M1 to M3. The yield stress of the vehicles and the silver pastes is mainly controlled by the strong sample spanning structure formed by T-Max during organic medium preparation, which prevents phase separation and ensures long storage periods [24, 54]. In the silver pastes, van der Waals (vdW) interactions among particles and depletion attraction triggered by free (nonadsorbing) ethyl cellulose may additionally contribute to reinforce the network structure [54, 105]. In our model vehicle series, the slight increase in T-Max from 11.73 $wt\%$ to 13.49 $wt\%$ resulted in a four-fold increase in τ_y from 180 to 830 Pa. For the silver pastes, however, the same relative rise in T-Max only led to a doubling of the yield stress from 495 to 990 Pa. The vehicle without T-Max does not exhibit yield stress at all. The paste without T-Max has a very small, hardly measurable yield stress ($\sim 10\ Pa$) and exhibits rapid phase separation (data not shown). The yield stress of the pastes including T-Max therefore cannot be assumed to be a simple superposition of a T-Max network structure and a particle network, but has to be rationalized as the result of a reinforcement of the T-Max structure by the particles. The ratio of paste and vehicle yield stress decreases with increasing T-Max content, indicating that the structure formed by the thixotropic agent is partly destroyed by the silver particles or that the silver particles cannot reinforce the denser structure at higher levels of T-Max content completely.

Yield stress is considered to be one of the key parameters controlling screen-printing behavior. However, viscosity at low and high shear rates may also affect the paste behavior during the printing process. A low high shear viscosity is reported to ease paste transfer through the screen and subsequent release from the screen [21, 24], and a high low shear viscosity is reported to ensure finger line stability [27]. A certain degree of shear thinning is furthermore required to push the paste through the screen opening during squeegee movement [24, 54].

Viscosity curves of all samples investigated here clearly exhibit shear thinning behavior (data not shown). Results obtained at the low shear rate $\dot{\gamma} = 0.5\ s^{-1}$ are shown in Figure 3.2(a). Figure 3.2(b) displays corresponding data obtained at $\dot{\gamma} = 3{\cdot}10^5\ s^{-1}$.

As for yield stress, we observe a strong increase in low shear viscosity due to the slightly increased T-Max content. For the vehicle, this increase is five-fold whereas the low shear viscosity of the silver pastes only doubles. This again indicates that the structure formed by the thixotropic agent is partly destroyed by the silver particles.

The viscosity values at $\dot{\gamma} = 3{\cdot}10^5\ s^{-1}$ are about four orders of magnitude smaller than the corresponding values at $\dot{\gamma} = 0.5\ s^{-1}$. This is true for the vehicles as well as for the pastes and demonstrates the high degree of shear thinning of these systems. This strong viscosity drop is due to the breakdown of the T-Max structure and the high shear viscosity of the vehicles is determined by the solvent mixture, as well as the dissolved EC binder. Since the binder concentration hardly varies among the investigated samples and the solvent mixture is the same in all cases, the high shear viscosity is essentially the same for all three vehicles, as well as for the pastes. The paste viscosity is about twice as high as the vehicle viscosity. For a

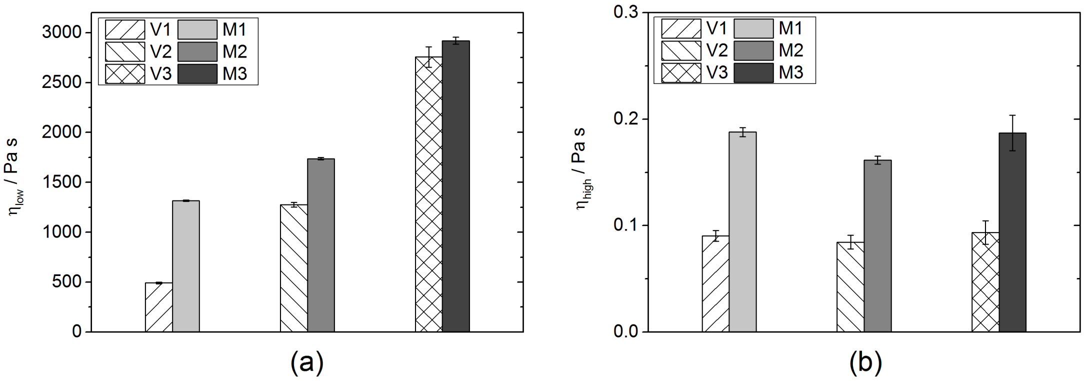

Figure 3.2: (a) Low shear viscosity values determined from rotational rheometry (parallel-plate geometry, $d_{plate} = 25\ mm$, $R_q = 2\text{-}4\ \mu m$, $h = 1\ mm$) at $\dot{\gamma} = 0.5\ s^{-1}$; (b) High shear viscosity results determined using a capillary rheometer ($L_{nozzle} = 40\ mm$, $d_{nozzle} = 0.5\ mm$) at $\dot{\gamma} = 3{\cdot}10^5\ s^{-1}$. Patterned bars correspond to vehicles, filled bars represent silver pastes.

suspension with 36.4 $vol\%$ particle loading, as investigated here, a relative viscosity $\eta_r = \eta_{paste}/\eta_{vehicle} \approx 6$ would be expected [106]. This discrepancy shows that the thixotropic agent T-Max is partly de-activated upon addition of silver particles as already indicated by the lower change of τ_y and η_{low} upon T-Max variation when comparing pastes and corresponding vehicles.

The rheological characterization of highly loaded silver pastes in a parallel-plate rotational rheometer is limited regarding higher shear rates due to sample spillage [56, 95]. We investigate this gap drainage phenomenon for different values of plate roughness R_q between 1 and 9 μm. Sample spillage occurs at a certain rotational speed n_{crit} which increases with decreasing plate roughness and sample yield stress (see Figure 3.13 in Appendix A). Spillage is a phenomenon occurring in silver pastes with a high-density difference between disperse and continuous phases, but does not occur in pure vehicles. Therefore, we assume that it is an inertia-driven phenomenon and a minimum energy input $(\tau{\cdot}\dot{\gamma})$ is required to drain the gap. This energy transfer is higher for samples with higher τ_y and when rough plates prevent slip, i.e., the sample is exposed to higher shear rates.

Previous work revealed that wall slip promotes paste transfer and leads to improved finger line/busbar connections [26]. Wall slip effects often disturb the rheological characterization of highly filled pastes or suspensions, and viscosity data may be blurred if slip is not taken into account adequately. No indication for wall slip was found for the vehicles investigated here. The pastes' slip velocity v_{slip} is displayed as a function of shear stress τ (Figure 3.3). Slip velocity increases linearly with increasing shear stress. The applied stress was varied between $\tau = 200\ Pa$ and τ_y of the respective paste. For a given τ the wall slip velocity decreases with increasing T-Max content. The characteristic slip velocity V^* [87] is obtained at the yield stress τ_y of the respective paste, but is independent of sample composition. It should be kept in mind that the slip velocities found here are more than an order of magnitude lower than those reported earlier [26], i.e., wall slip is of minor relevance for the pastes investigated here.

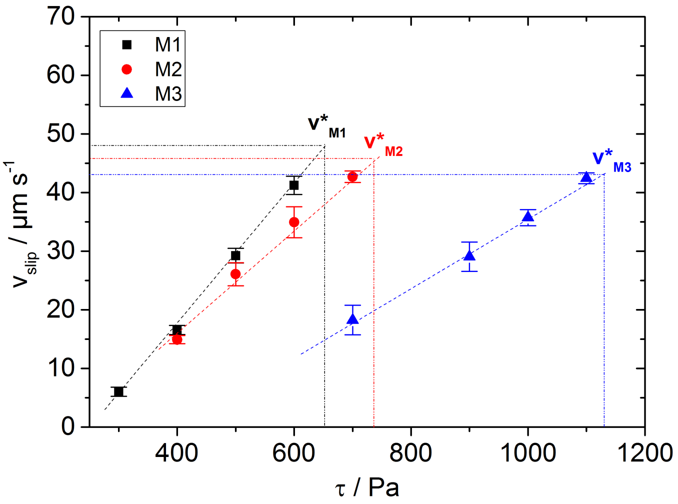

Figure 3.3: Slip velocity of model pastes on steel rheometer plate with roughness $R_q = 1\ \mu m$ as a function of applied shear stress, v_{slip}, determined as described in section 3.3.1. The characteristic slip velocity V^* occurs at the yield stress of the paste.

Oscillatory shear measurements are not limited due to sample spillage or wall slip effects occurring in steady shear experiments. Frequency sweep experiments demonstrate the dominating elastic properties of the vehicles as well as the pastes, i.e., G' is independent of frequency and $G' \gg G''$, in the linear response regime (see Figure 3.14(a) in Appendix A). Figure 3.4(a) shows the corresponding $G_0 = G'(f = 1\ Hz)$ data for all investigated samples.

As for τ_y and η_{low}, we find a strong increase in G_0 with increasing T-Max content and again this increase is more pronounced for the vehicle than for the paste. Amplitude sweep experiments (at a fixed frequency $f = 1\ Hz$) were performed to determine the critical stress amplitude $\hat{\tau}_c$ at which $G' = G''$ (see Figure 3.14(b) in Appendix A). This crossover indicates a structural breakdown and this kind of oscillatory shear test is considered as an alternative approach to determine τ_y [107]. Corresponding $\hat{\tau}_c$ data for all investigated vehicles and silver pastes are displayed in Figure 3.4(b). As expected, $\hat{\tau}_c$ increases with increasing T-Max content and this effect is less pronounced for the pastes than for the vehicles. The absolute $\hat{\tau}_c$ values agree fairly well with the corresponding τ_y data.

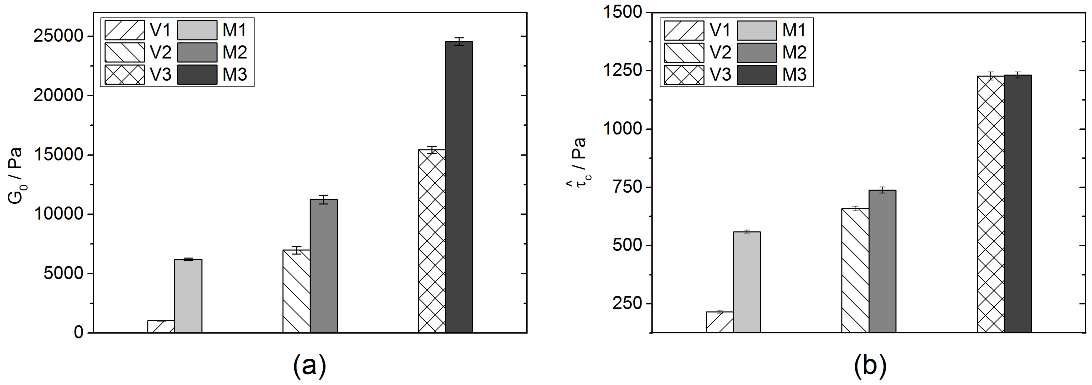

Figure 3.4: (a) Plateau modulus $G_0 = G'(f = 1\ Hz)$ determined in the LVE regime; (b) Critical stress amplitude $\hat{\tau}_c$ determined from the crossover of G' and G'' in amplitude sweep experiments performed at $f = 1\ Hz$. Patterned bars corresponds to vehicles, filled bars represent silver pastes.

A three-interval shear test as suggested in [18] and later used in [24, 25, 91, 95] was performed to characterize the structural recovery after large shear deformation. Here, the degree of recovery is calculated as the ratio of G'_{fin} obtained as the limiting G' value in section III and G'_{ini} determined in section I. In the second interval, a shear deformation amplitude $\hat{\gamma} = 90\ \%$ is applied for 150 s to assure extensive structural breakdown, and to achieve good paste transfer across the screen [18]. Corresponding data shown in Figure 3.5(a) reveal that the paste structure is irreversibly damaged during high shear in section II.

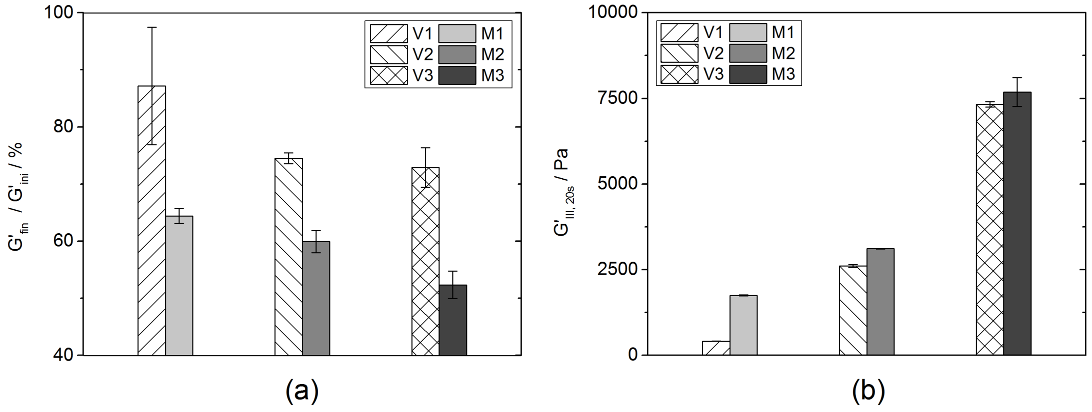

Figure 3.5: (a) Degree of structural recovery for vehicles and silver pastes represented as G'_{fin}/G'_{ini} determined from oscillatory three-interval thixotropy tests. The applied oscillatory amplitude in sections I and III is in each case $\hat{\gamma}_{I,III} = 0.05\ \%$ and in section II $\hat{\gamma}_{II} = 90\ \%$; (b) Absolute degree of recovery $G'_{III,20\ s}$ after 20 s rest time in section III at $\hat{\gamma}_{III} = 0.05\ \%$. Patterned bars correspond to vehicles, filled bars represent silver pastes.

Similar results have been previously reported for silver [95] and ZnO pastes [91]. The degree of irreversible damage is generally controlled by the interactions among solid particles, thixotropic agent and binder [108]. Here, this change in structure is more pronounced for the pastes than for the vehicles and increases with increasing T-Max content as already reported for ZnO pastes [91].

Additionally, we have determined the modulus G' in section III, 20 s after cessation of high shear deformation. This time period approximately corresponds to the interval between the solar cell printing step and the drying step [25]. As shown in Figure 3.5(b) $G'_{III,20\ s}$ increases with increasing T-Max content. This is again true for the vehicles as well as for the pastes, and obviously the irreversible damage of the paste structure, which also increases with increasing T-Max content, does not compensate for this effect. It should be kept in mind, however, that the characterization of structural recovery relies on oscillatory shear deformation data obtained on a time scale of several tenths of seconds. By contrast, printing and spreading of silver lines in solar cell metallization happens in less than 0.1 s based on high-speed camera observations [91] and may not be related to the long term rheological changes characterized by this kind of three-interval thixotropy test [18, 24, 25, 95].

Filament breakage length, respectively fracture strain ϵ, was determined in uniaxial extension to understand the paste behavior during snap-off in the printing process. Paste sticking to the substrate or the screen experiences a tensile stress when the screen detaches from the wafer. We used a commercial CaBER device to determine the fracture strain ϵ. A constant stretching velocity $v_{stretch} = 110\ mm\ s^{-1}$ was chosen and the corresponding ϵ values are shown in Figure 3.6. Obviously, fracture strain decreases with increasing T-Max content. Again, this effect is more pronounced for the vehicles than for the pastes. Similar behavior was observed earlier for ZnO pastes with different T-Max content [91]. The sample spanning network structure provided by this thixotropic agent cannot withstand strong tensile stresses and exhibits brittle failure.

In summary, this section provides a comprehensive rheological characterization of silver pastes and corresponding vehicles essentially differing in the amount of included thixotropy agent T-Max. The parameters τ_y, $\hat{\tau}_c$, G_0, and η_{low} are tightly related, and all increase strongly with T-Max concentration. However, this effect is more pronounced for the vehicles than for the pastes, indicating that the structure provided by the thixotropic agent is partly disturbed by the added silver particles. The fracture strain ϵ in uniaxial extension is another, independent paste rheology parameter. This quantity decreases substantially with increasing T-Max content. The structure provided by the thixotropic agent is destroyed during high shear deformation and only partly recovers after cessation of flow. The degree of irreversible

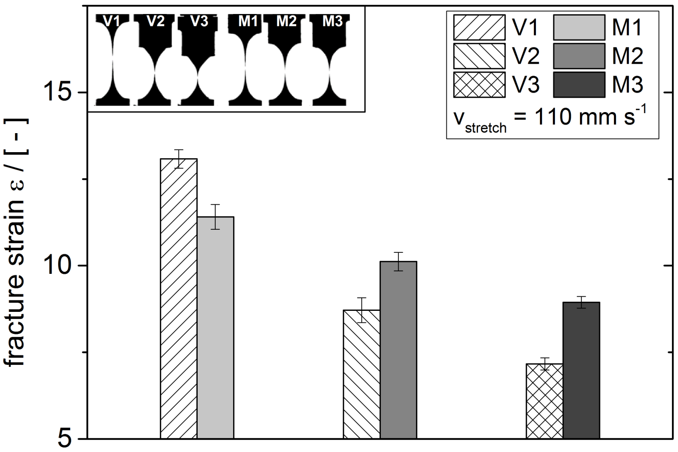

Figure 3.6: Fractue strain ϵ results obtained from sample stretching experiments measured with the capillary breakup elongational rheometer (CaBER) device at $v_{stretch} = 110\ mm\ s^{-1}$ stretching speed. Exemplary pictures of stretched and broken filaments for vehicles and silver pastes are shown inset. Patterned bars correspond to vehicles, filled bars represent silver pastes.

damage increases with increasing T-Max content. Furthermore, the slip on steel surfaces (determined at stresses below τ_y) decreases with increasing T-Max content. Finally, high shear viscosity is a rheological quantity which, in contrast to all other rheological parameters mentioned above, does not vary with the thixotropy agent content. It should also be noted that the wetting properties of the silver pastes are not affected by the thixotropy agent. In the next section, we will discuss how the distinct differences in flow behavior of the prepared silver pastes are seen in the properties of finger lines obtained via screen-printing.

3.4.2 Printed finger morphology characterization

An overview of our 156×156 mm^2 test layout pattern printed on monocrystalline (Cz) Si solar cell at speed of 210 $mm\ s^{-1}$ is represented in Figure 3.7.

Here we used paste M1, but similar results were obtained for M2 and M3. This test layout contains eight finger openings from 20 to 55 μm. Based on this example, uniform, interruption-free printed finger lines can be observed down to 25 μm finger opening. It should be noted that our layout screen includes a 13 μm thick emulsion over mesh (EOM) layer. Interruption-free printing through a 20 μm finger opening would require an EOM layer thickness below 10 μm, as is typically used in fine line printing [25, 109, 110]. In general, print results are not only affected by paste rheology or wetting properties, but also by the printer hardware, such as the screen (design of steel mesh and EOM type and layer thickness), and printer settings (e.g., squeegee angle, squeegee speed, snap-off distance and the magnitude of the force that presses the squeegee against the screen and substrate) [21].

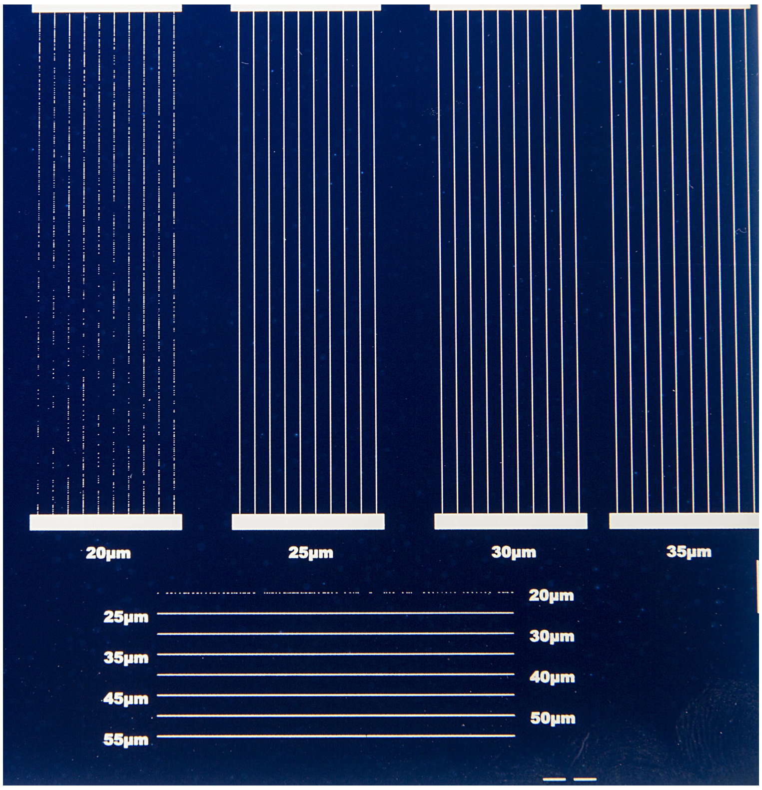

Figure 3.7: Model silver paste M3 printed on a (Cz) Si-wafer using a test layout pattern with eight different finger openings between 20 and 55 μm at printing speed $v_{print} = 210\ mm\ s^{-1}$.

However, our focus is the characterization of finger lines printed through 25, 30, and 50 μm finger openings at various printing velocities $v_{print} = 70$, 140, and 210 $mm\ s^{-1}$. For the layout screen used here, these finger openings provide uniform interruption-free finger lines suitable for a systematic study of the influence of paste composition, as well as printing speed on the morphology of printed lines. Paste transfer, or laydown, is a characteristic feature of a printing process not only for metallization of solar cells. Results for pastes M1-M3 obtained with the above-mentioned layout screen at different printing speeds for a 50 μm finger opening are summarized in Table 3.2. Essentially the same paste laydown of about 53 mg is achieved, irrespective of paste composition and printing speed; however, at low printing speeds paste M3 enables a slightly higher transfer of 56 mg.

The differences in wall slip previously shown to have a strong effect on paste transfer [26, 27] do not show up here and we attribute this to the low absolute slip velocity values measured on a smooth steel plate (section 3.4.1) indicating that slip is of minor relevance for the pastes investigated.

Table 3.2: Paste transfer for model silver pastes M1, M2, and M3 obtained through 50 μm finger opening at different printing velocities 70, 140, and 210 $mm\ s^{-1}$.

printing speed	**paste laydown**		
	M1	**M2**	**M3**
70 $mm\ s^{-1}$	52.00 ± 0.85	53.60 ± 0.98	56.10 ± 1.06
140 $mm\ s^{-1}$	52.30 ± 0.53	53.80 ± 0.14	56.00 ± 0.12
210 $mm\ s^{-1}$	52.90 ± 0.14	53.20 ± 0.64	53.50 ± 0.64

Key characteristic parameters of printed electrodes are finger width w_f and its fluctuation, finger height h_f, and the corresponding cross-sectional area A_f and aspect ratio AR. Evaluation of these parameters is carried out using a 3D laser scanning microscope. In Figure 3.8, finger width results are plotted in a box plot diagram versus printing speed for electrode lines printed through $d_{finger} = 50\ \mu m$ finger opening.

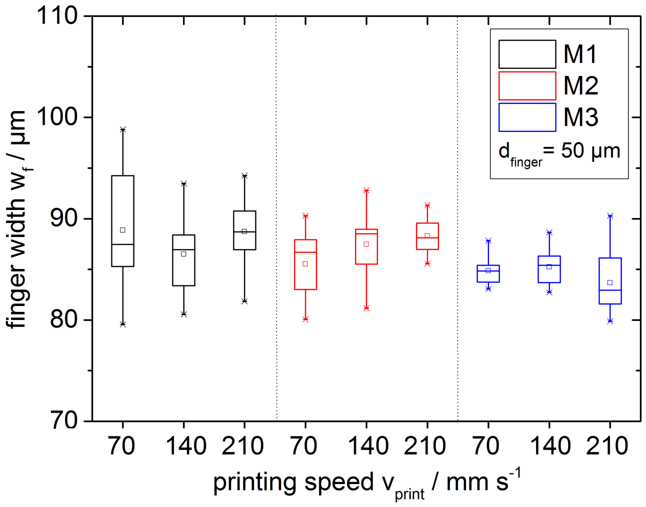

Figure 3.8: Resulting finger width w_f printed through a 50 μm finger opening are plotted versus printing speed v_{print} (70, 140, and 210 $mm\ s^{-1}$) for model silver pastes M1, M2, and M3.

Results for pastes M1-M3 are separated into three groups. Our results confirm that the variation of printing speed has no significant effect on finger width, and w_f seems to decrease slightly with increasing T-Max content. However, this effect is more pronounced at lower mesh openings and will be discussed below. During the screen-printing process pastes are exposed to high shear rates, especially when pushed through the finger openings [19, 21]. Since the high shear viscosity is the same for all investigated pastes, a variation in w_f is not expected. In all printing trials, the finger width is about 75 % higher than the finger opening. This is attributed to the low absolute value of the viscosity in the high shear regime. A finger width w_f closer to the finger opening can be achieved using pastes with substantially higher viscosity at high shear rates [91].

Since printing speed has no influence on finger width here, we decide to characterize further geometrical parameters of printed lines only for printing speed $v_{print} = 210\ mm\ s^{-1}$, which is close to the state-of-the-art in front-side metallization of Si solar cells. The results of finger lines printed through 25, 30, and 50 μm finger openings are shown in Figure 3.9. Finger width is obviously smaller for a narrower finger opening but the deviations between resulting finger width w_f and finger opening are even more pronounced for smaller openings; e.g., for the 25 μm finger opening, the obtained true line width is almost three times larger than the opening of the screen. Overall, there is a small effect of sample composition on line width and w_f decreases from M1 to M3, i.e., with increasing T-Max content. We attribute this to the two-fold increase in τ_y. The weak dependence of w_f on the inverse of the product $(\tau_y \cdot \eta_{high})$ reported in [91] for two series of ZnO pastes with varying content of T-Max or EC binder, respectively, also appears to be revealed here.

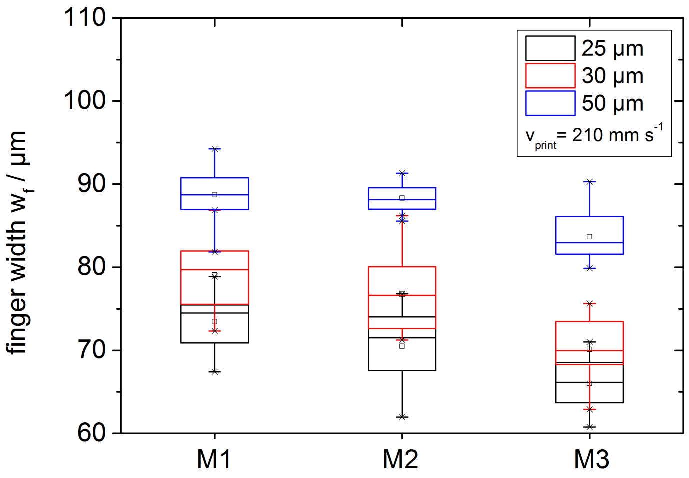

Figure 3.9: Finger width values for M1, M2, and M3 printed through 25, 30, and 50 μm finger openings at $v_{print} = 210\ mm\ s^{-1}$.

In all cases we observe severe fluctuations in line width. The electrical properties of printed electronic devices are not only determined by the printed line width but also by the homogeneity of the obtained structures in terms of width and height. Therefore, the degree of fluctuation in finger width is determined for 10 lines, each 40 mm in length. The width is evaluated at each pixel position. Afterwards, the standard deviation Δw_f is calculated to characterize the fluctuations of the printed electrode width. In Figure 3.10 the relative fluctuation $\Delta w_f/w_f$ is plotted for each paste printed through 25, 30, and 50 μm finger openings.

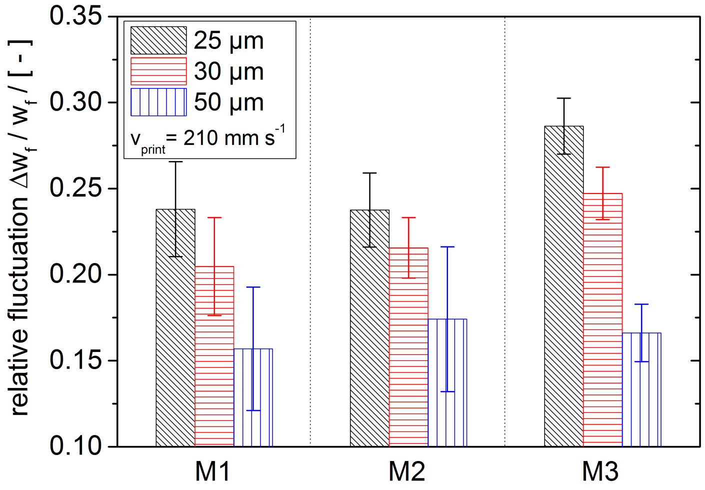

Figure 3.10: Degree of fluctuation in dried finger line width after screen-printing at $v_{print} = 210\ mm\ s^{-1}$.

The relative fluctuations in line width clearly decrease strongly with increasing finger opening, although the absolute values of w_f are fairly close and much larger than the used finger opening. Paste spreading and hence line width, as well as line width fluctuations, depend on the wetting properties of the paste on the substrate and also the paste rheology, especially at high shear rates. Neither the wetting behavior or η_{high} vary among the pastes investigated here and, hence, it seems to be reasonable that $\Delta w_f/w_f$ does not vary much with paste composition. For smaller finger openings, relative finger width fluctuations seem to increase slightly with increasing yield stress. It should also be noted that the characteristic length scale of the pyramidal wafer surface texture is much smaller than the observed line width fluctuations.

Finger height h_f results obtained for pastes M1-M3 printed through 25, 30, and 50 μm finger openings at printing speed $v_{print} = 210\ mm\ s^{-1}$ are shown in Figure 3.11. These data suggest that h_f weakly increases with T-Max concentration, i.e., with increasing yield stress. An opposite trend was observed for w_f (see Figure 3.9) and, accordingly, the aspect ratio $AR = h_f{\cdot}w_f^{-1}$, shown in Figure 3.12(a), clearly increases with increasing τ_y. On the other hand, the cross-sectional area $A_f \approx w_f{\cdot}h_f$ is independent of sample composition due to the opposing effects of τ_y on w_f and h_f (Figure 3.12(b)). This is consistent with the initially stated paste transfer independent of paste composition. As expected, the absolute value of A_f, and, hence, the paste transfer increases with increased finger opening.

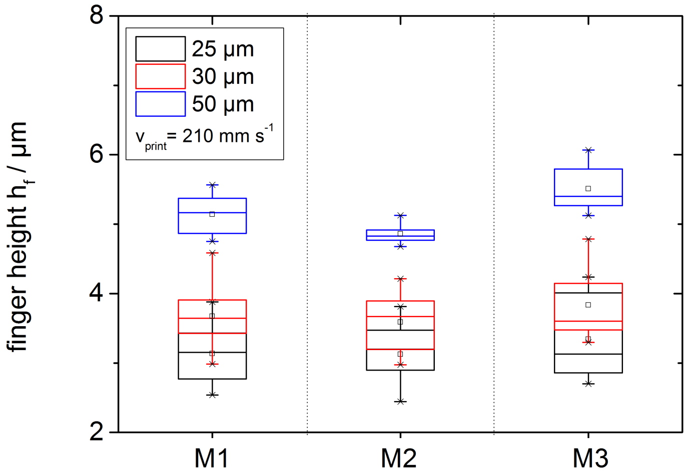

Figure 3.11: Finger height h_f results for M1, M2, and M3 printed through 25, 30, and 50 μm finger opening at $v_{print} = 210\ mm\ s^{-1}$.

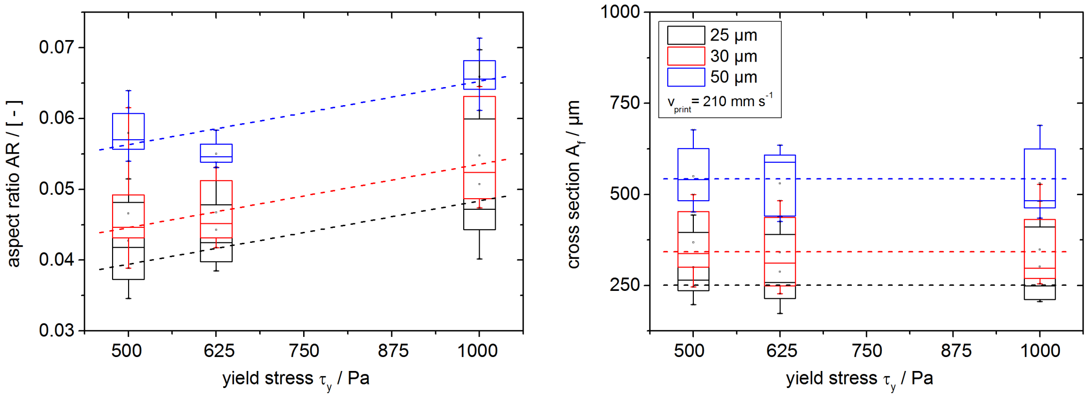

(a) (b)

Figure 3.12: (a) Aspect ratio AR determined for M1, M2, and M3 at 25, 30, and 50 μm finger openings and 210 $mm\ s^{-1}$ printing speed in relation to the yield stress; (b) Finger cross sections A_f obtained for M1, M2, and M3 at 25, 30, and 50 μm finger openings and $v_{print} = 210\ mm\ s^{-1}$ as a function of yield stress.

The variations in paste transfer and also in finger cross-sectional area are small since high shear viscosity and substrate wetting behavior are similar for all pastes, and the differences in wall slip velocity do not affect paste transfer because the overall contribution of slip to paste transport through the finger opening is supposed to be small. However, the aspect ratio AR increases significantly with increasing T-Max content due to its impact on yield stress and low shear viscosity. This should finally show up in an improved cell efficiency η_{el} which is proportional to the short circuit current density J_{SC} increasing with AR corresponding to reduced shading losses.

Grid and line resistance, however, solely depend on A_f (and its fluctuations) and hence should not be affected here, since A_f is independent of paste composition.

3.5 Conclusion

We have thoroughly investigated the rheological properties of three silver pastes suitable for front-side metallization of Si solar cells, and corresponding vehicles mainly differing with respect to the concentration of thixotropic agent Thixatrol Max. Even minor changes in T-Max concentration led to drastic changes in rheological response. This effect is more pronounced for the vehicles than for the pastes, indicating that the network structure formed by this hydrogenated castor oil is partly disturbed by the suspended silver particles.

Increasing the T-Max concentration by only 15 % leads to a twofold (at least) increase of yield stress, low shear viscosity and storage modulus in the pastes. At the same time, the fracture strain in uniaxial extension drops by about one-third. These T-Max based vehicles and pastes are sensitive to high shear deformation and an irreversible damage of the structure was found in widely used, so-called three-interval thixotropy tests. Wall slip on smooth steel plates was observed for the pastes, however, the absolute slip velocity values were small compared to other silver paste formulations. Finally, it should be noted that the high shear viscosity of the samples obtained at a shear rate of $3{\cdot}10^5$ s^{-1} was independent of T-Max concentration; obviously, the network structure breaks down at such high shear rates.

We screen-printed these pastes using a layout screen with different finger openings at various printing speeds in order to elucidate how the substantial changes in paste rheology show up in the printed finger line morphology. We focused on finger openings between 25 and 50 μm and varied printing speeds between 70 and 210 $mm\ s^{-1}$. In all cases the observed true line width was much larger than the finger opening and we attribute this to the low high shear viscosity of the pastes since the EC binder content was kept constant at a low level.

The observed strong fluctuations in line width were mostly independent of finger opening and paste composition. We assume this phenomenon is mainly controlled by wetting properties, which are not affected by the thixotropic agent and can be safely assumed to be the same for all investigated pastes. However, finger width w_f and height h_f turned out to depend weakly on paste composition. Whereas w_f decreases, h_f increases slightly with increasing T-Max concentration, i.e., with increasing yield stress τ_y. Accordingly, the aspect ratio $AR = h_f{\cdot}w_f^{-1}$ exhibits a distinct dependence on τ_y, whereas the cross-sectional area A_f is independent of sample composition (i.e., τ_y) consistent with the gravimetric paste transfer determination revealing that paste laydown is independent of T-Max content. As pointed out earlier, paste transfer strongly depends on wall slip and this feature is mainly controlled by particle loading and solvent wetting properties not modified here. Our results do not support the hypothesis that fracture strain significantly affects snap-off and hence paste transfer. We also do not see that differences in structural recovery or degree of irreversible structural damage as characterized in three-interval oscillatory shear tests are manifested in the printing results.

In summary, the screen-printing process was found to be robust against changes in paste rheology. A twofold increase in τ_y induces a 15-20 % increase in finger line aspect ratio AR without affecting the total laydown. This observed increase in AR should have a significant impact on electrical cell properties due to reduced shading losses obtained from finer line-widths at a given cross-sectional area.

Author Contributions

Conceptualization, C.Y., M.K. and N.W.; Methodology, C.Y., M.K. and N.W.; Investigation, C.Y.; Writing-Original Draft Preparation, C.Y. and N.W.; Writing-Review & Editing, C.Y., N.W. and M.K.; Visualization, C.Y.; Supervision, N.W.

Funding

This research was funded by the Federal Ministry for Economic Affairs and Energy (0325775G) and the 100 prozent erneuerbar stiftung.

Acknowledgements

The authors would like to thank to Heraeus Deutschland GmbH & Co. KG for their support and supply of model vehicles and model pastes, especially A. Grumbach for his help performing the printing experiments in their laboratories in Hanau Germany and for fruitful discussions. Special thanks go to G. Klotz for experimental support in rheological characterization of vehicles.

Conflict of interests

The authors declare no conflict of interest.

Appendix A

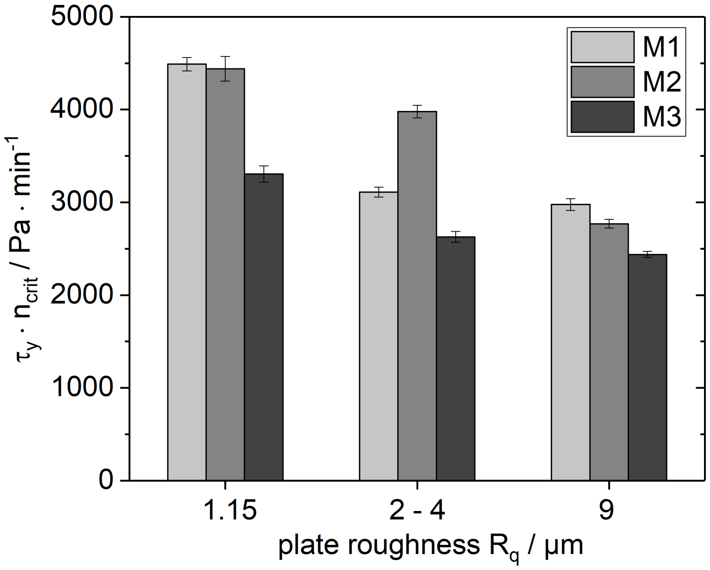

Figure 3.13: Product of yield stress τ_y and critical rotational speed n_{crit} obtained from sample spill investigation at varied plate roughness for M1, M2, and M3.

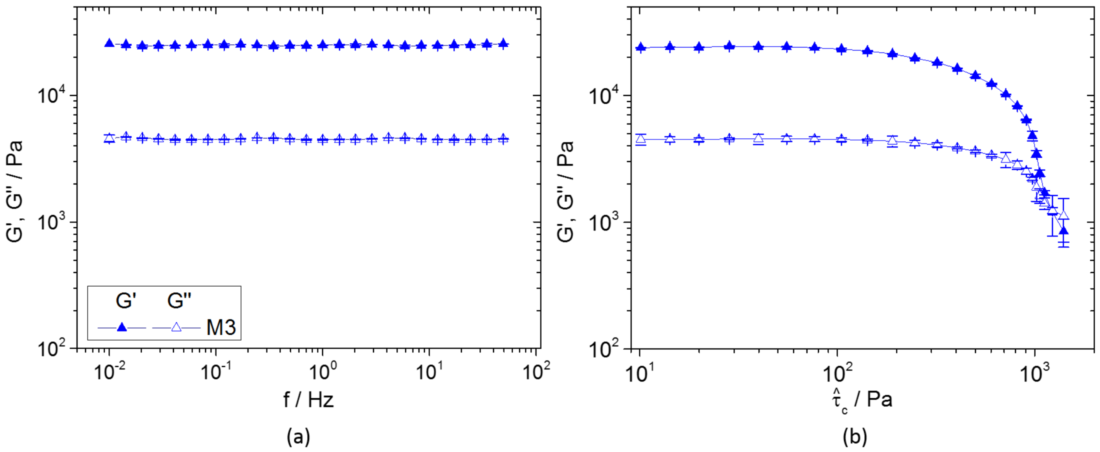

Figure 3.14: (a) Frequency sweep experiment demonstrated for M3; G', G'' vs. frequency f at fixed stress amplitude $\hat{\tau}_c = 25\ Pa$. (b) Amplitude sweep experiment demonstrated for M3: G', G'' vs. stress amplitude $\hat{\tau}_c$ at fixed frequency $f = 1\ Hz$. Pastes M1 and M2 behave similarly.

4. Non-volatile free silver pastes manufactured from capillary suspension formulation concept

Full title:	Non-volatile free silver paste formulation for front-side metallization of silicon solar cells [111]
Authors:	Ceren Yüce, Kuninori Okamoto, Lindsey Karpowich, Adrian Adrian, and Norbert Willenbacher
Status:	published
Bibliographic data:	Solar Energy Materials and Solar Cells 200 (2019) 1100400; doi: 10.1016/j.solmat.2019.110040

Abstract

We present a versatile, cost-effective formulation platform for highly conductive silver pastes used in front-side metallization of silicon (Si) solar cells. Pastes based on the capillary suspension concept include silver particles, glass frit and two immiscible fluids. Capillary forces inferred from the second fluid added only in small fractions induce the formation of a percolating particle network. This provides extended shelf-life and distinct flow properties adjustable in a wide range as demanded by the respective printing process, thus yielding residual-free sintered electrodes. Si-wafers are successfully metallized with such pastes using conventional screen-printing, knotless screen and Pattern Transfer Printing^{TM}. Paste spreading is studied via high-speed imaging during screen-printing on glass plates. Morphology of printed lines is analyzed using laser scanning microscopy. Electrical properties of the cells are characterized employing a solar simulator and electroluminescence spectroscopy. Results are compared to those obtained using commercial pastes including the same silver particles and glass frits. Paste performance strongly depends on the selected secondary fluid. Aspect ratios ≈ 0.4-0.5 can be reached and cell efficiencies $\eta_{eff} \approx 21$ % on Cz- and 18.6 % on mc Si-wafers are obtained. Additional investigations are necessary to further reduce paste spreading and line interruptions thus improving cell performance.

Keywords

additive-free silver paste formulation; capillary suspensions; fine line printing; high-speed imaging; knotless screen; Pattern Transfer Printing; paste rheology; cell efficiency; EL; electrode morphology

4.1 Introduction

The global challenge of climate change pushes electric energy generation from renewable sources, utilizing photovoltaics, wind energy, hydropower, geothermal energy and biomass is strongly growing [1, 2, 3]. Photovoltaic (PV) systems, namely solar cells, play a key role due to their robustness and virtually maintenance-free operation over long time periods ($>$ 25 years). Today more than 90 % of the globally installed PV systems are based on silicon wafer technology which despite of its maturity still is a matter of current research [112, 113] and screen-printing is the dominant production technology for front- and rear-side metallization of these silicon (Si) solar cells [4, 5] due to its easy implementation and its high through-put (currently up to 4000 $wafers/h$ on a single line) [6]. This economically attractive technology is one of the key factors enabling the recent improvement of solar cell efficiency and cost reduction. However, already today about 7.5 % of the global silver production are used for the metallization of solar cells [6]. Thus, a significant reduction of silver consumption per wafer and further enhancement of cell efficiency are essential for an expansion of PV installations. An optimization of the solar cell front-side metallization can be achieved by reducing the finger width w_f and increasing the aspect ratio AR of the screen printed lines. State-of-the-art finger widths achieved by screen-printing goes down to 30 μm [17]. Further reduction of $w_f < 30$ μm and $AR > 0.6$ could facilitate lower shading losses and reduce material consumption [6, 15, 16].

Screen-printing is a robust and cost-efficient production process, but the resulting finger width is limited by the mesh wire thickness and material used in conventional screen manufacturing [4, 33]. New application technologies, such as knotless screen [33], dispensing [34], flexographic print [36], or Pattern Transfer Printing^{TM} (PTP) [37], as well as suitable paste formulations are needed to excel the actual finger width and AR limits.

Typical commercial formulations of screen-printing pastes for front-side metallization consist of conductive material (85-90 $wt\%$), i.e. micron sized spherical silver particles $x_{50} \approx$ 1-3 μm, dispersed in a continuous phase (5-14 $wt\%$), the so-called vehicle. This is a mixture of organic solvent containing non-volatile organic binders and additives to control flow properties and to strengthen the adhesion of printed electrodes on the substrate. In addition, micron sized leaded glass frit (1-5 $wt\%$) is dispersed as a second solid component to etch off the anti-reflection layer on the wafer surface and to create a contact between the printed electrodes and the n-doped Si-wafer layer [57, 59, 60, 61, 62, 63, 64].

In this study, we present highly conductive silver pastes prepared as so-called capillary suspensions, i.e. ternary solid/fluid/fluid systems [29] without any addition of non-volatile organic components [28]. The special feature is that the used liquids, termed as bulk fluid and secondary fluid, are immiscible and accordingly a sample-spanning particle network forms driven by the capillary forces acting in the ternary system. The strength of this particle network results in a high yield stress and guarantees storage stability for several months, even with the high density difference between silver particles and continuous phase used here [28, 29, 30, 31]. This network, however, breaks down when external stresses are applied and this results in a high degree of shear thinning which can be varied in a wide range to meet the requirements of different coating processes [31]. The flow behavior of such pastes is not only determined by the size, shape and volume fraction of the solid phase but also by the wetting properties of both fluids on the particle surface as well as the interfacial tension Γ_{int} between bulk and secondary fluid [31]. Accordingly, a large number of liquid combinations can be chosen for silver paste formulation in combination with commercially available silver and glass frit to meet a wide range of product and process-specific requirements. Our research is motivated by the expected metallization cost reduction coming with this paste concept. The fabrication of non-volatile free pastes is simpler than that of commercial paste since the number of ingredients is lower, in particular it does not include a thixotropic agent which requires heat treatment to be dissolved or dispersed properly. This is the direct but relatively small effect on cost reduction. Beyond that, we expect a significantly better electrical performance, provided a state-of-the-art printing quality can be achieved, according to preliminary experiments [28] silver consumption may be cut by 50 %.

In this study, we use this new paste formulation concept together with different printing technologies: the screen-printing method with conventional standard screen as well as knotless screen, and the PTP method, for ultra-fine front-side metallization. Knotless screen is characterized by the 0° mesh angle, which is the orientation of the mesh wire to the screen frame and hence the direction of finger lines. The advantage is that the wire intersections in the open channels which are known from the 22.5° orientated mesh wires in conventional screens are absent here. Due to less wires crossing the mesh openings, so-called mesh marks are reduced, paste transfer is expected to be enhanced, finger uniformity should be improved and a better conductivity is expected even at lower finger width [33, 48]. Recently, finger widths of $w_f = 28\ \mu m$ could be obtained using knotless screen design [38]. PTP is a contactless printing technology based on laser induced paste deposition from a polymer substrate, so-called tape. This method enables the manufacturing of ultra-fine finger lines ($< 20\ \mu m$) with high aspect ratio (> 0.6) since the trench width and height in the typically used tapes are $20\ \mu m$ [37, 39].

The high conductivity of silver pastes based on capillary suspensions is demonstrated in preliminary lab scale stencil printing test. A twofold increase of conductivity compared to layers produced from commercial pastes under identical conditions could be gained [28]. The non-volatile organic additives in commercial silver paste formulations do not necessarily burn out without residues during sintering. Thus, small amounts of residual carbon can considerably worsen the conductivity of the printed layer. These residues are demonstrated in sintered electrodes made from a commercial paste using energy dispersive electron microscopy (EDX) imaging here (Figure 4.1).

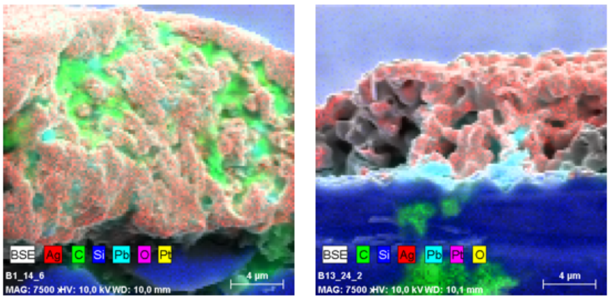

Figure 4.1: Energy dispersive electron microscopy (EDX) image of screen-printed and fired commercial paste (left) and additive-free formulation paste (right) printed on a Si-wafer to demonstrate the presence of carbon impurities, here shown in green color.

In the cross-section of sintered finger lines made from a commercial silver pastes residual carbon (C = green color) is evident, while in the electrode cross-section of the additive-free capillary suspension type paste no carbon is detected. The absence of non-volatile components should result in higher finger line conductivity since the electrical conductivity is not disturbed by impurities. However, this is not proven experimentally yet due to a lack of data for printed lines with similar cross-section and longitudinal uniformity made from both types of paste.

Furthermore, burned-out polymeric binders are likely to contaminate the sintering furnace and ventilation ductwork and residues may cause unexpected changes to the sintering furnace performance, excessive downtime for maintenance and possible fire hazard as carbonaceous residues accumulate within ventilation ductwork. Clean-burning binder systems have been developed to reduce these detriments [32]. Our paste formulations based on the capillary suspension concept offer an inherent benefit with respect to the sintering process since paste stabilization is done with volatile solvents only.

We prepare pastes with different composition and determine rheological parameters relevant for paste characterization, as described in [95, 100] considering paste rheology to be relevant for printing performance [18]. Furthermore, a detailed investigation of finger line morphology obtained from standard screen printing is done to understand the relationship between paste composition, its rheological properties, and line shape as well as its impact on cell performance. Analysis of line morphology right after printing, drying, and firing elucidates the change in finger line during the drying and sintering steps. High-speed imaging experiments [91] are performed to capture finger shape development for additive-free suspensions during standard screen-printing.

4.2 Experimental procedure

4.2.1 Materials

Capillary suspensions are ternary solid/fluid/fluid systems. The bulk fluids used in this work are mixtures of two polar liquids, glycerol (Carl Roth, Germany) and ethylene glycol (VWR, Germany). The amount of ethylene glycol dissolved in glycerol is varied between 0 and 100 $wt\%$ corresponding to a variation in viscosity between 20 $mPas$ and 1060 $mPas$ (Table 4.1).

Three proprietary mixtures of nonpolar volatile organic solvents (termed SF1, SF2, and SF3) differing in their boiling point (215 °C, 244 °C, and 260 °C) are used as secondary fluid. All of them are immiscible with the above mentioned bulk mixtures. Further differences are obtained for the interfacial tension Γ_{int} between bulk and secondary fluid determined with the pendant drop method [114, 115, 116], values vary between 1.6 mN/m and 11.2 mN/m depending on the selected liquid combination (see supplementary, Figure 4.13). In one series of pastes Γ_{int} is decreased by increasing the ethylene glycol content of the bulk fluid, in a second series interfacial tension is varied using SF1, SF2, or SF3 together with one specific bulk system.

Table 4.1: Viscosity values of various bulk fluid composition mixtures used for the capillary suspension formulation.

glycerol content / *wt%*	**ethylene glycol content** / *wt%*	**bulk fluid viscosity η_{bulk}** / mPas
0	100	20 ± 1
20	80	36 ± 1
40	60	77 ± 2
60	40	166 ± 3
80	20	404 ± 14
100	0	1060 ± 9

For conductive front-side metallization pastes, we use micron sized, almost spherical and hydrophobically modified silver (Ag) particles (type T, H, and M, Figure 4.2). Type M Ag particles, product number K-7418P, are purchased from Metalor Technologies (UK) Ltd., type T is provided by the industrial partner, Changzhou Fusion New Material Company (China) and type H by Heraeus Photovoltaics (United States).

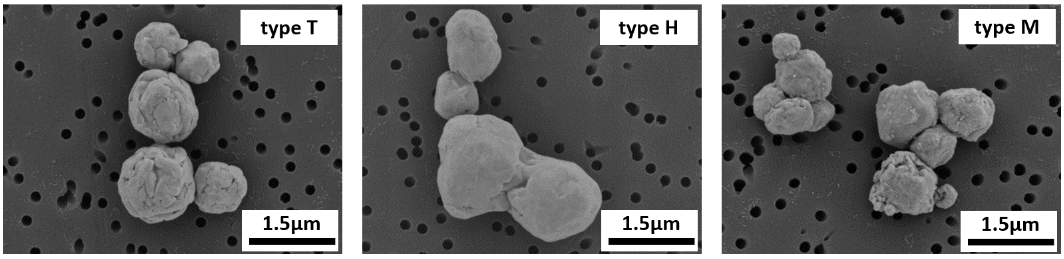

Figure 4.2: SEM images of micron sized spherical silver particles type T, H, and M.

Contact angle measurements on silver surface are performed according to the sessile drop method [117, 118, 119]. The contact angle of a water drop on silver tablet made from the particles mentioned above in air environment is $\Theta = 123.1 \pm 3.5°$ for type T, $\Theta = 132.5 \pm 2.5°$ for type H, and $\Theta = 110.0 \pm 3.9°$ for type M. All determined values are higher than 90° and hence all types of silver particles are classified as hydrophobic. Surface energies $\Gamma_{surface}$ (see supplementary, Figure 4.14) are calculated from measured contact angles for a series of liquids according to the method of

Owens and Wendt [120]. These are in the range of $\Gamma_{surface} = 40\text{-}60\ mN/m$, which further suggests that the particles used here are not behaving like precious metals since the expected surface energy $\Gamma_{surface}$ for pure silver $\Gamma_{surface,\ pureAg} = 1250\ mN/m$ is several orders of magnitude higher. Surface energy measurements confirm that the silver particles are surface modified particles to facilitate the dispersibility in nonpolar organic solvent.

To ensure electrode contacting during the fast firing process we also add micron sized leaded glass frit (type GT and GH, Figure 4.3). Glass frit type GT is provided by Changzhou Fusion New Material Company (China) and type GH by Heraeus Photovoltaics (United States). Particle size distributions are determined using Fraunhofer diffraction and corresponding data are listed in Table 4.2.

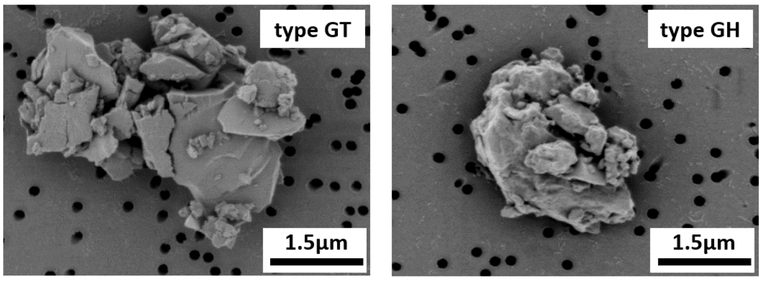

Figure 4.3: SEM images of micron sized glass frit type GT and GH.

Table 4.2: Overview of particle size distribution for silver particles type T, H, and M as well as for glass frit type GT and GH; x_{10} is the 10th percentile of all particle diameters, which means that 10 % of the observations are less than the x_{10} value, x_{50} is the median, corresponds to the 50th percentile, and x_{99} is the 99th percentile, these values are determined using Fraunhofer diffraction.

silver paste			
type	$\boldsymbol{x_{10}}$ / μm	$\boldsymbol{x_{50}}$ / μm	$\boldsymbol{x_{99}}$ / μm
T	1.12 ± 0.02	2.19 ± 0.01	5.11 ± 0.11
H	0.97 ± 0.10	2.53 ± 0.07	9.27 ± 0.55
M	1.08 ± 0.03	2.05 ± 0.06	4.78 ± 0.02
glass frit			
type	$\boldsymbol{x_{10}}$ / μm	$\boldsymbol{x_{50}}$ / μm	$\boldsymbol{x_{99}}$ / μm
GT	0.53 ± 0.01	2.66 ± 0.04	11.85 ± 4.12
GH	0.25 ± 0.01	1.08 ± 0.03	9.51 ± 0.03

Three-phase contact angle Θ_C measurements [117, 118, 119] are performed for a SF1 and SF2 droplet on silver tablets made from Ag particles of type T, H, and M surrounded by 60 *wt*% ethylene glycol dissolved in glycerol (Table 4.3). For both fluids the three-phase contact angle Θ_C on Ag type T and H is well below 90°, and therefore it can be concluded that a pendular state network is formed in the corresponding capillary suspensions. For Ag type M a capillary state network structure is formed since $\Theta_C > 90°$ [121, 122]. Within experimental accuracy the wetting behavior of fluids SF1 and SF2 is similar on all three types of silver particles.

Table 4.3: Three-phase contact angle Θ_C of SF1 or SF2 droplets formed on silver tablets made of type T, H, and M silver particles surrounded by a mixture of 60 *wt*% ethylene glycol dissolved in glycerol.

Ag particle	$\boldsymbol{\Theta_{C,SF1}}$	$\boldsymbol{\Theta_{C,SF1}}$	**capillary network** [121, 122]
type T	29.5 ± 3.8	24.8 ± 4.5	pendular state
type H	19.1 ± 2.4	16.8 ± 2.5	pendular state
type M	101.4 ± 1.1	108.0 ± 5.5	capillary state

Composition and characteristic parameters of pastes used in the different printing experiments are summarized in Table 4.4, Table 4.5, Table 4.6, and Table 4.7 shown in chapter 4.3.

4.2.2 Process route for silver paste preparation

The process route for silver paste preparation (Figure 4.4) based on the capillary suspension concept is fast and simple compared to commercial silver paste manufacturing. Processing time is decreased since additives typically included in commercial silver pastes which are activated at elevated temperature to form a sample-spanning network in the fluid phase are not included [123]. All components (silver particles, glass frit, bulk, and secondary liquid) are placed in a bottle (1) and then mixed for 30 *s* at 2000 *rpm* using a non-contact planetary mixer (SpeedMixer^{TM}, Hauschild GmbH) (2). Capillary bridges are formed between the particles, but a few agglomerates are still present in the paste (3). Thus, the subsequent use of a three-roll mill (EXAKT 80E, EXAKT Advanced Technologies GmbH) is essential to break agglomerates by changing the gap distance stepwise from 40 μm down to 7 μm. The processing speed for de-agglomeration is set to 90 *rpm* (4). Obtained pastes include air bubbles after the milling process due to the high paste viscosity (5). These bubbles are removed using the non-contact planetary mixer with the same settings as in the previous mixing step (6). Following these steps allows to create a homogeneous and agglomerate-free silver paste which is also stabilized against sedimentation due to the formed capillary bridges between the solid particles (7). Storage stability is checked after 6 months, 1 year, and 2 years. Pastes do not dry and no phase separation is observed. For commercial pastes phase separation typically occurs after 6 months.

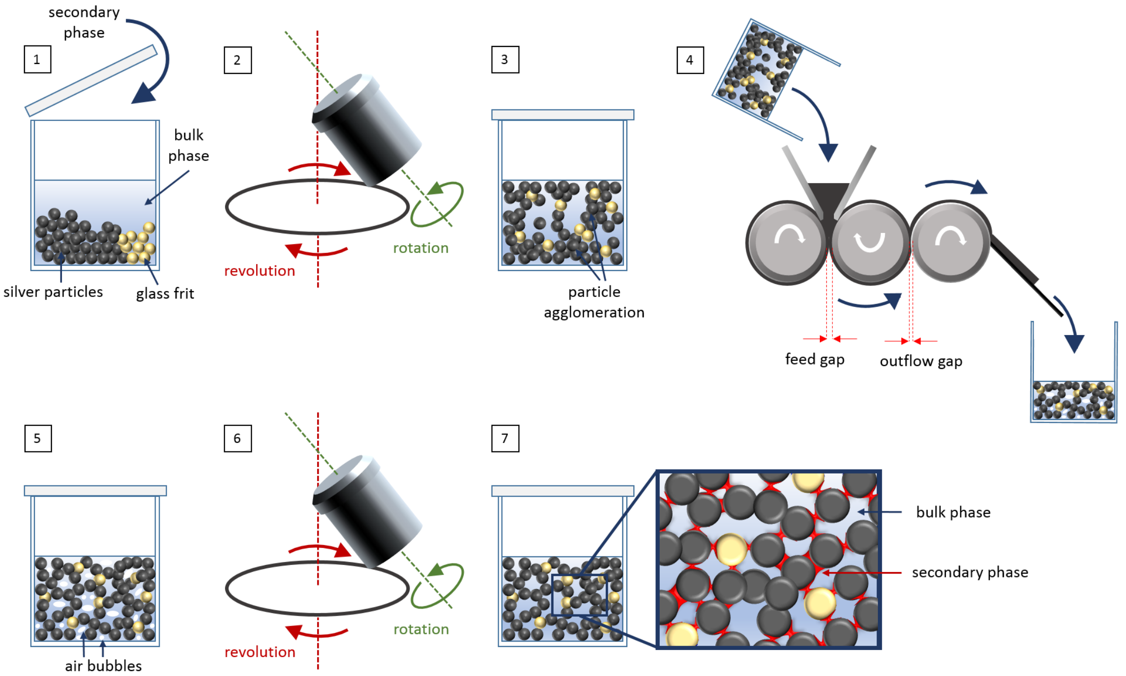

Figure 4.4: Process route for silver paste preparation based on the capillary suspension concept using a non-contact planetary mixer and a three-roll mill for manufacturing of homogeneous additive-free pastes. Sample preparation steps are (1) the addition of all components into one mixing bottle, (2) homogenization of the components with a non-contact planetary mixer, (3) sample-spanning network formation in the paste with visible agglomerates, (4) subsequent paste homogenization with a three-roll mill, (5) & (6) removal of air bubbles using the non-contact planetary mixer, (7) finally the homogeneous sample-spanning network formation in capillary suspension without agglomerates and air bubbles; see text for more details.

4.2.3 Paste characterization

Various rheological parameters considered to be relevant for screen-printing of conductive pastes are determined according to experimental protocols especially suited for highly filled silver pastes [95]. All experiments are conducted at $T = 23\,^{\circ}\mathrm{C}$.

Yield stress measurements are performed using a stress controlled rheometer setup (Haake RS150, Thermo Fisher Scientific) equipped with a vane-and-cup fixture. Measurements are conducted applying a stepwise controlled stress mode, varying the stress from 1 to 5000 Pa in 41 steps equally separated on a logarithmic scale, while each stress is applied for 30 s. The yield stress is defined as the stress at which the sample begins to flow irreversibly and here it is determined from deformation vs. stress data according to the tangent intersection point method [95, 103, 104].

Wall slip velocity v_{slip} is determined in a parallel-plate rheometer (Haake RS150) using a smooth upper stainless steel plate (plate roughness $R_q = 1\ \mu m$, plate radius $r = 10\ mm$, gap height $h = 1\ mm$) and a rough bottom plate ($R_q = 9\ \mu m$) to assure that slip takes place only at the upper plate, but the rest of the sample remains undeformed [26]. Then $v_{slip} = 2\pi nr$, where n is the rotational speed of the plate. According to [26] absolute v_{slip} values may be significantly different on emulsion polymer, which is more relevant for the printing process, compared to a stainless steel surface. The relative changes due to modification of the paste composition, however, can be assumed to be similar for both substrates.

The size of the largest agglomerates in the silver pastes is determined based on the grindometer test. This test utilizes a precisely fabricated bar of stainless steel with parallel spaced grooves in a planar surface. The grooves have a start depth of 25 μm and linearly decrease towards 0 μm at the opposite end of the bar. A small amount of silver paste is placed between a blade and the grooves at 25 μm depth and the blade is moved along the grooves which are filled up with the paste. Resulting scratches in the lane indicate the presence of particle agglomerates. The so-called fineness of grind FOG value is set as the depth of the groove position where the fourth scratch occurs.

4.2.4 Printing technology, electrode morphology and cell performance characterization

Standard screen

Printing tests with standard screen are performed at Changzhou Fusion New Material Company (Shanghai, China). Front-side metallization with a conventional screen (360 meshes per inch, 16 μm mesh wire diameter, 16 μm emulsion over mesh (EOM) thickness, 96 fingers with 37 μm finger opening, and 5 busbars) (Murakami Screen) is carried out on an industrial semiautomatic screen printer (Baccini Soft Line). The used squeegee (Youlan Solar) has a 65 shore hardness and forms a 60° angle with the screen. Metallization is performed at 150 mm/s printing speed and 400 mm/s flooding speed. The snap-off distance is fixed at $h_{snap-off} = 1.9\ mm$. We print 10 multicrystalline Si-wafer (TrinaSolar, diamond wire cut, wafer size, $152.4 \times 152.4\ mm^2$) per paste. The rear-side is metallied with aluminum paste (normal BSF). These printed substrates are dried and fired in an industrial belt furnace (CF-series, Despatch Industries) at a process speed of $v_{beltfurnace} = 6.35\ m/min$ and 9 temperature zones within 100 s. Here, last remaining organic components of the pastes are burned out at around $T \approx 500$ °C before the contact formation of printed electrode and substrate starts at the firing peak temperature $T_{peak} = 740$ °C.

The electrode morphology is examined with a 3D laser scanning microscope (Keyence VK-X200srs). The finger profile, i.e. width w_f and height h_f, are directly measured and the respective aspect ratio $AR = h_f/w_f$, is calculated. Characterization is done at different positions of three printed wafers to get an overview of substrate contacting. Furthermore, cell performance characterization (short circuit current J_{SC}, open circuit voltage V_{OC}, fill factor FF, and cell efficiency η_{eff}) is performed by current vs. voltage (I-V) measurements on a solar simulator (Pasan Lab cell tester).

In addition, we investigate the finger line width right after printing, drying, and firing for standard screen printing tests. Therefore, finger height profile images are captured with a 3D laser scanning microscope and AR is determined always at the same position to evaluate the differences between printed, dried and fired electrodes. The substrates are dried at $T_{dry} = 200$ °C and are fired at $T_{peak} = 740$ °C.

Paste spreading and finger width development of additive-free pastes during the screen-printing process with a standard screen is further observed with high-speed imaging system described in [91]. A modified commercial screen printer (EKRA E2, ASYS Group) and a high-speed camera (MotionBLITZ EoSens mini, Mikrotron GmbH) with an Olympus LMPLFLN 10X objective are used to capture the paste flow through a standard screen (360 meshes per inch, 16 μm mesh wire diameter, 22 μm EOM thickness, and 102 fingers with 35 μm finger opening) (Brave, Taiwan) from underneath. Pastes are printed on a 1 cm thick transparent glass plate which is placed on a movable substrate table. We record the printing process with a frame rate of 1000 fps and a resolution of 1708×832 pixels corresponds to 0.724 $\mu m/pixel$. The used squeegee (BASF Taiwan) has a 75 shore hardness and forms a 60° angle with the screen. Printing tests are performed at 100 mm/s printing speed and snap-off distance is fixed at $h_{snap-off} = 1.6\ mm$. More detailed information about the test protocol and process parameters can be found in [91].

Knotless screen

Front-side metallization with knotless screen (290 meshes per inch, 20 μm mesh wire diameter, 15 μm EOM thickness, and 101 fingers with 27 μm finger opening) (Sanyo Super Screen) is performed at Heraeus Photovoltaics (Conshohocken, Pennsylvania, USA). Printing tests are carried out on an industrial screen printer (EKRA E2, ASYS Group). The used squeegee has a 75 shore hardness and forms a 60° angle with the screen. Metallization is performed at $50 mm/s$ printing speed and $100 mm/s$ flooding speed. The commercial reference paste is printed at 300 mm/s and flooding is done at 400 mm/s. The snap-off distance is fixed at $h_{snap-off} = 2.2\ mm$. Four multicrystalline Si-wafer per paste are printed. The rear-side is metallized with commercial aluminum paste (Al-BSF, deposit is around 1.2 g per cell). In the next step these printed substrates are dried in a convection-dryer at 150 °C for 10 min. After that, the high temperature contact firing step is performed in an industrial belt furnace including 6 temperature zones (Centrotherm 1) at a process speed of $v_{beltfurnace} = 6.5\ m/min$. Here, last remaining organic components of the pastes are burned out at around $T \approx 500$ °C before the contact formation of printed line and solar cells took place at the firing peak temperature $T_{peak} = 817$ °C.

The electrode morphology is examined with a 3D laser scanning microscope (Zeta from KLA-Tencor) to determine finger width, height and corresponding aspect ratio AR. These values are determined at different positions. Furthermore, the solar cells are analyzed using electroluminescence (EL) spectroscopy to get an overview of contacting defects on the substrate [94].

Pattern Transfer Printing

Pattern Transfer Printing^{TM} (PTP) [37] experiments are performed with the Utilight Ltd. (Yavne, Israel) device at ISC Konstanz (Germany). The pastes are applied using two doctor blades on a transparent polymer substrate with 112 pre-embossed trenches (trench width $w_{trench} = 30\ \mu m$, trench height $h_{trench} = 20\ \mu m$). Afterwards, the transfer of the paste pattern to the substrate is induced by laser light irradiation (wavelength = 1064 nm). The dissipated high energy locally increases the temperature above the boiling point of the solvent included in the paste, the resulting gas pressure delaminates the paste from the polymer substrate and it is deposited on the wafer underneath. The gap between polymer substrate and the wafer is set to 200 μm. Here, we use 15 precursors per paste made of $156.75 \times 156.75\ mm^2$ monocrystalline Si-wafer with passivated emitter and rear cell structure (PERC). Rear-side metallization with aluminum paste (Al-BSF) as well as six busbars on the front-side is already screen-printed on the precursor by the manufacturer. Substrates with applied front-side metallization are dried at $T_{peak} = 200$ °C using a Baccini drying oven with one drying cycle for 10 min. The firing process is performed in a fast firing furnace (c.FIRE, Centrotherm AG) with a peak temperature of $T_{peak} = 930$ °C and belt process speed of $v_{beltfurnace} = 7\ m/min$.

Finger width, finger height and cross-sectional area are evaluated with a 3D laser scanning microscope (Olympus) and the aspect ratio is calculated. Cell performance is characterized by I-V-curve measurements using a solar simulator (h.a.l.m. flasher, h.a.l.m. elektronik GmbH) and EL spectroscopy image analysis (LumiSolarCell, Greateyes GmbH) is performed to characterize contacting. With the LumiSolarCell installation it is possible to conduct the measurement with up to 5 busbars and we have to relinquish the sixth busbar present on the cells used here. Two stripes (stripe width = 22 μm) for each cell are used to determine the line resistance value of randomly selected 20 contact fingers using the four-point-probe method [124, 125].

4.3 Results and discussion

4.3.1 Standard screen printing experiments

Printing tests through a standard screen with 37 μm finger opening are performed with nine additive-free silver pastes (Table 4.4). All pastes are made from T-type Ag particles and GT-type glass frit. The fraction of silver particles (87.1 $wt\%$) and glass frit (2.25 $wt\%$) is kept constant. The pastes have a low degree of agglomeration with FOG values varying between 7 and 12 μm.

Table 4.4: Additive-free paste formulations P1-P9 applied for standard screen printing experiments made of $\phi_{Ag} = 87.1$ $wt\%$ ($= 47.4$ $vol\%$) T-type silver particles and $\phi_{glassfrit} = 2.25$ $wt\%$ ($= 4.8$ $vol\%$) GT-type glass frit. Pastes differ in composition of bulk fluid as well as type and amount of secondary fluid.

label	**bulk fluid composition glycerol content** / $wt\%$	**secondary fluid type and amount** / $vol\%$	**yield stress** $\boldsymbol{\tau_y}$ / Pa	**slope of wall slip velocity** $\boldsymbol{\partial v_{slip}/\partial \tau}$ / $\mu m/Pas$
P1	80	SF1 - 5	1479 ± 178	-
P2	60	SF1 - 3	916 ± 80	3.3 ± 0.2
P3	60	SF1 - 5	1153 ± 160	8.6 ± 2.6
P4	60	SF1 - 9	1379 ± 198	-
P5	40	SF1 - 5	836 ± 30	9.1 ± 0.2
P6	60	SF2 - 5	1583 ± 38	6.5 ± 0.3
P7	40	SF2 - 5	661 ± 55	-
P8	40	SF2 - 9	1002 ± 49	8.1 ± 0.2
P9	100	SF3 - 5	1014 ± 16	5.9 ± 0.6

The yield stress of the pastes varies in a wide range (600 $Pa < \tau_y < 1600$ Pa) depending on sample composition. Corresponding data in Figure 4.5 demonstrate that τ_y increases almost linearly with interfacial tension Γ_{int} between bulk and secondary fluid, and at a fixed Γ_{int} the yield stress increases with increasing secondary fluid content as expected for capillary suspensions [31].

The high shear viscosity η_{high} of the pastes is not measured directly here because capillary rheometry experiments require a large amount of sample. It is well known that η_{high} depends on the particle volume fraction ϕ and the viscosity of the suspending medium η_{bulk}, i. e. the composition of the bulk fluid (Table 4.1). Accordingly, η_{high} varies with the mixing ratio ethylene glycol/glycerol. For capillary suspensions the high shear viscosity can be well approximated by that of hard sphere

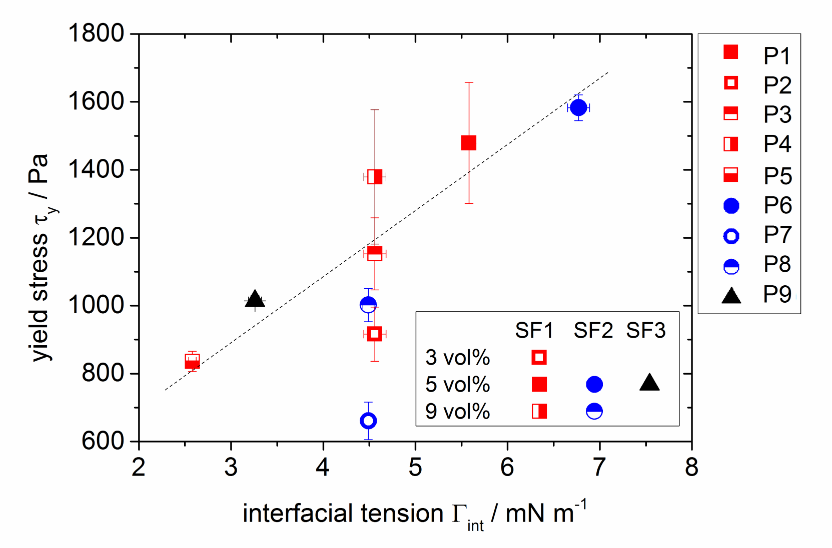

Figure 4.5: Yield stress values for additive-free pastes with different amount of secondary fluid and different interfacial tension Γ_{int} between bulk and secondary fluid.

suspensions and since the volume fraction for the series of pastes investigated here is $\phi = 0.5 =$ constant, $\eta_{high} \approx 10 \cdot \eta_{bulk}$ [106].

The slopes of wall slip velocity $\partial v_{slip}/\partial \tau$ determined from v_{slip} versus shear stress curves (see supplementary, Figure 4.17) vary in a narrow range, but increase systematically with decreasing bulk fluid viscosity. The slip velocities measured here are much higher than for typical commercial pastes [26, 95].

Figure 4.6(a) displays the paste laydown on the substrate determined right after printing as a function of the pastes yield stress, results for the commercial reference paste T are shown for comparison. The laydown for seven out of nine additive-free pastes is in the range between 110 mg and 125 mg, similar as for the commercial paste T and seems not to depend on yield stress τ_y. Only two samples using SF2 as secondary fluid show a significantly lower paste deposit. The reason for this is not clear yet. The wetting properties of the pastes on the Si-wafer are very similar. Figure 4.15 (see supplementary) shows that the contact angle between multicrystalline Si-wafer and bulk fluid increases weakly with increasing ethylene glycol content in the bulk fluid, but for the three pastes including SF2 this variation is small. Furthermore, it should be noted that the contact angle values for the secondary fluids SF1, SF2 and SF3 are similar within experimental error, but substantially lower than those of the bulk fluids (see supplementary, Figure 4.16). Remarkably, pastes P7 and P8 with the low laydown exhibit the highest slip velocities whereas for commercial paste formulations laydown was found to increase with increasing wall slip velocity [26].

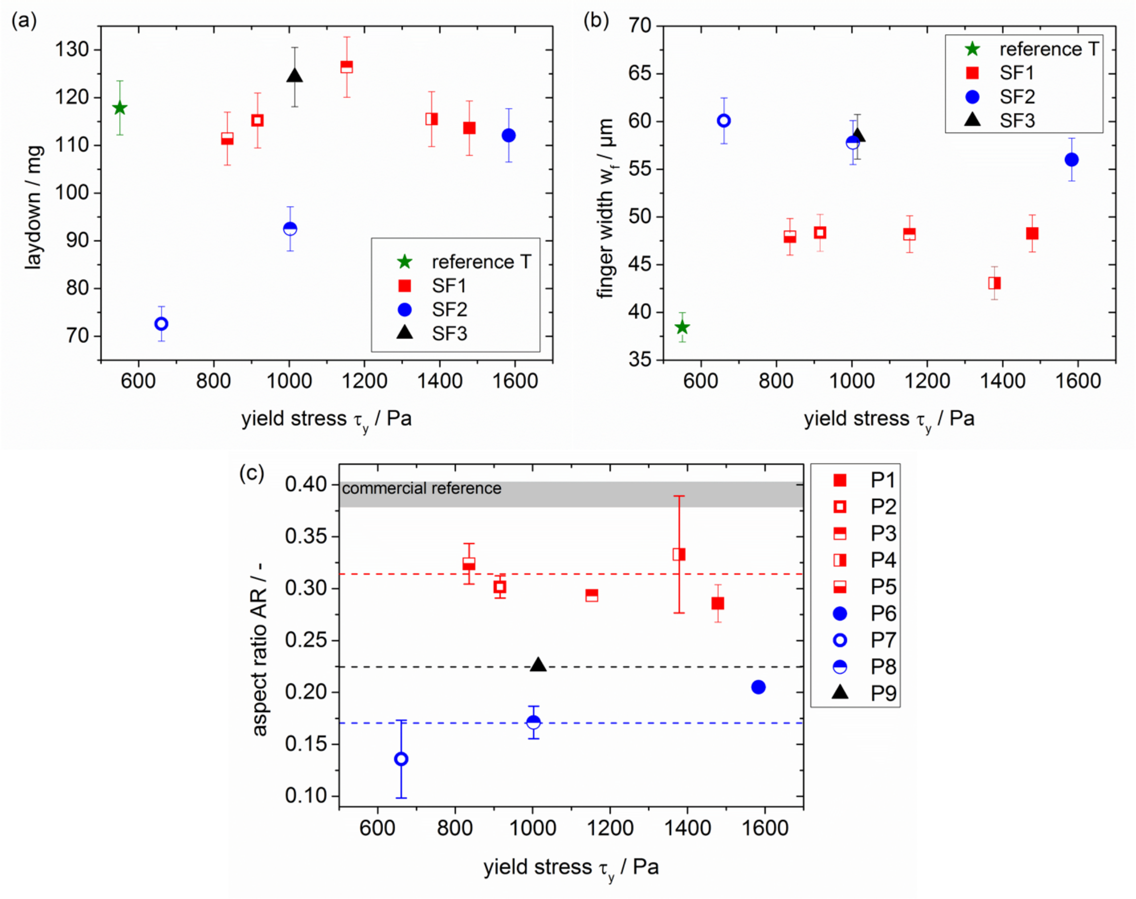

Figure 4.6: (a) Paste laydown versus yield stress for additive-free formulations based on the capillary suspension concept containing SF1, SF2, and SF3. Corresponding results of two trials with commercial paste T are shown for reference. (b) Finger width versus yield stress for electrodes made from additive-free silver paste formulations based on the capillary suspension concept using SF1, SF2, and SF3 as secondary fluid. Data for the commercial reference paste T are also shown. (c) Aspect ratio of electrodes screen-printed through 37 μm mesh opening for additive-free paste compared to commercial reference plotted over the yield stress.

The width of the printed finger lines is shown in Figure 4.6(b). All formulations exhibit substantial paste spreading, w_f values vary between 38 μm and 60 μm for printing tests performed through 37 μm mesh openings. Smallest fingers ($w_f < 40\ \mu m$) are obtained with commercial reference paste T, but additive-free pastes including SF1 are fairly close with $w_f = 43\ \mu m$ - 48 μm. However, pastes made with SF2 and SF3 exhibit much higher finger width in the range $w_f = 55\ \mu m$ - 60 μm. In contrast to earlier findings for commercial pastes [26, 91] neither τ_y (as can be directly seem from Figure 4.6(b)) nor the product ($\tau_y \cdot \eta_{high}$) exhibit a correlation with w_f (graph not shown). Although it needs further investigations to elucidate the different behavior between pastes including SF1 or SF2 and SF3 we can conclude, that additive-free pastes based on the capillary suspension concept can yield similar laydown and finger line width as commercial pastes including polymeric additives, if bulk and secondary fluid are chosen appropriately. Figure 4.6(c) shows the aspect ratio AR as a function of yield stress. As expected from laydown and w_f data the highest aspect ratio is achieved with the commercial paste ($AR > 0.37$), but the AR values for the pastes including SF1 are close (AR = 0.28-0.33). Within experimental error the paste P4 including 9 % SF1 and a 40/60 mixture of ethylene glycol/glycerol exhibits an AR value similar to the commercial paste. AR values for the pastes including SF2 and SF3 are much lower (AR = 0.13-0.23).

Performance of the metallized cells is characterized by the short circuit current density J_{SC}, open circuit voltage V_{OC}, fill factor FF, and cell efficiency η_{eff}. Corresponding data for all pastes are shown in Figure 4.7. As expected from printed finger line morphology, the highest cell efficiency and the best cell performance parameters are achieved for the commercial paste T but the additive-free pastes including SF1 exhibit only 0.1-0.2 % lower cell efficiency η_{eff}. Within experimental uncertainty FF and V_{OC} values of SF1 pastes are similar to those of the commercial paste. The J_{SC} values are related to shading losses, i.e. line width and accordingly the data for the pastes including SF2 and SF3 are particularly low and within the series of SF1 pastes P4 exhibits the highest J_{SC} value consistent with the lowest line width w_f in that series. For most pastes the V_{OC} values are close to that of the reference paste. For paste P6 and P9, V_{OC} is significantly below the reference value, this can be attributed to the wider electrode lines (see Figure 4.6(b)) leading to more damage of surface passivation. The FF for most pastes is also close to the reference value, only pastes P7 and P8 exhibit a clearly lower FF, this is related to the low laydown of these pastes (see Figure 4.6(a)). The cell efficiency η_{eff} is determined by J_{SC}, V_{OC}, and FF. Accordingly the efficiency of pastes including SF2 and SF3 is well below the efficiency of reference paste T, whereas the η_{eff} of pastes made with SF1 are close to the reference value. We obtain almost the same cell efficiency for all pastes including SF1, therefore we can conclude that high shear viscosity, yield stress or wall slip do not affect the printability, respectively the resulting cell performance. All these quantities vary in a wide range within the series of pastes including SF1. On the other hand pastes including SF2 and SF3 exhibit similar rheological properties but printing properties and cell performance are much worse using these pastes. The physical reason for the distinct performance of pastes including SF1 still remains elusive.

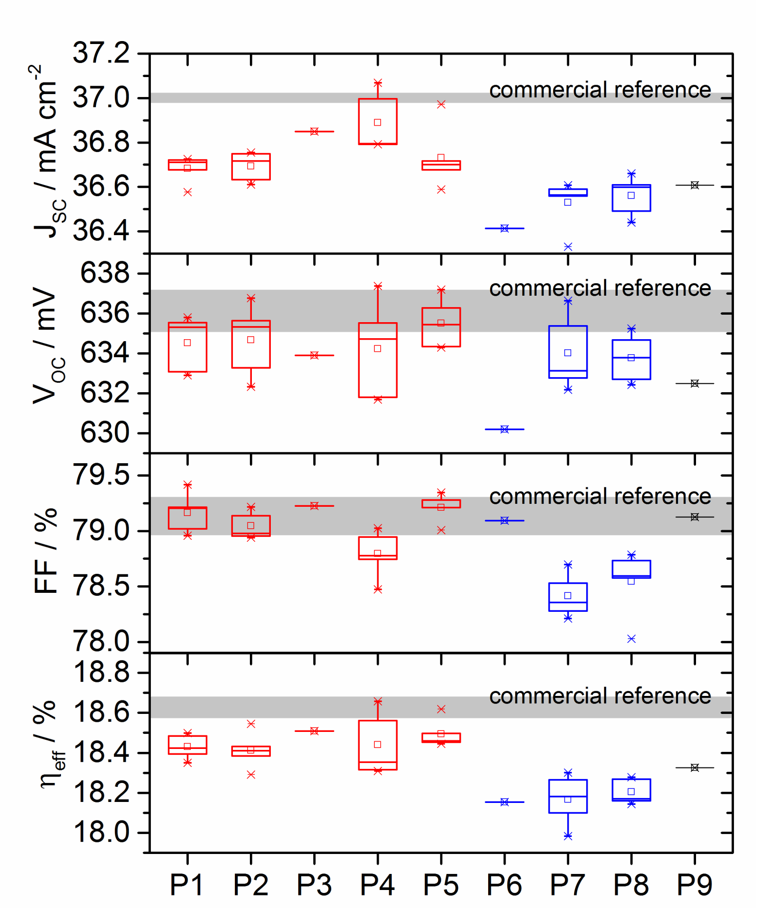

Figure 4.7: Cell performance (short circuit current density J_{SC}, open circuit voltage V_{OC}, fill factor FF, and cell efficiency η_{eff}) determined for additive-free silver paste formulation, P1-P9 (see Table 4.4) and the commercial reference paste T.

4.3.2 Finger line study

For a deeper understanding how the finally sintered finger lines are formed, printed electrodes are investigated for selected pastes P1, P5, and P7 (see Table 4.4) as well as reference paste T right after printing, after drying, and after firing and the changes in AR are summarized in Figure 4.8(a), data always determined at the same position of the fingers. Corresponding 3D laser scanning microscopy images of the printed, dried and fired electrodes illustrating the 3D height profile are shown in Figure 4.8(b). As can be seen from Figure 4.8(a) aspect ratio AR slightly decreases after drying and firing for all pastes due to the removal of the liquid components. This drop is weakest for the commercial paste T and the additive-free pastes including SF1, whereas the decrease in AR is strongest for paste P7 including SF2 with its low AR even right after printing. The corresponding 3D laser scanning microscopy images shown in Figure 4.8(b) clearly show the line interruptions caused by the wires crossing the screen openings. For the commercial paste T, these interruptions seem to heal or level out during drying but appear again after firing. In contrast, for the additive-free pastes P1 and P7 such a levelling of line defects is not observed and the width of the finger line interruptions further increases during the firing step. These line interruptions are more pronounced for the additive-free pastes than for the commercial paste T. This disturbs electrical cell properties and hence the electrical cell performance of the commercial paste T is superior to that of the additive-free pastes.

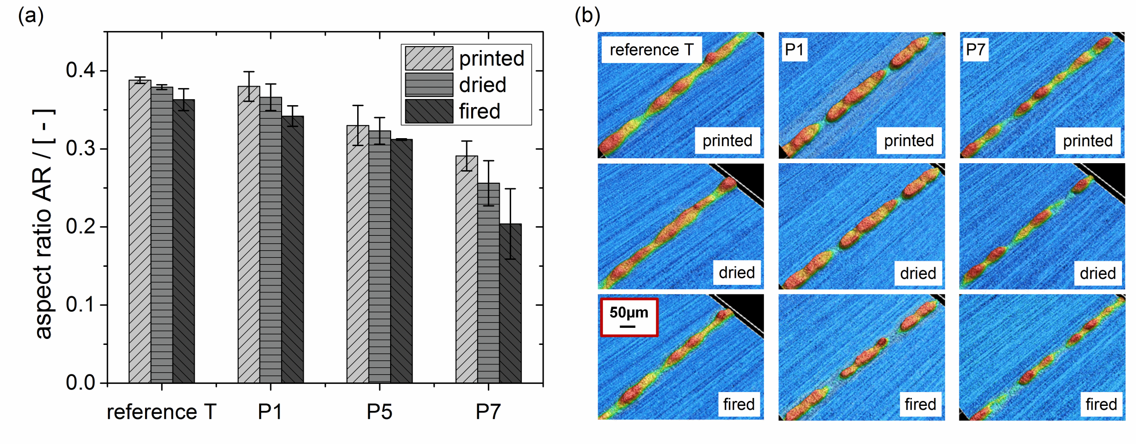

Figure 4.8: (a) *AR* values for pastes P1 (80 *wt*% glycerol in bulk fluid, SF1 used as secondary fluid), P5 (40 *wt*% glycerol, SF1), and P7 (40 *wt*% glycerol, SF2), as well as corresponding data for the commercial paste T. (b) Electrode height profiles of reference T, P1, and P7 right after printing, drying, and sintering. The scale bar in the lower left corner is valid for all height profile images.

4.3.3 High-speed imaging during screen-printing

The printing behavior of capillary suspensions in the screen-printing process is captured with high-speed imaging which is described in detail in a previous work [91]. Printing experiments through 35 μm mesh openings on a glass substrate are done for three pastes made of the same type M Ag particles and same bulk fluid, pure glycerol, but using different secondary fluids SF1, SF2, or SF3 to change the pastes yield stress as summarized in Table 4.5. Changes in yield stress occur due to the variation in interfacial tension between the bulk fluid and the different secondary fluids. Here, in contrast to the previous section, capillary forces are supposed to induce formation of a sample-spanning network in the so-called capillary state (see Table 4.3), i.e. particle clusters form around small droplets of secondary fluid and further assemble into a sample-spanning network. Wall slip behavior is mainly determined by the viscosity of the bulk fluid and the volume fraction of particles. Accordingly, slip behavior is similar for all three pastes investigated here. Since particle loading is low and the viscosity of the bulk fluid (glycerol) is high, absolute v_{slip} (see supplementary, Figure 4.17) values as well as the slope $\partial v_{slip}/\partial\tau$ are small.

Table 4.5: Compositions of pastes used for high-speed imaging experiments. Pastes contain $\phi_{Ag} = 82.0\ wt\%$ ($= 35\ vol\%$) silver particles type M. The bulk fluid used for all pastes is pure glycerol and the secondary fluid content is 5 $vol\%$. Type of secondary fluid is different for pastes P10-P12. These formulations include no glass frit.

label	**secondary liquid type and amount** / $vol\%$	**yield stress** $\boldsymbol{\tau_y}$ / Pa	**slope of wall slip velocity** $\boldsymbol{\partial v_{slip}/\partial\tau}$ / $\mu m/Pas$
P10	SF1 - 5	1153 ± 123	0.9 ± 0.1
P11	SF2 - 5	1451 ± 30	1.1 ± 0.2
P12	SF3 - 5	416 ± 7	0.8 ± 0.1

In Figure 4.9 the change of finger width over the time, as well as corresponding high-speed images are shown for paste P11, similar behavior is found for P10 and P12. A maximum in finger width is observed when the squeegee brings the screen in contact with the glass plate (substrate). The corresponding picture (1) can be identified by the sharp pattern of the screen on the substrate due to the applied squeegee pressure. This point in time is defined as $t = 0\ ms$. At this point, comparatively high stresses occur, pastes yield stress is exceeded, i.e. it becomes liquid like, its pronounced strong shear thinning further facilitates spreading of the paste on the glass substrate underneath the screen. This results in a much wider finger widths than the mesh opening. This spreading phenomenon at the squeegee position is not observed for screen-printing pastes containing additives dissolved in the continuous phase providing flow resistance even at high shear rates [91]. Picture (2) is captured after $t = 20\ ms$, when the squeegee passes the observation field but the screen still clings to the substrate. The paste creeps back towards the mesh opening and the finger width exhibits a minimum at $t = 50\ ms$ (Figure 4.9(b), image 3). This corresponds to the snap-off of the screen. Remarkably, the time of snap-off, or in other words the length of the cling zone, is much shorter than observed earlier for ZnO model pastes including polymers dissolved in the continuous phase of the paste [91]. The pronounced lateral spreading and creep back to the mesh opening is not observed before for commercial pastes and seems to be a characteristic of the additive-free pastes introduced here. Furthermore, high-speed imaging also reveals that a liquid layer with single solid particles remains on the left and right of the printed line after finger width shrinkage. After snap-off, the paste spreads again and finger line gets wider until reaching an equilibrium after about 150 ms (Figure 4.9(b), image 4 and 5).

The finger line width is determined within about 150 ms after the squeegee passage and thus takes significantly (about 50 ms) longer than observed earlier for ZnO model pastes including polymeric binders and thixotropic agents [91]. It should be noted, that the so-called three interval thixotropy test suggested earlier to characterize the thixotropy and spreading behavior of silver pastes [120] is not appropriate for front-side metallization pastes because the finger line width is determined on a time scale not accessible with classical rotational rheometers as pointed out earlier [91]. The time evolution of finger width for pastes P10 and P12 with experimental uncertainty perfectly agrees with the results shown in Figure 4.9 for paste P11. Obviously, the strong variation in yield stress among these pastes does not affect the spreading and receding of the pastes during the printing process. Presumably, high shear viscosity and wall slip which are kept constant here, are more relevant. Resolving this, however, requires further systematic investigations.

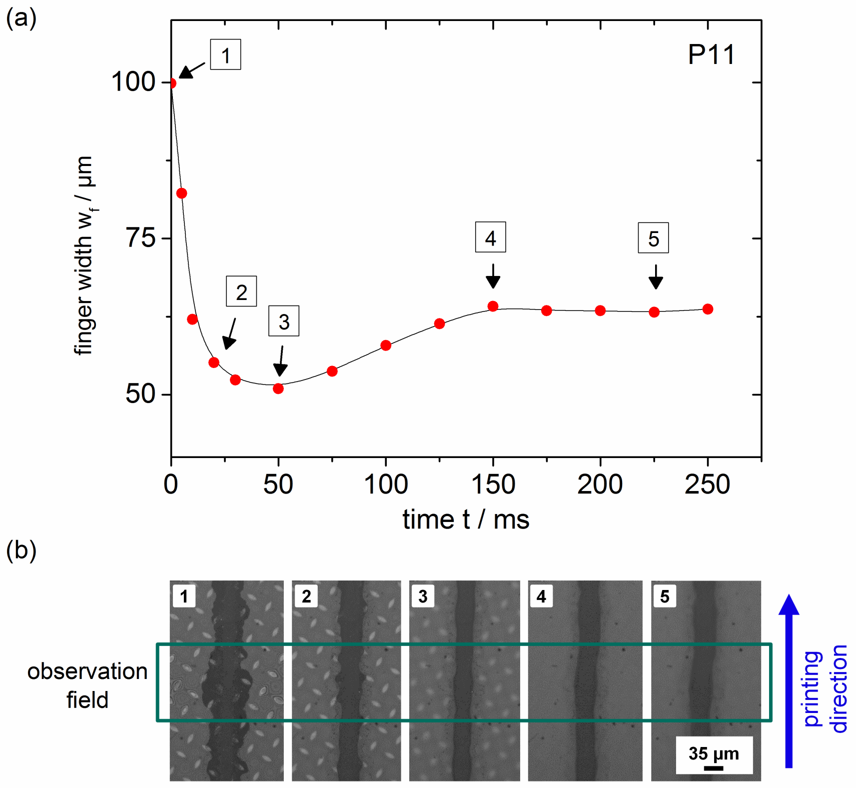

Figure 4.9: (a) Finger width development over time determined from high-speed imaging and (b) corresponding cutouts. These cutouts show the bottom side of the finger line printed on a glass plate through 35 μm mesh opening at 100 mm/s printing speed. Paste P11 (see Table 4.5) is used for these experiments.

4.3.4 Knotless screen printing experiments

Knotless screen is a new screen design especially developed to print fine electrodes ($< 30\ \mu m$). The extent of interruption areas in the finger lines caused by the mesh marks is decreased, as the knotless screen, in contrast to well established standard screens, avoids wire intersections within the mesh openings. The wires of the mesh supporting the patterned emulsion polymer are either parallel or perpendicular to the finger line direction. We prepare three additive-free pastes with different bulk fluid composition (Table 4.6) and perform printing experiments through 27 μm mesh opening. The amount of silver particles (H-type) as well as glass frit (GH-type) and also the secondary fluid SF1 are not changed in these formulations.

Table 4.6: Composition of pastes used for knotless screen printing tests. These pastes are made of H-type silver particles $\phi_{Ag} = 88.8\ wt\%$ ($= 52.1\ vol\%$), GH-type glass frit $\phi_{glassfrit} = 2.64\ wt\%$ ($= 6.2\ vol\%$), and SF1 ($5\ vol\%$) as secondary liquid. Yield stress and the slope of wall slip vs. shear stress of pastes P13-P15 and the commercial reference H are listed. Differences in FOG = 11 ± 2 μm are within experimental error.

label	**bulk fluid composition glycerol content** / $wt\%$	**yield stress** $\boldsymbol{\tau_y}$ / Pa	**slope of wall slip velocity** $\boldsymbol{\partial v_{slip}/\partial \tau}$ / $\mu m/Pas$
P13	80	1514 ± 47	12 ± 1
P14	40	846 ± 36	37 ± 3
P15	20	608 ± 57	72 ± 3
reference H	-	780 ± 8	41 ± 4

The yield stress decreases from P13 to P15, i.e. with decreasing amount of glycerol in the bulk fluid due to the corresponding decrease in interfacial tension (see supplementary, Figure 4.13). Bulk fluid viscosity and hence the high shear viscosity of the respective pastes also strongly decreases with decreasing glycerol content. In contrast, absolute values of wall slip velocity as well as $\partial v_{slip}/\partial \tau$ values increase.

In Figure 4.10(a) we show 3D laser scanning microscopy images, corresponding finger line cross-sections (b), EL spectroscopy images (c), as well as the calculated AR data (d) for printed electrodes made of additive-free pastes P13, P14, and P15 and reference H manufactured with the same Ag and glass frit particles according to a commercial formulation. In knotless screen experiments, finger morphology of the additive-free pastes (Figure 4.10(a)) strongly depends on the bulk fluid, i.e. on yield stress and high shear viscosity, which is not seen in standard screen printing experiments discussed above. A sharp edge and narrow finger width is obtained for

P13 similar to that achieved with reference paste H containing non-volatile additives. Although the edges obtained with paste P13 seem to be formed sharper than for the reference paste H, the aspect ratio AR is slightly higher for the latter and this is presumably due to the lower silver deposit with paste P13 (90 $mg/wafer$ vs. 120 $mg/wafer$ for reference H). However, the electrical cell performance for wafers metallized with paste P13 (data not determined) is expected to be significantly lower than that achieved with the reference paste due to fluctuations in finger height (see Figure 4.10(b)) and potential line interruptions. Corresponding contacting defects are clearly seen in the EL spectroscopy image (see Figure 4.10(c)) of the wafer printed with paste P13. The dark fields between the printed lines indicate poor contacting. In contrast, a bright EL spectroscopy image is obtained for the wafer printed with paste H indicating good interruption-free contacting. All in all, the aspect ratio is higher and the silver laydown is lower in both cases compared to printing through a standard screen with otherwise similar specifications. Printing trials using a standard screen with similar mesh opening (27 μm) resulted in 40 % higher silver deposit for reference paste H as well as the additive-free system P13. Knotless screen technology was introduced to enable reduced silver consumption without loss in cell efficiency [38]. This concept is confirmed here, too.

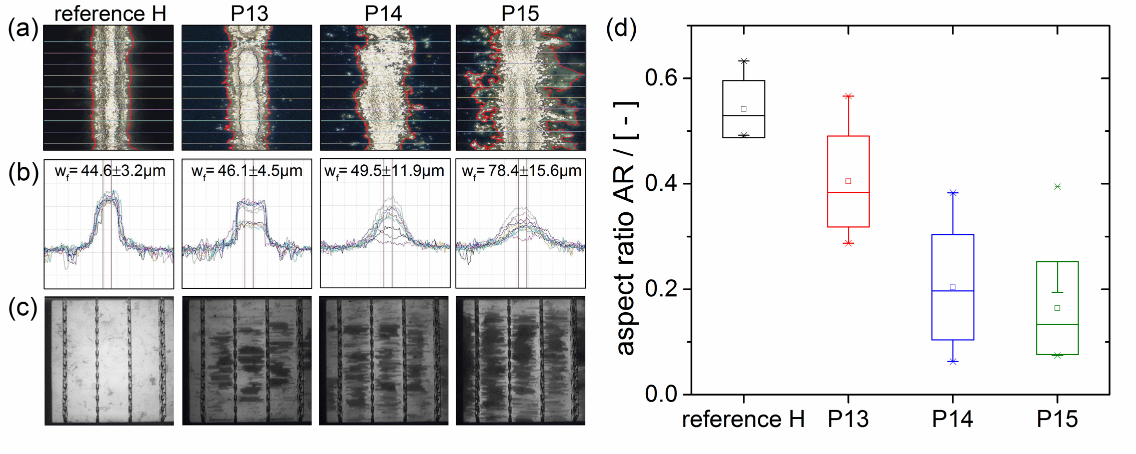

Figure 4.10: Characterization of electrodes made from reference H, P13, P14, and P15 applied with knotless screen through 27 μm mesh opening. (a) Top view of printed electrodes obtained from 3D laser scanning microscopy imaging and finger edge detection. (b) Corresponding finger line cross-sections determined at 10 positions along the printed finger lines with identical spacing in between. (c) EL spectroscopy images representing finger lines with interruption-free contacting (bright areas) and non-contacting due to printing defects like finger line interruptions (dark areas). (d) Corresponding AR data calculated from finger height and finger width data.

The additive-free pastes P14 and P15 show an extended spreading with w_f much larger than the mesh opening and strong fluctuations in line width as well as height. P15 additionally exhibits substantial paste debris, i.e. individual Ag particles are laterally disposed from the printed line. This results in aspect ratios $AR < 0.3$ and many contacting defects as obvious from corresponding data in Figure 4.10(d). These pastes are clearly not suitable for knotless screen printing. The reason for this drastic change in printing behavior is not clear yet. Similar changes in yield stress, high shear viscosity or contact angle between bulk fluid and wafer upon changing glycerol/ethylene glycol mixing ratio are not shown up in standard screen printing trials. Presumably, the higher slip velocity observed for this series of pastes compared to the pastes P1-P9 used for standard screen printing causes this phenomenon. Slip is more pronounced here due to the higher particle loading of the pastes, and for the narrower mesh opening (27 μm) slip contributes stronger to paste transport than in the standard screen printing tests done with 37 μm mesh opening. The relevance of slip phenomena for screen-printing needs further investigation.

4.3.5 Pattern Transfer Printing

Pattern Transfer Printing^{TM}, a contactless printing technology, is applied to print fine silver lines of additive-free paste on the Si-wafer. This paste transfer concept is supposed to yield defect free fine electrodes at a high printing speed [37, 39]. Here we want to elucidate whether our additive-free paste formulation concept is suitable for PTP, too. Pastes are made of Ag particles type T and M forming capillary networks in pendular (P16) and capillary state (P17) (see Table 4.7).

Table 4.7: Paste properties used for PTP tests. Glass frit type GT is used for these pastes and 5 *vol%* SF1 are added as secondary fluid. Fineness of grind is around 11 ± 2 μm.

label	**bulk fluid composition glycerol content**	**silver particle type**	**silver particle content**	**glass frit content** / *wt %*	**yield stress** τ_y / *Pa*	**slope of wall slip velocity** $\partial v_{slip}/\partial \tau$ / $\mu m/Pas$
P16	40 *wt%*	T	87.0 wt% (48 vol%)	2.6	959 ± 111	17.8 ± 2.1
P17	20 *wt%*	M	87.9 wt% (50 vol%)	2.9	1633 ± 11	52.1 ± 3.5

For these experiments we also use different bulk fluid compositions but the same type and amount of secondary fluid (SF1). Glass frit type GT is included in both formulations but the glass frit amount is slightly different. Yield stress, high shear viscosity and the wall slip properties of these pastes are significantly different.

Figure 4.11(a) shows laser scanning images of the printed lines and Figure 4.11(b) displays corresponding geometrical data characterizing finger line morphology. The cross-sectional area A_f, i.e. the silver deposit, is the same for all pastes and apparently all pastes completely detach from the trenched polymer substrate (data not shown here). The customized reference paste PTP exhibits a line width $w_f \sim 20\ \mu m$ and an aspect ratio $AR > 0.6$ closely resembling the geometry of the trenches in the substrate. Obviously, this paste hardly spreads when deposited on the wafer. In contrast, the additive-free paste P17 spreads significantly resulting in a 50 % larger w_f compared to the trench width. Accordingly, $AR \approx 0.4$ is clearly lower than for the reference paste, but still in a technically reasonable range. Spreading is even more pronounced for paste P16 and in addition a lot of debris is visible off the printed lines, consequently $AR \approx 0.2$ is very low.

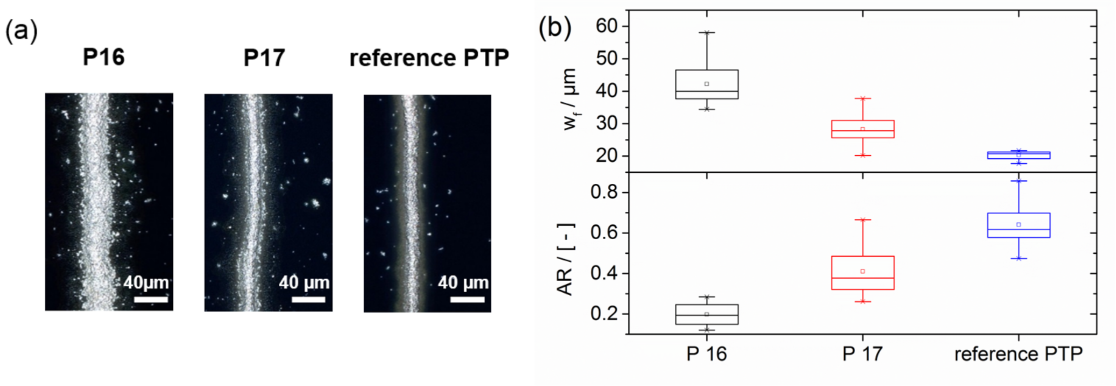

Figure 4.11: (a) 3D laser scanning microscopy image and (b) corresponding finger morphology characterization (w_f and calculated AR) for P16, P17 reference PTP pastes.

Figure 4.12(a) displays data characterizing electrical cell performance, Figure 4.12(b) the resulting line resistance and in Figure 4.12(c) EL spectroscopy images are shown. Cell efficiency and fill factor of the reference paste are far higher than those of the additive-free pastes. The differences in short circuit current J_{SC} reflect the shading losses and directly correlate to the differences in w_f and AR data shown in Figure 4.11(b). The poor electrical performance, especially of paste P17, is mostly due to contacting defects as indicated by the high line resistance R_L and the strong scatter in the measured R_L values especially for P17 (see Figure 4.12(b)). These contacting faults are also visible in the EL spectroscopy images shown in Figure 4.12(c), corresponding dark regions shown up in the lower and left border regions for pastes

P16 and P17, while the image corresponding to the reference paste PTP is essentially defect free. Visual inspection of the metallized wafers after drying reveals that the lines printed with pastes P16 and P17 partly detached from the wafer particularly in the border areas of the wafers. The air flow in the drying oven seems to peel off the fine lines. This seems to be a major challenge for improving the electrical performance of cells metallized with the new additive-free pastes, i.e. adhesion between wafer and printed finger lines has to be improved without addition of non-volatile, polymeric additives.

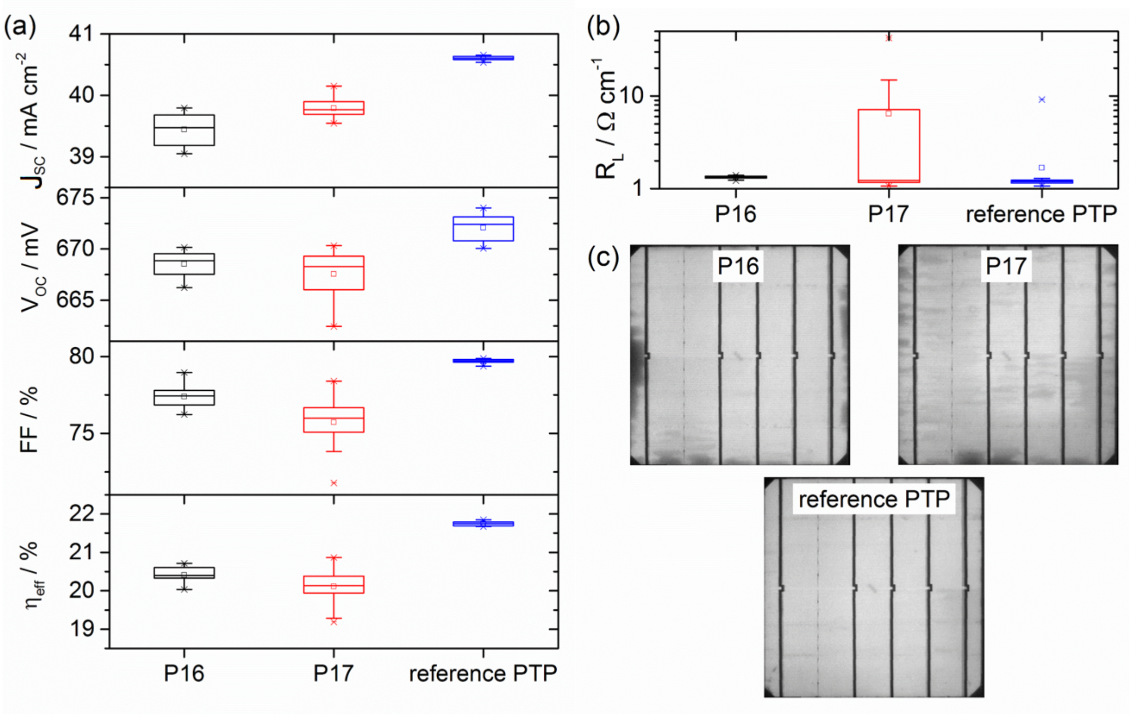

Figure 4.12: (a) Cell performance (J_{SC}, V_{OC}, FF, and η_{eff}) determination, (b) line resistance R_L and (c) EL images obtained for additive-free paste formulation (P16 and P17) compared to commercial reference paste PTP.

4.4 Conclusion

Non-volatile free silver paste formulation based on the so-called capillary suspension concept is a simple, versatile and cost-efficient platform to manufacture highly conductive silver pastes suitable for different printing technologies utilized in front-side metallization of silicon (Si) solar cells. Pastes consist of silver particles, glass frit and two immiscible fluids. Capillary forces induced by the secondary fluid added only in small amounts (< 5 *vol*%) induce the formation of a percolating particle network. This network provides extended shelf-life and distinct flow properties adjustable in a wide range according to the demands of the respective printing process. Pastes have a low degree of agglomeration which is beneficial especially for printing narrow finger lines. The absence of non-volatile binders or thixotropic agents guarantees that the sintered finger lines are free of residual carbon impurities.

Printing tests with standard screen design through 37 μm mesh openings are performed with a series of pastes including the same type and amount of silver particles and glass frit. Composition of bulk fluid (different mixing ratios of ethylene glycol and glycerol) as well as type and amount of secondary fluid is varied in order to cover a broad range of yield stress, high shear viscosity and wall slip velocities. No clear correlation between these flow properties and printing results, i.e. cell performance can be retrieved from these experiments. However, all pastes including SF1 as secondary fluid exhibit printed finger line morphologies and electrical cell performance data close to that of a commercial reference paste including non-volatile additives. The physical reason for this remains elusive. We hypothesize the phenomenon is related to differences in the wetting behavior on the Si-wafer. This will be addressed in future research and our high-speed imaging set-up allowing for a direct imaging of the printing process on transparent model substrates can shed some light on this important application aspect.

The commercial paste exhibits the lowest drop of aspect ratio AR from printing to firing and printed defects (variations of line height) level out during drying. Line interruptions are more pronounced for the additive-free pastes and further increase during firing. This is a major reason for the lower electrical cell performance achieved with the latter pastes compared to the commercial system.

High-speed imaging is used to monitor paste spreading during screen-printing of additive-free pastes on a glass substrate. Pastes exhibit a strong lateral spreading far beyond the mesh opening when the squeegee brings the screen into contact with the substrate. Then the paste creeps back and a minimum line width is observed when the screen snaps off. Subsequently, the paste spreads again to achieve an equilibrium value after about 150 ms. This spreading kinetics is distinctly different from what was reported for ZnO pastes including non-volatile additives [91] and seems to be characteristic for capillary suspension type pastes. Future high-speed imaging studies will help to find appropriate printer settings (e.g. squeegee pressure) to reduce paste spreading, and also to understand how this is affected by paste composition.

Additive-free pastes are also suitable for knotless screen printing and similar as for commercial pastes silver deposit can be reduced and AR can be increased compared to printing with a conventional screen. However, printing results strongly depend on bulk fluid composition (secondary fluid type and amount is kept constant in this series of experiments). Paste spreading and line interruptions strongly increase with decreasing yield stress and high shear viscosity as well as increasing wall slip. Since in this series of experiments particle loading is higher and mesh opening is narrower than in the standard screen printing trials reported above, we hypothesize that particularly slip phenomena may have a dominant effect on printing performance. Laser scanning microscopy of the printed lines as well as EL spectroscopy imaging of sintered wafers reveal that line interruptions and contacting defects are more pronounced for the additive-free pastes than for the commercial reference paste.

Non-volatile free paste formulations are also suitable for PTP. Depending on the paste formulation we obtain almost interruption-free finger widths $w_f \approx 30\ \mu m$ with high AR (≈ 0.5) from PTP technology. Cell performance again suffers from contacting defects which according to visual inspection are caused here by poor adhesion of the deposited lines on the wafer.

Our results demonstrate that the additive-free paste formulation concept based on the capillary suspension phenomenon is applicable in standard screen, knotless screen as well as PTP technologies. With appropriate choice of bulk and secondary fluid, electrode morphologies and cell performance data can be achieved similar to that obtained with commercial silver pastes including non-volatile additives presumably resulting in residual carbon impurities in the sintered electrodes.

However, paste composition has to be further modified and also printing parameters have to be adjusted to decrease paste spreading and line interruptions. Beyond that, also adhesion of printed lines to the wafer has to be improved in order to excel electrical cell performance achieved with state-of-the-art silver pastes, finally reducing the silver consumption needed for harvesting solar energy.

Acknowledgements

The authors would like to thank C. Xu for performing high-speed imaging experiments, O. Süß and K. Tedjokusuma for experimental support especially in contact angle and surface tension measurements. Furthermore, we would like to thank V. Zibat for supporting us with EDX images. C. Yüce gratefully acknowledges financial support by the 100 prozent erneuerbar stiftung. Finally, we acknowledge financial support from the Federal Ministry for Economic Affairs and Energy, Germany (Grant no. 0325775G).

Supplementary

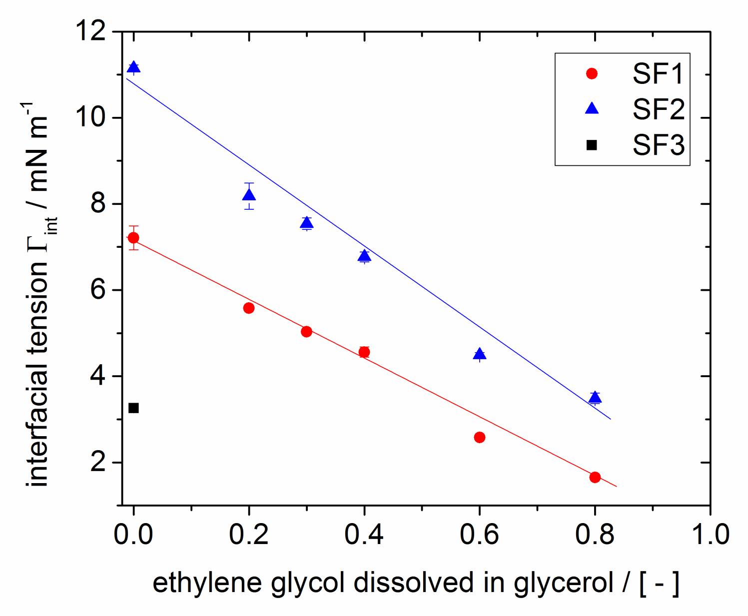

Figure 4.13: Interfacial tension between ethylene glycol/glycerol mixtures and secondary fluids SF1, SF2, as well as SF3, respectively, as determined with the pendant drop method. Lines represent linear fits to the data.

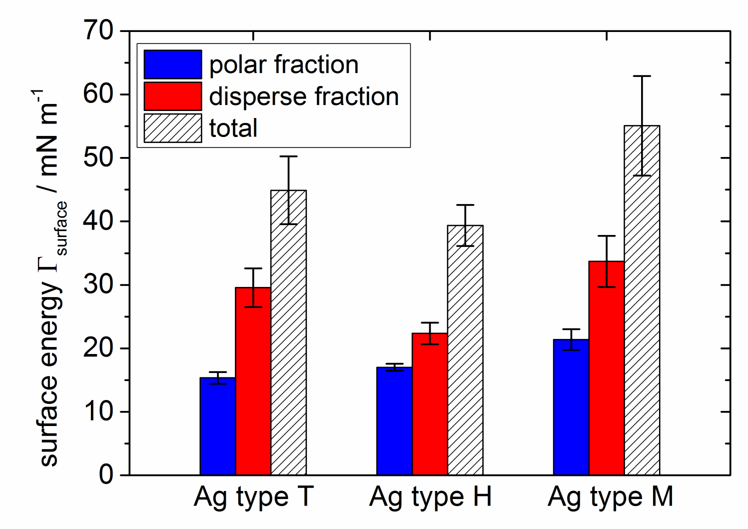

Figure 4.14: Surface energy (total) for Ag type T, H, and M determined with the Owens and Wendt method and additionally separated in their polar and disperse fraction.

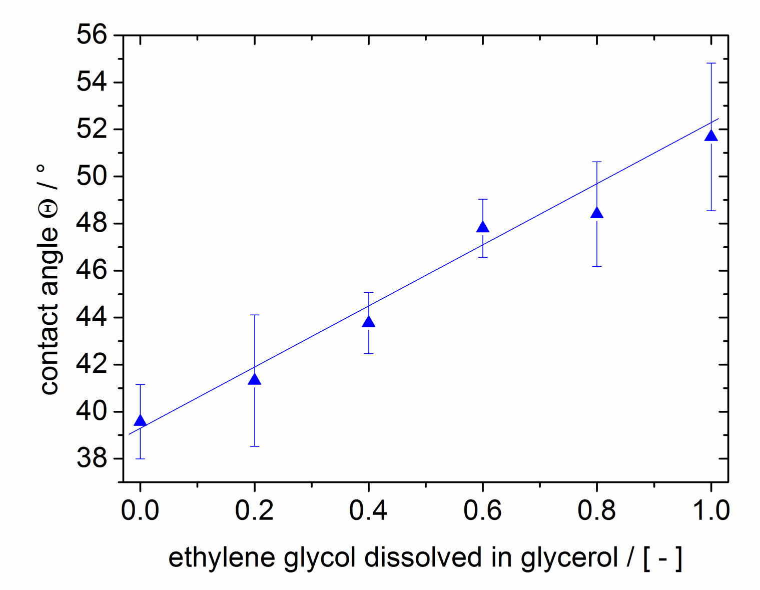

Figure 4.15: Contact angle vs. ethylene glycol fraction for ethylene glycol/glycerol mixtures on a multicrystalline Si-wafer as determined with the sessile drop method. Line represent linear fit to the data.

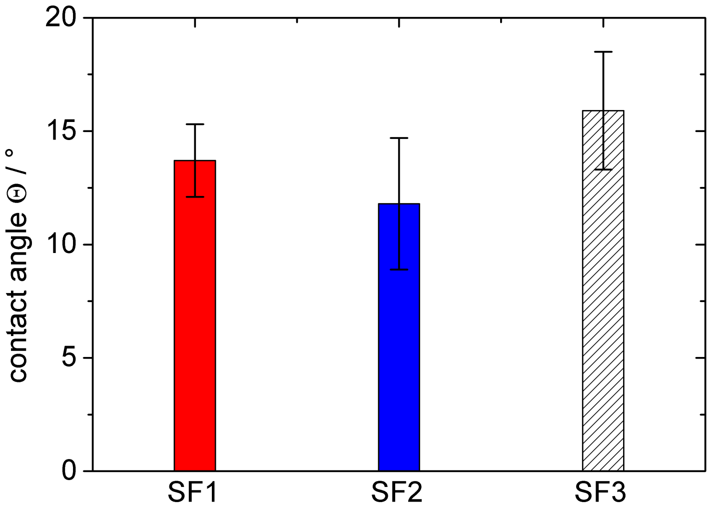

Figure 4.16: Contact angle of SF1, SF2, and SF3 on a multicrystalline Si-wafer as determined with the sessile drop method.

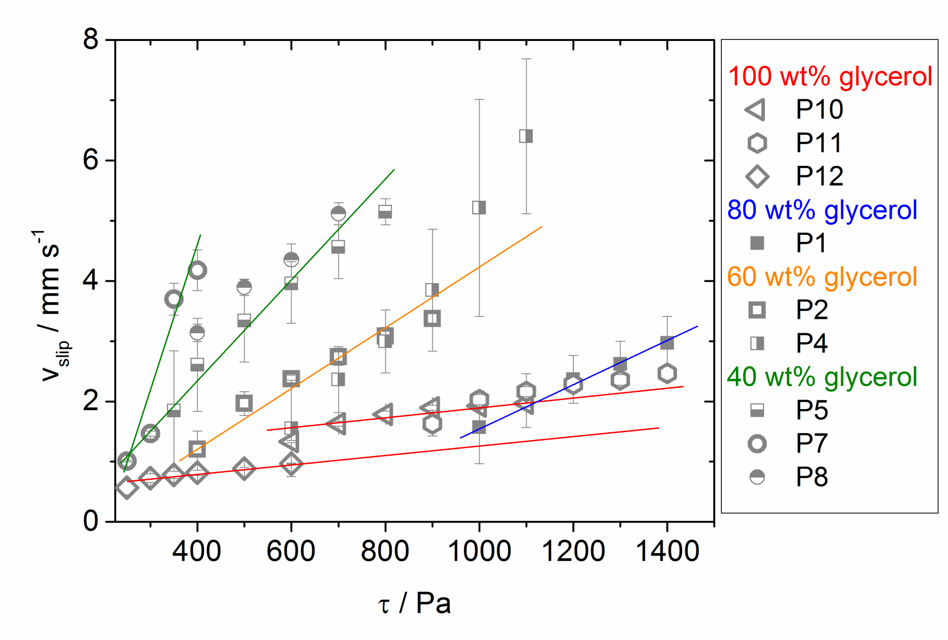

Figure 4.17: Wall slip over shear stress for P1-P12 with different glycerol fraction in the ethylene glycol/glycerol mixtures used as bulk fluids. Lines are to guide the eye.

5. Summary

This dissertation is an experimental work with the focus on the rheological characterization of complex, highly concentrated silver pastes, the correlation of rheological properties and screen-printing behavior as well as the tailored formulation of non-volatile free suspensions based on the capillary suspension concept for the front-side metallization of narrow electrodes printed on Si solar cells. The main results of this cumulative dissertation were divided into three parts.

The application of fine electrodes on a Si-wafer for solar cells is made possible by means of the screen-printing process. The flow behavior of the used silver pastes plays an important role for the printability and the printing result of the electrodes, such as line width and line height. The first part of this work focused on the comprehensive rheological characterization of two commercial screen printing pastes provided by Heraeus Deutschland GmbH & Co. KG showing significant differences in all performed experiments. A detailed measuring protocol is mandatory for a targeted product development meeting the manifold requirements during processing and application of such complex fluids. The investigation included the determination of yield stress, viscosity at low and high shear rates, wall slip velocity, structural recovery after large deformation, and elongation at break as well as tensile force during filament stretching. The importance of video recordings for reliable determination of rheological quantities of highly concentrated suspensions showing wall slip, shear banding, and sample spillover in parallel-plate rotational rheometry is demonstrated. Video recordings enable the determination of the true deformation profile and the flow field at the sample rim using appropriate markers. This protocol contains measurement parameter settings and plate roughness values identified for meaningful rheological characterization. The paste yield stress can be determined either using a vane geometry or plate-plate geometry with appropriate roughness.

Viscosity determination is possible using a plate-plate geometry only with carefully selected plate roughness depending on sample composition. Higher roughness does not necessarily result in lower wall slip. The shear rate or shear stress range in which viscosity determination can be performed is limited by the yield stress and the onset of sample spill. Video recordings further indicate that wall slip, plug flow, and sample spill can be excluded during oscillatory shear tests. Filament stretching tests using a capillary breakup elongational rheometer and a tensile tester can be used to characterize the deformation and breakup behavior of highly filled pastes in elongation.

An in-depth understanding of the relationship between paste composition, rheology and screen-printed line morphology is essential. In chapter 3 the rheological properties of three silver pastes suitable for front-side metallization of Si solar cells, and corresponding vehicles, mainly differing in their thixotropic agent concentration, have been thoroughly investigated. This part elucidates how the substantial changes in paste rheology, determined with the above obtained protocol, show up in the printed finger line morphology. Even a minor increase of thixotropic agent concentration (only 15 %) lead to drastic changes in rheological response, i.e. increase of yield stress, low shear viscosity, and storage modulus in the pastes. Also, the fracture strain in uniaxial extension drops by about one-third. The focus is on the printing tests performed with a layout screen through finger openings between 25 and 50 μm at different printing speeds between 70 and 210 $mm\ s^{-1}$ in order to elucidate how the substantial changes in paste rheology show up in the printed finger line morphology. However, finger width w_f decreases, finger height h_f increases slightly with increasing thixotropic agent concentration, i.e., with increasing yield stress τ_y. Accordingly, the aspect ratio AR exhibits a distinct dependence on τ_y, whereas the cross-sectional area A_f is independent of sample composition consistent with the gravimetric paste transfer determination revealing that paste laydown is independent of thixotropic agent content. The screen-printing process was found to be relatively robust against changes in paste rheology. A twofold increase in τ_y induces a 15-20 % increase in finger line aspect ratio AR without affecting the total laydown. This observed increase in AR should have a significant impact on electrical cell properties due to reduced shading losses obtained from finer line-widths at a given cross-sectional area.

Chapter 4 presents the non-volatile free silver paste formulation. These pastes are stabilized by a percolating particle network induced by the volatile secondary fluid added only in a small amount ($< 5\ vol\%$) providing extended self-life. The distinct flow properties (yield stress and viscosity) are adjusted in a wide range according to the demands of the respective printing process for narrow finger line printing. The absence of non-volatile binders or thixotropic agents guarantees that the sintered finger lines are free of residual carbon impurities. This could result in higher finger line conductivity since the electrical conductivity is not disturbed by these impurities. The developed non-volatile free silver pastes are applied on Cz, respectively mc, Si-wafers using standard screen printing as well as emerging technologies such as knotless screen design and Pattern Transfer Printing^{TM} (PTP) technology. Printing tests with standard screen design through 37 μm mesh openings are performed with a series of pastes including the same type and amount of silver particles and glass frit. Composition of bulk fluid as well as type and amount of secondary fluid is varied in order to cover a broad range of yield stress, high shear viscosity and wall slip velocity. The results reveal no clear correlation between these flow properties and printing results, i.e. cell performance. However, all pastes including a special organic solvent SF1 as secondary fluid exhibit printed finger line morphologies and electrical cell performance data close to that of a commercial reference paste including non-volatile additives. From printing to firing the drop of AR of electrodes with non-volatile free paste formulation are remarkable and line interruptions are more pronounced causing lower electrical cell performance compared to the commercial system. High-speed imaging of paste spreading during screen-printing of additive-free pastes on a glass substrate demonstrates that pastes exhibit a strong lateral spreading far beyond the mesh opening when the squeegee brings the screen into contact with the substrate then the paste retracts and the whole spreading process is completed within 150 ms. Using the knotless screen design the silver deposit can be reduced and AR can be increased compared to printing with a conventional screen for conventional as well as for non-volatile free pastes. Paste spreading and line interruptions strongly increase with decreasing yield stress and high shear viscosity as well as increasing wall slip. Since in this series of experiments particle loading is higher and mesh opening is narrower than in the standard screen printing trials reported above, we hypothesize that particularly slip phenomena may have a dominant effect on printing performance. We hypothesize that particularly slip phenomena may have a dominant effect on printing performance. Depending on the paste formulation we obtain almost interruption-free finger widths $w_f \approx 30\ \mu m$ with high AR (≈ 0.5) from PTP technology. Cell performance again suffers from contacting defects which according to visual inspection are caused here by poor adhesion of the deposited lines on the wafer.

However, paste composition has to be further modified and also printing parameters have to be adjusted to decrease paste spreading and line interruptions. Beyond that, also adhesion of printed lines to the wafer has to be improved in order to excel electrical cell performance achieved with state-of-the-art silver pastes, finally reducing the silver consumption needed for harvesting solar energy.

6. Outlook

Our investigations regarding the development of non-volatile free silver pastes for front-side metallization of Si solar cells demonstrated that the capillary suspension based formulation concept yields pastes with printing properties and cell efficiencies close to that of commercial silver pastes including additional polymeric binders, thickeners or thixotropic agents. However, there is still work to be done and further improvements have to be achieved such that these innovative pastes can serve the growing market of PV installations.

Due to their intrinsically high conductivity these pastes offer advantages in terms of reduced silver consumption and/or higher cell efficiency for potential solar cell manufacturers. This customer benefit has to be proven on an industrial pilot plant scale. Beyond that, the usability of these pastes in innovative, contactless printing methods should be further evaluated and adjusted if required.

The most challenging part is the improvement of the finger morphology, i.e. the finger width and height, respectively AR, have to be further optimized. Paste spreading and line interruptions have to be reduced to minimize shading losses and increase the homogeneity of the electrodes. We assume that reduced spreading behavior of printed electrodes respectively narrower finger widths could be achieved by increasing the bulk fluid viscosity regarding the observations obtained from [91] demonstrating that w_f is proportional to $1/(\tau_y \cdot \eta_{high})$ and the high shear viscosity of the paste is directly proportional to the viscosity of the bulk fluid. Increasing the wall slip of the pastes would result in higher paste laydown on the substrate and improved electrode morphology with lesser finger line interruptions. The next paste generation should be prepared from a newly selected bulk fluid with lower wettability on the substrate to minimize electrode spreading. However, electrode adhesion on the substrate has to be further guaranteed. A study using glass plates with different surface energy could be done to investigate the effect of wetting differences on paste spreading and adhesion.

High-speed imaging of the screen-printing process on transparent substrates is a promising tool to detect the effects of paste formulation and most important, to adjust the printing properties, printing speed, squeegee pressure and snap-off distance for interruption-free electrodes. We started such observations on capillary suspension type silver pastes formulated in the capillary state. This should be continued for pastes with the sample-spanning particle network formation in the pendular state.

The main solvent in the commercial paste formulation is an organic, non-polar solvent. This is beneficial to dissolve binders and additives, being advantageous for paste stability, printability, paste spreading, and the electrode adhesion on the substrate. Such additives should be introduced to capillary suspension type pastes in order to understand how they affect finger line morphology and how a similar electrode quality can be reached without these additives. The adhesion of printed lines to the wafer has to be improved in order to excel electrical cell performance achieved with state-of-the-art silver pastes, finally reducing the silver consumption needed for harvesting solar energy. We started a brief study dissolving either 1 *wt*% polyethylene glycol (PEG from Sigma Aldrich, $M_v \sim 100.000$) in the polar bulk fluid or 1 *wt*% ethyl cellulose (EC from DOW, ETHOCEL^{TM} Standard 10 Industrial Ethyl Cellulose) in the non-polar secondary fluid. Four pastes with varied silver content (84.6 *wt*% and 88.8 *wt*%) and ethylene glycol content (20 *wt*% and 40 *wt*% dissolved in glycerol) as the bulk phase were prepared (see Table 6.1).

Table 6.1: Paste composition S1, S2, S3, and S4 based on capillary suspension concept including 1 *wt*% polyethylene glycol in their bulk phase or ethyl cellulose in their secondary phase. 2.2 *wt*% glass frit type T is used for all formulations.

label	**Ag type T** / *wt*%	**bulk phase composition ethylene glycol/glycerol** / *wt*%	**PEG in bulk phase** / *wt*%	**EC in secondary phase** / *wt*%
S1	84.6	20/80	1	0
S2	88.8	40/60	1	0
S3	84.6	20/80	0	1
S4	88.8	40/60	0	1

The main result of this pretest (see Figure 6.1) is that we can obtain similar cell efficiencies for formulations with around 13.5 *wt*% lower silver laydown on the substrate compared to a commercial formulation. This demonstrates a huge benefit for the cost reduction of Si solar cells. The added polymer in the bulk or secondary fluid is not disturbing the cell efficiency for capillary paste formulation with reduced silver content. For a paste with around 88.8 $wt\%$ Ag content, which is comparable with the Ag amount used in conventional silver pastes, cell efficiencies are decreased due to the addition of additives. This should be pursued further in future work.

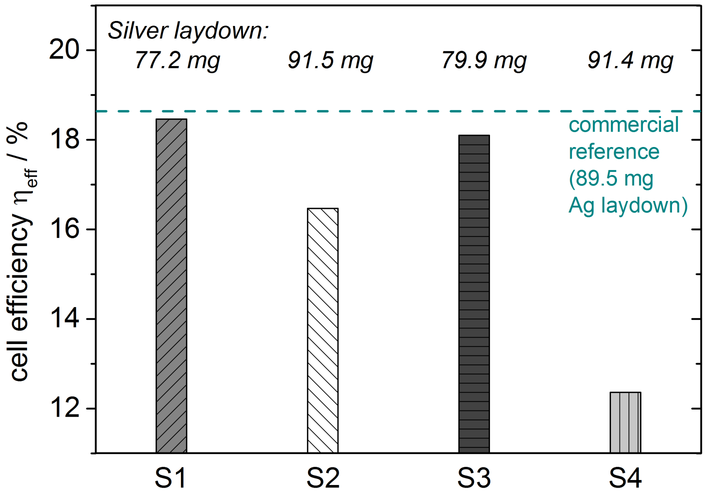

Figure 6.1: Cell efficiency performance of multicrystalline Si solar cells printed with four pastes based on the capillary suspension concept (S1, S2, S3, and S4). Metallization was done at pastes include 84.6 $wt\%$ (S1 and S3) and 88.8 $wt\%$ (S2 and S4) silver particles. The bulk fluid is a 20/80 mixture (S1 and S3) and a 40/60 mixture of ethylene glycol/glycerol (S2 and S4), respectively. In all pastes 5 $vol\%$ SF1 is added as secondary fluid. Additionally, pastes S1 and S2 include 1 $wt\%$ polyethyleneglycol (Sigma Aldrich, $M_v \sim 100.000$) dissolved in the bulk phase, whereas pastes S3 and S4 include 1 $wt\%$ ethyl cellulose (DOW, ETHOCEL^{TM} Standard 10 Industrial Ethyl Cellulose) dissolved in the secondary fluid (see Table 6.1). Cell efficiency results and resulting silver laydown after firing are compared with a commercial paste as reference.

In the longer term, further product lines for other applications of printed electronics beyond PV technology are to be developed. The application potential of our formulation concept for printable electronics sintered at low temperatures should also be assessed. In these applications, conductive structures are produced that contain large amounts of organic components in the printed, dried or low-temperature sintered structure in order to achieve sufficient cohesion. This has already been demonstrated for thermal conductivity using the example of epoxy resin/silver mixtures [126]. The developed paste concept based on the so-called capillary suspensions opens up new technical possibilities to obtain polymer/silver composites with high conductivity at low silver consumption.

7. Appendix

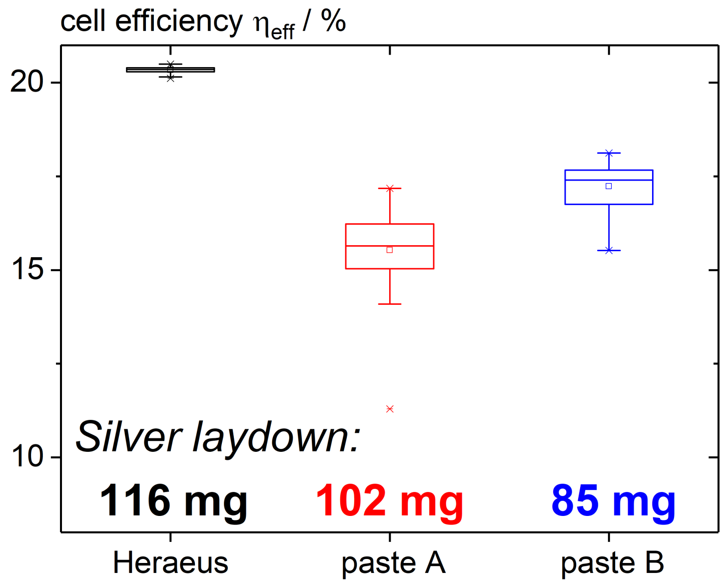

Figure 7.1: Comparison of cell efficiency results for commercially manufactured paste Heraeus, and two silver pastes based on capillary suspension concept, termed as paste A and paste B. Cells were printed through 50 μm mesh openings on monocrystalline Si-wafers and were fired at peak temperature T_{peak} = 860 °C. Paste laydown and cell efficiency differ substantially. Non-volatile free paste B provides a reasonable cell efficiency at significantly lower silver consumption compared to the commercial reference paste.

Bibliography

[1] "Connecting the sun - Solar Photovoltaics on the Road To Large-Scale Grid Integration," tech. rep., 2012.

[2] J. Wilkes, C. Kjaer, and R. Gruet, *Pure power-wind energy targets for 2020 and 2030.* European Wind Energy Association, 2011.

[3] European Wind Energy Association, "WindEurope Annual Statistics 2016," tech. rep., 2017.

[4] E. Ralph, "Recent advancements in low cost solar cell processing," in *11th Photovoltaic Specialists Conference*, vol. 1, p. 315, 1975.

[5] M. B. Field and L. R. Scudder, "Application of thick-film technology to solar cell fabrication," in *12th Photovoltaic Specialists Conference*, pp. 303–308, 1976.

[6] "International technology roadmap for photovoltaic (ITRPV). Results 2017 including maturity report 2018," 2018.

[7] A. Eshkeiti, A. S. G. Reddy, S. Emamian, B. B. Narakathu, M. Joyce, M. Joyce, P. D. Fleming, B. J. Bazuin, and M. Z. Atashbar, "Screen printing of multilayered hybrid printed circuit boards on different substrates," *IEEE Transactions on Components, Packaging and Manufacturing Technology*, vol. 5, no. 3, pp. 415–421, 2015.

[8] A. E. Ostfeld, I. Deckman, A. M. Gaikwad, C. M. Lochner, and A. C. Arias, "Screen printed passive components for flexible power electronics," *Scientific reports*, no. 5:15959, pp. 1–11, 2015.

[9] J.-h. Kim, J. Kim, G. J. Lee, J. Jeong, and C. Byeongdae, "Screen-printed Cu source/drain electrodes for a- InGaZnO thin-film transistors," *Molecular Crystals and Liquid Crystals*, vol. 586, pp. 161–167, 2013.

[10] S. K. Tam, K. Y. Fung, and K. M. Ng, "Copper pastes using bimodal particles for flexible printed electronics," *Journal of Material Science*, vol. 51, no. 4, pp. 1914–1922, 2016.

[11] D. Schwanke, J. Pohlner, A. Wonisch, T. Kraft, and J. Geng, "Enhancement of fine line print resolution due to coating of screen fabrics," *Journal of Microelectronics and Electronic Packaging*, vol. 6, no. 1, pp. 13–19, 2009.

[12] R. Faddoul, N. Reverdy-Bruas, and A. Blayo, "Formulation and screen printing of water based conductive flake silver pastes onto green ceramic tapes for electronic applications," *Materials Science and Engineering B: Solid-State Materials for Advanced Technology*, vol. 177, no. 13, pp. 1053–1066, 2012.

[13] P. Kumar, M. Pfeffer, B. Willsch, O. Eibl, L. J. Koduvelikulathu, V. D. Mihailetchi, and R. Kopecek, "N-type single-crystalline Si solar cells: Front side metallization for solar cells reaching 20% efficiency," *Solar Energy Materials and Solar Cells*, vol. 157, pp. 200–208, 2016.

[14] N. Wehmeier, A. Nowack, B. Lim, T. Brendemühl, S. Kajari-schröder, J. Schmidt, R. Brendel, and T. Dullweber, "21.0%-efficient screen-printed n-PERT back-junction silicon solar cell with plasma-deposited boron diffusion source," *Solar Energy Materials and Solar Cells*, vol. 158, pp. 50–54, 2016.

[15] N. S. Lewis, "Toward cost-effective solar energy use," *Science*, vol. 315, no. February, pp. 798–801, 2007.

[16] M. Ju, Y. J. Lee, J. Lee, B. Kim, K. Ryu, K. Choi, K. Song, K. Lee, C. Han, Y. Jo, and J. Yi, "Double screen printed metallization of crystalline silicon solar cells as low as 30 μm metal line width for mass production," *Solar Energy Materials and Solar Cells*, vol. 100, pp. 204–208, 2012.

[17] M. Aoki, K. Nakamura, T. Tachibana, I. Sumita, H. Hayashi, H. Asada, and Y. Ohshita, "30 micron fine-line printing for solar cells," in *Photovoltaic Specialists Conference (PVSC), 2013 IEEE 39th*, pp. 2162–2166, 2013.

[18] J. Hoornstra, A. W. Weeber, H. H. C. de Moor, and W. C. Sinke, "The importance of paste rheology in improving fine line, thick film screen printing of front side metallization," *Netherlands Energy Research Foundation ECN*, 1997.

[19] J. R. Larry, R. M. Rosenberg, and R. Uhler, "Thick-film technology: An introduction to the materials," *IEEE Transactions on components, hybrids, and manufacturing technology*, vol. 3, no. 2, pp. 211–225, 1980.

[20] H. Reichl, *Hybridintegration: Technologie und Entwurf von Dickschichtschaltungen.* Hüthig Verlag, 1986.

[21] D. E. Riemer, "The theoretical fundamentals of the screen printing process," *Microelectronics International*, vol. 6, no. 1, pp. 8–17, 1989.

[22] R. Durairaj, S. Mallik, A. Seman, and N. N. Ekere, "Investigation of wall-slip effect on lead-free solder paste and isotropic conductive adhesives," *Sadhana*, vol. 34, no. 5, pp. 799–810, 2009.

[23] R. Durairaj, L. W. Man, N. N. Ekere, and S. Mallik, "The effect of wall-slip formation on the rheological behaviour of lead-free solder pastes," *Materials and Design*, vol. 31, pp. 1056–1062, 2010.

[24] C. P. Hsu, R. H. Guo, C. C. Hua, C.-L. Shih, W.-T. Chen, and T.-I. Chang, "Effect of polymer binders in screen printing technique of silver pastes," *Journal of polymer research*, vol. 20, no. 10, pp. 1–8, 2013.

[25] S. Thibert, J. Jourdan, B. Bechevet, D. Chaussy, N. Reverdy-Bruas, and D. Beneventi, "Influence of silver paste rheology and screen parameters on the front side metallization of silicon solar cell," *Materials Science in Semiconductor Processing*, vol. 27, pp. 790–799, 2014.

[26] C. Xu, M. Fies, and N. Willenbacher, "Impact of wall slip on screen printing of front-side silver pastes for silicon solar cells," *IEEE Journal of Photovoltaics*, vol. 7, no. 1, pp. 129–135, 2017.

[27] Y. Zhou, H. Tong, Y. Liu, S. Yuan, X. Yuan, C. Liu, Y. Zhang, G. Chen, and Y. Yang, "Rheological effect on screen-printed morphology of thick film silver paste metallization," *Journal of Materials Science: Materials in Electronics*, vol. 28, no. 7, pp. 5548–5553, 2017.

[28] M. Schneider, E. Koos, and N. Willenbacher, "Highly conductive, printable pastes from capillary suspensions," *Scientific Reports*, vol. 6, no. August, pp. 1–10, 2016.

[29] E. Koos and N. Willenbacher, "Capillary forces in suspension rheology," *Science*, vol. 331, pp. 897–900, 2011.

[30] E. Koos and N. Willenbacher, "Particle configurations and gelation in capillary suspensions," *Soft Matter*, vol. 8, no. 14, pp. 3988–3994, 2012.

[31] E. Koos, J. Johannsmeier, L. Schwebler, and N. Willenbacher, "Tuning suspension rheology using capillary forces," *Soft Matter*, vol. 8, no. 24, pp. 6620–6628, 2012.

[32] I. B. Cooper, R. Stephenson, and P. Ferraro, "Polyalkylene carbonate binders for cleaner burning thick film Ag paste: Comparison to commercially available Ag pastes," in *Photovoltaic Specialist Conference, (PVSC), 2016 IEEE 43th*, pp. 2882–2884, 2016.

[33] S. K. Chunduri and M. Schmela, "Market survey screen printers 2018," *Taiyangnews*, 2018.

[34] M. Pospischil, M. Klawitter, M. Kuchler, M. Jahn, R. Efinger, R. Schwarz, L. Wende, M. König, F. Clement, and D. Biro, "High speed dispensing with novel 6inch print head," *Energy Procedia*, vol. 98, pp. 61–65, 2016.

[35] N. Mathews, Y. M. Lam, S. G. Mhaisalkar, and A. C. Grimsdale, "Printing materials for electronic devices," *International Journal of Materials Research*, vol. 101, no. 2, pp. 236–250, 2010.

[36] A. Lorenz, A. Kalio, G. T. Hofmeister, S. Nold, L. Friedrich, A. Kraft, J. Bartsch, D. Wolf, M. Dreher, F. Clement, and D. Biro, "Flexographic printing - high troughput technology for fine line seed layer printing on silicon solar cells," in *28th European Photovoltaic Solar Energy Conference and Exhibition*, pp. 1017–1023, 2013.

[37] J. Lossen, M. Matusovsky, A. Noy, C. Maier, and M. Bähr, "Pattern transfer printing (PTP) for c-Si solar cell metallization," *Energy Procedia*, vol. 67, pp. 156–162, 2015.

[38] A. Lorenz, M. Linse, H. Frintrup, M. Jeitler, A. Mette, M. Lehner, R. Greutmann, H. Brocker, M. König, D. Erath, and F. Clement, "Screen printed thick film metallization of silicon solar cells - recent developments and future perspectives," in *35th European Photovoltaic Solar Energy Conference and Exhibition*, pp. 819–824, 35th European Photovoltaic Solar Energy Conference and Exhibition, 2018.

[39] A. Adrian, D. Rudolph, J. Lossen, M. Matusovsky, and V. Chandrasekaran, "Benefits of pattern transfer printing method for finger metallization on silicon solar cells," in *35th European Photovoltaic Solar Energy Conference and Exhibition*, pp. 434–438, 35th European Photovoltaic Solar Energy Conference and Exhibition, 2018.

[40] M. A. Green, "Solar cells: operating principles, technology, and system applications," *Englewood Cliffs, NJ, Prentice-Hall, Inc.*, p. 288 p., 1982.

[41] D. Erath, A. Filipović, M. Retzlaff, A. K. Goetz, F. Clement, D. Biro, and R. Preu, "Advanced screen printing technique for high definition front side

metallization of crystalline silicon solar cells," *Solar Energy Materials and Solar Cells*, vol. 94, no. 1, pp. 57–61, 2010.

[42] S. Braun, G. Hahn, R. Nissler, C. Pönisch, and D. Habermann, "Multi-busbar solar cells and modules: High efficiencies and low silver consumption," *Energy Procedia*, vol. 38, pp. 334–339, 2013.

[43] H. Hannebauer, T. Dullweber, U. Baumann, T. Falcon, and R. Brendel, "21.2%-efficient fineline-printed PERC solar cell with 5 busbar front grid," *Physica Status Solidi - Rapid Research Letters*, vol. 8, no. 8, pp. 675–679, 2014.

[44] D. L. Meier, V. Chandrasekaran, A. Gupta, V. Yelundur, and A. Rohatgi, "Silver contact grid: Inferred contact resistivity and cost minimization in 19% silicon solar cells," *IEEE Journal of Photovoltaics*, vol. 3, no. 1, pp. 199–205, 2013.

[45] T. Dullweber, S. Gatz, H. Hannebauer, T. Falcon, R. Hesse, J. Schmidt, and R. Brendel, "Towards 20% efficient large-area screen-printed rear-passivated silicon solar cells," *Progress in Photovoltaics: Research and Applications*, vol. 20, no. 6, pp. 630–638, 2012.

[46] A. J. McEvoy, L. Castaner, and T. Markvart, *Solar cells: materials, manufacture and operation.* Academic Pres, 2012.

[47] "EKRA Screen Printing Technologies - HYCON XH STS," 2019.

[48] Y. Zhang, L. Zhang, L. Jiang, L. Song, C. Guo, V. Dua, H. Yang, E. Kim, and C. Chen, "Knotless screen printing for crystalline silicon solar cells," in *7th Workshop on Metallization Konstanz*, 2017.

[49] S. B. Rane, T. Seth, G. J. Phatak, D. P. Amalnerkar, and B. K. Das, "Influence of surfactants treatment on silver powder and its thick films," *Materials Letters*, vol. 57, no. 20, pp. 3096–3100, 2003.

[50] S. B. Rane, P. K. Khanna, T. Seth, G. J. Phatak, D. P. Amalnerkar, and B. K. Das, "Firing and processing effects on microstructure of fritted silver thick film electrode materials for solar cells," *Materials Chemistry and Physics*, vol. 82, no. 1, pp. 237–245, 2003.

[51] R. Faddoul, N. Reverdy-Bruas, and J. Bourel, "Silver content effect on rheological and electrical properties of silver pastes," *Journal of Materials Science: Materials in Electronics*, vol. 23, no. 7, pp. 1415–1426, 2012.

[52] J. F. Nijs, J. Szlufcik, J. Poortmans, S. Sivoththaman, and R. P. Mertens, "Advanced manufacturing concepts for crystalline silicon solar cells," *IEEE Transactions on Electron Devices*, vol. 46, no. 10, pp. 1948–1969, 1999.

[53] R. Gomatam and K. L. Mittal, *Electrically Conductive Adhesive.* CRC Press, 2008.

[54] J. Qin, W. Zhang, Z. Liu, and S. Bai, "Effects of polymer binder on rheological properties of silver pastes for screen printing front electrode films of solar cells," *International Journal of Modern Physics B*, vol. 29, no. 10 & 11, pp. 1–9, 2015.

[55] J. Qin, S. Bai, W. Zhang, Z. Liu, and H. Wang, "Effects of organic medium on rheological properties of silver pastes for crystalline silicon solar cells," *Circuit World*, vol. 42, no. 2, pp. 77–83, 2016.

[56] J.-S. Jiang, J.-E. Liang, H.-L. Yi, S.-H. Chen, and C.-C. Hua, "Rheological fingerprints of time-evolving polymer-particle interaction and sol-gel transition in silver pastes," *Journal of Polymer Research*, vol. 22, no. 8, pp. 1–11, 2015.

[57] C. Ballif, D. M. Huljić, G. Willeke, and A. Hessler-Wyser, "Silver thick-film contacts on highly doped n-type silicon emitters: Structural and electronic properties of the interface," *Applied Physics Letters*, vol. 82, no. 12, pp. 1877–1880, 2003.

[58] Y. C. Shih, Y. H. Lin, J. P. You, and F. G. Shi, "Screen-printable silver pastes with nanosized glass frits for silicon solar cells," *Journal of Electronic Materials*, vol. 42, no. 3, pp. 410–416, 2013.

[59] G. C. Cheek, R. P. Mertens, R. van Overstraeten, and L. Frisson, "Thick-film metallization for solar cell applications," *IEEE Transactions on Electron Devices*, vol. 31, no. 5, pp. 602–609, 1984.

[60] L. Wang, C. Guo, R. M. Cosimano, and W. Zhang, "Conductive thick film paste for solar cell contacts," 2013.

[61] S. E. Habas, H. A. S. Platt, M. F. A. M. V. Hest, and D. S. Ginley, "Low-cost inorganic solar cells : from ink to printed device," *Chemical Reviews*, vol. 110, pp. 6571–6594, 2010.

[62] L. Song, C. Chen, T. Guo, and W. Zhang, "Organic vehicle for electroconductive paste," 2013.

[63] W. J. Borland and J. D. Summers, "Conductive paste for fine-line high-aspect-ratio screen printing in the manufacture of semiconductor devices," 2013.

[64] J. D. Fields, M. I. Ahmad, V. L. Pool, J. Yu, D. G. Van Campen, P. A. Parilla, M. F. Toney, and M. F. Van Hest, "The formation mechanism for printed silver-contacts for silicon solar cells," *Nature Communications*, vol. 7, pp. 1–7, 2016.

[65] F. Bossler and E. Koos, "Structure of particle networks in capillary suspensions with wetting and nonwetting fluids," *Langmuir*, vol. 32, no. 6, pp. 1489–1501, 2016.

[66] E. Koos, W. Kannowade, and N. Willenbacher, "Restructuring and aging in a capillary suspension," *Rheologica Acta*, vol. 53, no. 12, pp. 947–957, 2014.

[67] F. Bossler, J. Maurath, K. Dyhr, N. Willenbacher, and E. Koos, "Fractal approaches to characterize the structure of capillary suspensions using rheology and confocal microscopy," *Journal of Rheology*, vol. 62, no. 1, pp. 183–196, 2018.

[68] J. Dittmann and N. Willenbacher, "Micro structural investigations and mechanical properties of macro porous ceramic materials from capillary suspensions," *Journal of the American Ceramic Society*, vol. 97, no. 12, pp. 3787–3792, 2014.

[69] T. Domenech and S. S. Velankar, "On the rheology of pendular gels and morphological developments in paste-like ternary systems based on capillary attraction," *Soft Matter*, vol. 11, no. 8, pp. 1500–1516, 2015.

[70] J. Dittmann, E. Koos, and N. Willenbacher, "Ceramic capillary suspensions: Novel processing route for macroporous ceramic materials," *Journal of the American Ceramic Society*, vol. 96, no. 2, pp. 391–397, 2013.

[71] M. Pospischil, K. Zengerle, J. Specht, G. Birkle, P. Koltay, R. Zengerle, A. Henning, M. Neidert, C. Mohr, F. Clement, and D. Biro, "Investigations of thick-film-paste rheology for dispensing applications," *Energy Procedia*, vol. 8, pp. 449–454, 2011.

[72] M. Pospischil, M. Kuchler, M. Klawitter, C. Rodríguez, M. Padilla, R. Efinger, M. Linse, A. Padilla, H. Gentischer, M. König, M. Hörteis, L. Wende, O. Doll, R. Zengerle, F. Clement, and D. Biro, "Dispensing technology on the route to an industrial metallization process," *Energy Procedia*, vol. 67, pp. 138–146, 2015.

[73] K. Gilleo, "Rheology and surface chemistry for screen printing," *Screen Printing Magazine*, pp. 128–132, 1989.

[74] H. W. Lin, C. P. Chang, W. H. Hwu, and M. D. Ger, "The rheological behaviors of screen-printing pastes," *Journal of Materials Processing Technology*, vol. 197, no. 1-3, pp. 284–291, 2008.

[75] L. Shiyong, W. Ning, X. Wencai, and L. Yong, "Preparation and rheological behavior of lead free silver conducting paste," *Materials Chemistry and Physics*, vol. 111, no. 1, pp. 20–23, 2008.

[76] S. Thibert, J. Jourdan, B. Bechevet, S. Mialon, D. Chaussy, N. Reverdy-Bruas, and D. Beneventi, "Study of the high throughput flexographic process for silicon solar cell metallisation," *Progress in Photovoltaics: Research and Applications*, vol. 24, no. 2, pp. 240–252, 2016.

[77] S. W. Glunz, A. Mette, P. L. Richter, A. Filipovic, and G. Willeke, "New concepts for the front side metallization of silicon solar cells," *21st European Photovoltaic Solar Energy Conference*, vol. 1, no. September, pp. 4–7, 2006.

[78] P. Coussot, *Rheometry of pastes , suspensions , and granular materials: Application in Industry and Environment.* Wiley-interscience, 2005.

[79] P. Coussot, "Rheophysics of pastes: a review of microscopic modelling approaches," *Soft Matter*, vol. 3, no. 5, p. 528, 2007.

[80] H. Zhou, J. Hong, L. Piao, and S.-H. Kim, "Dual rheological responses in Ag pastes," *Journal of Applied Polymer Science*, vol. 129, no. 3, pp. 1328–1333, 2013.

[81] R. Buscall, "The rheology of concentrated dispersions of weakly attracting colloidal particles with and without wall slip," *Journal of Rheology*, vol. 37, no. 4, p. 621, 1993.

[82] D. M. Kalyon, "Rheological behavior of a concentrated suspension: A solid rocket fuel simulant," *Journal of Rheology*, vol. 37, no. 1, pp. 35–53, 1993.

[83] U. Yilmazer and D. M. Kalyon, "Slip effects in capillary and parallel disk torsional flows of highly filled suspensions," *Journal of Rheology*, vol. 33, no. 8, pp. 1197–1212, 1989.

[84] B. K. Aral and D. M. Kalyon, "Effects of temperature and surface roughness on time-dependent development of wall slip in steady torsional flow of concentrated suspensions," *Journal of Rheology (1978-present)*, vol. 38, no. 4, pp. 957–972, 1994.

[85] J. Persello, A. Magnin, J. Chang, J. M. Piau, and B. Cabane, “Flow of colloidal aqueous silica dispersions,” *Journal of Rheology*, vol. 38, no. 6, pp. 1845–1870, 1994.

[86] F. Pignon, A. Magnin, and J. M. Piau, “Thixotropic colloidal suspensions and flow curves with minimum : Identification of flow regimes and rheometric consequences,” *Journal of Rheology*, vol. 40, no. 4, pp. 573–587, 1996.

[87] S. P. Meeker, R. T. Bonnecaze, and M. Cloitre, “Slip and flow in pastes of soft particles: Direct observation and rheology,” *Journal of Rheology*, vol. 48, no. 6, pp. 1295–1320, 2004.

[88] J. R. Seth, M. Cloitre, R. T. Bonnecaze, J. R. Seth, and M. Cloitre, “Influence of short-range forces on wall-slip in microgel pastes,” *Journal of Rheology*, vol. 52, no. 5, pp. 1241–1268, 2008.

[89] J. R. Seth, C. Locatelli-Champagne, F. Monti, R. T. Bonnecaze, and M. Cloitre, “How do soft particle glasses yield and flow near solid surfaces ?,” *Soft Matter*, vol. 8, no. 1, pp. 140–148, 2012.

[90] S. P. Meeker, R. T. Bonnecaze, and M. Cloitre, “Slip and flow in soft particle pastes,” *Physical Review Letters*, vol. 92, no. 19, pp. 1–4, 2004.

[91] C. Xu and N. Willenbacher, “How rheological properties affect fine-line screen printing of pastes: a combined rheological and high-speed video imaging study,” *Journal of Coatings Technology and Research*, pp. 1–12, 2018.

[92] D. Buzby and A. Dobie, “Fine line screen printing of thick film pastes on silicon solar cells,” in *Procedings of the 41st International Symposium on Microelectronics*, no. 610, pp. 645–649, 2008.

[93] J. Horzel, K. De Clercq, O. Evrard, J. Szlufcik, L. Frisson, F. Duerinckx, J. Nijs, and R. Mertens, “Advantages of a new metallisation structure for the front side of solar cells,” in *13th European Photovoltaic Solar Energy Conference and Exhibition*, 1995.

[94] K. Bothe, J. Schmidt, T. Weber, P. Altermatt, B. Fischer, and R. Brendel, “Electroluminescence imaging as an in-line characterization tool for solar cell production,” in *21st European Photovoltaic Solar Energy Conference*, pp. 597–600, 2006.

[95] C. Yüce and N. Willenbacher, “Challenges in rheological characterization of highly concentrated suspensions - A case study for screen-printing silver pastes,” *Journal of Visualized Experiments*, pp. 1–17, 2017.

[96] R. Brummer, *Rheology Essentials of Cosmetic and Food Emulsions.* Springer Berlin-Heidelberg, 2006.

[97] C. Macosko, *Rheology: Principles, measurements, and applications.* Wiley - VCH, 1994.

[98] N. Q. Dzuy and D. V. Boger, "Yield stress measurement for concentrated suspensions," *Journal of Rheology*, vol. 27, no. 1983, pp. 321 – 349, 1983.

[99] F. D. Cruz, F. Chevoir, D. Bonn, and P. Coussot, "Viscosity bifurcation in granular materials , foams , and emulsions," *Physical Review E*, vol. 66, no. 5, pp. 1–7, 2002.

[100] C. Yüce, M. König, and N. Willenbacher, "Rheology and screen-printing performance of model silver pastes for metallization of Si-solar cells," *Coatings*, vol. 8, no. 11, p. 406, 2018.

[101] T. Fellmeth, F. Clement, and D. Biro, "Analytical modeling of industrial-related silicon solar cells," *IEEE Journal of Photovoltaics*, vol. 4, no. 1, pp. 504–513, 2014.

[102] K. Holmberg, B. Kronberg, B. Jonsson, and B. Lindmann, *Surfactants and polymers in aqueous solutions.* John Wiley & Sons, 2003.

[103] H. Anthony and Q. D. Nguyen, "Rotating vane rheometry - a review," *Journal of Non-Newtonian Fluid Mechanics*, vol. 98, pp. 1–14, 2001.

[104] H. A. Barnes and J. O. Carnali, "The vane-in-cup as a novel rheometer geometry for shear thinning and thixotropic materials," *Journal of Rheology*, vol. 34, no. 6, pp. 841–866, 1990.

[105] S. Asakura and F. Oosawa, "Interaction between particles suspended in solutions of macromolecules," *Journal of Polymer Science*, vol. 33, pp. 183–192, 1958.

[106] J. Mewis and N. J. Wagner, *Colloidal suspension rheology.* Cambridge University Press, 2012.

[107] L. Martinie, H. Buggisch, and N. Willenbacher, "Apparent elongational yield stress of soft matter," *Journal of Rheology*, vol. 57, no. 2, pp. 627–646, 2013.

[108] W. Y. Shih, I. A. Aksay, and R. Kikuchi, "Reversible-growth model: Cluster-cluster aggregation with finite binding energies," *Physical Review A*, vol. 36, no. 10, pp. 5015–5020, 1987.

[109] K. Drabczyk and P. Panek, "Influence of screen printing parameters on the front metallic electrodes geometry of solar cells," *Circuit World*, vol. 40, no. 1, pp. 23–26, 2014.

[110] D. Erath, A. Filipović, M. Retzlaff, A. K. Goetz, F. Clement, D. Biro, and R. Preu, "Advanced screen printing technique for high definition front side metallization of crystalline silicon solar cells," *Solar Energy Materials and Solar Cells*, vol. 94, no. 1, pp. 57–61, 2010.

[111] C. Yüce, K. Okamoto, L. Karpowich, A. Adrian, and N. Willenbacher, "Solar Energy Materials and Solar Cells Non-volatile free silver paste formulation for front-side metallization of silicon solar cells," *Solar Energy Materials and Solar Cells*, vol. 200, pp. 1–12, 2019.

[112] A. Riverola, A. Mellor, D. Alonso Alvarez, L. Ferre Llin, I. Guarracino, and C. N. Markides, "Mid-infrared emissivity of crystalline silicon solar cells," *Solar Energy Materials and Solar Cells*, vol. 174, pp. 607–615, 2018.

[113] N. Zin, K. McIntosh, S. Bakhshi, A. Vázquez-Guardado, T. Kho, K. Fong, M. Stocks, E. Franklin, and A. Blakers, "Polyimide for silicon solar cells with double-sided textured pyramids," *Solar Energy Materials and Solar Cells*, vol. 183, pp. 200–204, 2018.

[114] F. Bashforth and J. C. Adams, "An attempt to test the theories of capillary action: by comparing the theoretical and measured forms of drops of fluid," *University Press*, 1883.

[115] B. Song and J. Springer, "Determination of interfacial tension from the profile of a pendant drop using computer-aided image processing," *Journal of Colloid and Interface Science*, vol. 184, pp. 64–76, 1996.

[116] E. Y. Arashiro and N. R. Demarquette, "Use of the pendant drop method to measure interfacial tension between molten polymers," *Materials Research*, vol. 2, no. 1, pp. 23–32, 1999.

[117] W. C. Hamilton, "A technique for the characterization of hydrophilic solid surfaces," *Journal of Colloid And Interface Science*, vol. 40, no. 2, pp. 219–222, 1972.

[118] W. Zhang and B. Hallström, "Membrane characterization using the contact angle technique I. methodology of the captive bubble technique," *Desalination*, vol. 79, no. 1, pp. 1–12, 1990.

[119] K. Grundke, T. Bogumil, C. Werner, A. Janke, K. Pöschel, and H.-J. Jacobasch, "Liquid-fluid contact angle measurements on hydrophilic cellulosic materials," *Colloids and Surfaces, A: Physicochemical and Engineering Aspects*, vol. 116, pp. 79–91, 1996.

[120] D. K. Owens and R. C. Wendt, "Estimation of surface free energy of polymers," *Journal of Applied Polymer Science*, vol. 13, pp. 1741 – 1747, 1969.

[121] E. Koos, "Capillary suspensions: Particle networks formed through the capillary force," *Current Opinion in Colloid and Interface Science*, vol. 19, no. 6, pp. 575–584, 2014.

[122] S. S. Velankar, "A non-equilibrium state diagram for liquid/fluid/particle mixtures," *Soft Matter*, vol. 11, no. 43, pp. 8393–8403, 2015.

[123] Elementitis Specialities, "Rheology Handbook," 2008.

[124] H. H. Berger, "Contact resistance and contact resistivity," *Journal of The Electrochemical Society: Solid -State Science and Technology*, vol. 119, no. 4, p. 507, 1972.

[125] D. K. Schroder and D. L. Meier, "Solar Cell Contact Resistance-A Review," *IEEE Transactions on Electron Devices*, vol. 31, no. 5, pp. 637–647, 1984.

[126] H. Sun, X. Zhang, and M. M. Yuen, "Enhanced conductivity induced by attractive capillary force in ternary conductive adhesive," *Composites Science and Technology*, vol. 137, pp. 109–117, 2016.